# Bonding of Glass-to-Glass for the Development of Ultrafast Microchip Lasers

by

Jansen Zhou

A thesis
presented to the University of Waterloo
in fulfillment of the
thesis requirement for the degree of
Master of Applied Science
in
Mechanical and Mechatronics Engineering

Waterloo, Ontario, Canada, 2023

©Jansen Zhou 2023

# Author's Declaration

This thesis consists of materials all of which I authored or co-authored: see Statement of Contributions included in this thesis. This is a true copy of the thesis, including any required final revisions, as accepted by my examiners.

I understand that my thesis may be made electronically available to the public.

# Statement of Contributions

Methods related to cleaning, bonding, and laser damage testing processes were taken directly from my published papers, references 41 and 50. Results for these processes, including chemical interface analysis, shear strength tests, and laser induced damage (LID) testing, were also taken from my published papers.

Jansen Zhou contributed to the literature review, conceptualization, methodology, software, investigation, analysis, and writing of all draft manuscripts.

Nanqin Mei and Prof. Zoya Leonenko contributed to the methodology and evaluation of the atomic force microscopy (AFM) readings.

Zhongqiang Liu, Reza Karimi, and Prof. Joe Sanderson all assisted in the methodology, collection, and evaluation of ultrafast LID material testing.

Prof. Michael Mayer assisted with development of surface roughness data visualization software.

Prof. Michael Mayer contributed to supervision, project administration, funding acquisition, conceptualization, writing, reviewing, and editing of all draft manuscripts. He also contributed to ideation of the project, developing the modified RCA-1 cleaning procedure with ammonium hydroxide rinse/wet mounting, as well as designing the first iteration of the custom made bonding apparatus. The design of this first bonding apparatus was done in collaboration with Montfort Laser.

Prof. Norman Zhou contributed to supervision, reviewing manuscripts, and project administration.

Permission was granted from Marketplace - Copyright Clearance Center (order numbers: 5531141361466, 1345557, 5531151500185, obtained on Apr. 17th, 2023) to use figs. 1.1, 1.4b, and 1.8.

Figs. 1.2 and 1.4a were reproduced under a Creative Commons Attribution 4.0 International License and a Creative Commons Attribution-NonCommercial 3.0 Unported Licence, respectively.

# Abstract

Direct glass-to-glass bonding is important for high-technology components in optics, microfluidics, and microelectromechanical systems applications. The focus of this research is on the design of an ultrafast, pulsed, microchip laser, specifically focusing on the microchip component. For this component, the proposed material is optically coated on both sides, allowing the light from a diode laser to be changed within it. This material is bonded to a saturable absorber, and sectioned into smaller units to accommodate size and mass production requirements.

I studied a number of different materials for this application, including 1 mm x 25 mm x 75 mm soda-lime float glass substrates and 8 mm diameter x 5 mm cylindrical fused silica/yittrium aluminum garnet (YAG) substrates, both optically coated and uncoated. The bonding process used is based on the classic RCA-1 cleaning procedure from the semiconductor industry modified with an ammonium hydroxide rinse, followed by a thermal treatment under unidirectional pressure without the need for a dedicated drying step. RCA-1 uses a solution of ammonium hydroxide and hydrogen peroxide to clean contaminants off the surface of silicon and enable subsequent bonding.

Bond quality was evaluated using two primary methods: destructive shear testing and laser induced damage (LID) testing through irradiation of the substrates by a continuous wave (CW) fiber laser and ultrafast, pulsed, femtosecond (FS) laser. Destructive shear testing of soda-lime glass samples revealed strong bonds (≈7.81 MPa on average) were achieved using a unidirectional pressure of approximately 0.88 MPa and low bonding temperatures between 160 °C and 300 °C applied for 30 min. Similar results were observed in uncoated fused silica samples.

The optical robustness of the bonds was tested in soda-lime glass and shown to be capable of surviving high powered CW fiber laser irradiation of at least 375 W focused for 2 s without delamination. Melting of the substrate was observed at higher powers and longer exposure times. Evolution of laser damage seemed to appear only in conjunction with melting of the bulk material, suggesting that optical robustness of the bonds is similar, if not greater than the bulk material.

When soda-lime glass samples were exposed to FS laser irradiation, the behaviour of a directly bonded sample was very similar to the bulk material. On the other hand, comparing a directly bonded sample to a poorly bonded sample showed very different damage evolution. Uncoated fused silica samples demonstrated this property as well, with greater damage appearing in poorly bonded samples versus directly bonded samples.

Surface roughness and chemistry was also characterized before and after cleaning, as these are influential factors affecting the efficacy of direct bonding. Surface roughness was measured using optical interferometry and atomic force microscopy (AFM). The results show that the surface roughness is comparable to measurements made with more complicated cleaning methods, demonstrating the advantage of our simplified method. The advantage of the ammonium bath as opposed to a rinse with deionized (DI) water is proposed in the surface chemistry analysis through X-ray photoelectron spectroscopy (XPS), which showed nitrogen incorporation at the bonding interface. This offers more opportunity for direct bonding. SEM was used to visually observe the

quality of the bonding interface. These images revealed a relatively high quality bonding interface. A cutting process was also developed to test the feasibility of mass production.

These results highlight the simplicity, optimization, and overall strength of the bonds created using the proposed bonding process, showing that it is an excellent option for the creation of ultra-fast, pulsed, microchip lasers. More information is also given regarding surface roughness ranges needed for direct bonding, as well as the mechanism of action for bonding using the RCA-1 chemical process. This will be useful in future optimization efforts for different materials.

# Acknowledgements

I would like to thank my parents for supporting me throughout my undergraduate degree as well as my master's. I am so fortunate to have had such a strong support network. I would also like to thank Prof. Michael Mayer and Prof. Norman Zhou for accepting me as a research student, even without a strong background in engineering. I appreciate their patience and support through experiment discussions, helping me to focus the breadth of my research into a single thesis.

I would like to thank Nanqin Mei, Prof. Zoya Leonenko, Zhongqiang Liu, Reza Karimi, Prof. Joe Sanderson, Matthew Scott, John Nugent, Yuquan Ding, Joseph Jessy, and Nina Heinig, for their assistance with data collection and training on various machines. With their support, I was able to learn a lot about scanning electron microscopy (SEM), atomic force microscopy (AFM), x-ray photoelectron spectroscopy (XPS), ultrafast lasers, and material dicing, while collecting publishable results.

I would like to also thank Brian Michael Tomkay, Kai Zhang, Joshua Jones, Kaiping Zhang, Shasvat Rathod, and all the other members of CAMJ for their help improving my presentation skills through the CAMJ seminar, technical support for research equipment, as well as simply making the long days at the lab a bit less tedious.

Finally, I would like to thank Daniel Kopf and Konstantina Kostourou of Montfort Laser, our industry sponsor. They provided invaluble feedback as well as funding throughout the project, helping to enable my research.

# Table of Contents

Author's Declaration ........ ii

Statement of Contributions ........ iii

Abstract ........ iv

Acknowledgements ........ vi

List of Figures ........ xi

Chapter 1: Introduction ........ 1

1.1 Literature Review: Low Temperature Glass-to-Glass Bonding ........ 3

1.2 Proposed Microchip Laser Design ........ 4

1.3 Factors Affecting Direct Bonding ........ 5

1.3.1 Chemical composition and mechanism of direct glass-to-glass bonding.. 5

1.3.2 Surface material topology ........ 6

1.4 Description of Laser Mechanics ........ 6

1.4.1 Continuous versus pulsed wave lasers ........ 6

1.4.2 FS laser interactions in fused silica and other transparent solids ........ 7

1.5 Factors Affecting Laser Damage at the Interface of Bonded Materials ........ 9

1.5.1 Average power density ........ 9

1.5.2 Other factors ........ 9

1.6 Scope and Objectives ........ 11

1.7 Chapter 1 Summary ........ 11

Chapter 2: Sample Preparation ........ 12

2.1 Cleaning Procedure ........ 12

2.1.1 Concentration determination for the cleaning solution ........ 12

2.1.2 General cleaning procedure ..... 12

2.2 Bonding Procedure ..... 13

2.2.1 General bonding procedure ..... 13

2.2.2 Parameters used for soda-lime glass ..... 15

2.2.3 Parameters used for fused silica pucks ..... 15

2.2.4 Iterations of the bonding apparatus ..... 16

2.3 Surface Roughness Characterization ..... 17

2.3.1 Optical profiler interferometry ..... 17

2.3.2 Atomic force microscopy (AFM) ..... 17

2.4 Bonding Interface Visual and Chemical Analysis ..... 18

2.4.1 X-ray Photoelectron Spectroscopy (XPS) Analysis ..... 18

2.4.2 Scanning Electron Microscopy (SEM) and Energy Dispersive X-ray (EDX) Analysis ..... 19

2.5 Tensile Shear Testing ..... 19

2.5.1 Soda-lime glass shear testing ..... 19

2.5.2 Fused silica shear testing ..... 21

2.6 Laser Induced Damage (LID) Testing ..... 23

2.6.1 Continuous wave (CW) laser damage setup ..... 23

2.6.2 Femtosecond (FS) laser damage setup ..... 24

2.7 Chapter 2 Summary ..... 25

Chapter 3: Properties of the Bonded Interface ..... 26

3.1 Surface Roughness Testing ..... 26

3.1.1 Interferometry-based optical profiler results ..... 26

3.1.2 Soda-lime glass AFM surface roughness results ... 28
3.2 Analysis of Bonding Interface ... 29
3.2.1 X-ray photoelectron spectroscopy (XPS) analysis ... 29
3.2.2 Scanning electron microscopy (SEM) and energy dispersive x-ray (EDX) analysis ... 31
3.3 Qualitative Shear Testing ... 33
3.3.1 Soda-lime glass ... 33
3.3.2 Fused silica ... 34
3.4 Quantitative Shear Testing ... 35
3.4.1 Soda-lime glass ... 35
3.4.2 Fused silica ... 37
3.5 Chapter 3 Summary ... 38
Chapter 4: Design Considerations for the Microchip Laser ... 40
4.1 Laser Damage Results ... 40
4.1.1 Continuous wave (CW) laser damage results ... 40
4.1.2 Soda-lime femtosecond (FS) laser damage results ... 41
4.1.3 Fused silica FS laser damage results ... 42
4.2 Developing a Dicing Workflow ... 44
4.2.1 Preparing samples for dicing ... 44
4.2.2 Dicing the samples ... 45
4.3 Chapter 4 Summary ... 46
Chapter 5: Conclusions and Future Directions ... 47
References ... 48

Appendix A: Design schematics for bonding apparatus ... 53

Appendix B: Code used for data processing ... 57

# List of Figures

Figure 1.1: Cold-welded bronze dagger with intricate designs made of gold and silver pressed into it (reproduced with permission) [1]. ........ 1

Figure 1.2: Example of glass microfluidic device that is formed using direct glass-to-glass bonding [15]. ........ 2

Figure 1.3: Examples of Newton rings. [A] Diagram of Newton rings and central black dot observed by Newton. The central black dot is labelled with an X [17]. [B] Sample of bonded soda-lime glass, with an example of the central black dot and Newton rings labelled. ........ 3

Figure 1.4: Shear graphs showing the advantage of new methods over traditional ones. [A] Shear graph showing that VUV irradiated bonding silicon samples had a much higher shear strength than traditional silicon directly bonded samples. The peak bonded shear strength for the VUV irradiated samples was at around 8 MPa [10]. [B] Shear graph showing that Ar ion beam SAB is much more effective than standard SAB methods. The peak bond energy for the Ar ion beam exposed samples was around 2 J/m2 [19]. Fig. 1.4b is reproduced with permission. ........ 4

Figure 1.5: Multiple possible designs for the microchip component within the laser. [A] Original patent designs proposed by Montfort Laser, showing many possible variations. [B] An updated microchip design based on a more recent publication from Montfort Laser. Important components are labelled. HR = highly reflective coating, AR = anti-reflective coating, PR = partially reflective coating. Fig. 1.5a is reproduced with permission. ........ 5

Figure 1.6: Example of possible surface topology at the interface of two glass substrates. Note the roughness of the surface on both samples. These are asperities. ........ 6

Figure 1.7: Graph showing laser power versus time relative to type of laser. CW lasers have continuous output, but generally have the lowest peak power. PW lasers have higher peak powers and are pulsed. Ultrafast lasers have very short pulses and the highest peak powers [31]. ........ 7

Figure 1.8: Occupancy of electron conduction bands within irradiated silicon material as laser fluence of 30 fs pulses with wavelength 800 nm is increased [32]. [A] Occupancy of electron conduction bands within irradiated silicon material at 0.9 J/cm2 laser fluence. Occupancy is relatively low. [B] Occupancy of electron conduction bands within irradiated silicon material at 2.7 J/cm2 laser fluence. Occupancy is much higher. Both graphs reproduced with permission. ........ 8

Figure 1.9: Diagram showing beam shape of focused gaussian laser used in this research. Note the hourglass shape that forms the focused laser spot. ........ 10

Figure 2.1: Fume hood workspace for creating the cleaning solution and applying it to the glass substrates. [A] Fume hood workspace, with all tools used in the experiments labelled. [B] Picture showing the cleaning solution after all chemicals have been combined at the correct temperature. ........ 13

Figure 2.2: [A] Schematic diagram of clamping apparatus used for bonding process. Glass sample dimensions: Brand - Thermo Scientific, 1 mm × 76 mm × 26 mm, Brand - VWR, 1 mm × 75 mm × 25 mm [42,43]. Red represents the cleaned glass substrates, whereas yellow represents the uncleaned glass substrates. [B] Image of custom bonding apparatus clamping soda-lime glass samples. Note that the configuration of the glass substrates is different in the diagram versus the image. 14

Figure 2.3: Thermal treatment setup used to bond glass to glass. [A] Inside of precision oven, showing temperature sensor that measures temperature of the oven. [B] Full thermal treatment setup, showing temperature detector connected to temperature sensor, as well as computer used to run temperature measurement code. 14

Figure 2.4: Various configurations used to bond the glass substrates. This was done to accommodate the bond strength testing method that each sample would undergo. [A] Initial configuration used during qualitative testing. Bonding was limited to a 3 cm × 3 cm area. [B] Complete overlap configuration. Offers the most opportunity for bonding since it has the greatest overlapping area. [C] Partial overlap configuration. Was originally designed for quantitative shear testing applications, but glass was too brittle to be gripped effectively. Ultimately the least used configuration... 15

Figure 2.5: [A] Top view of coated fused silica sample. Coating causes surface to appear green. [B] Side view of coated fused silica sample. [C] Top view of uncoated fused silica sample. [D] Side view of uncoated fused silica sample. An example of a single puck and full bonded sample is shown in this image. 16

Figure 2.6: Oxidation present on the first design of the bonding apparatus. [A] Top view of the bonding apparatus. Stainless steel plunger used shows resistance to repeated heat treatments relative to scrap steel. [B] Side view of bonding apparatus. 16

Figure 2.7: Pictures of newer bonding apparatus. [A] Top view of apparatus. [B] Side view of apparatus. Note that there are five plungers to apply pressure to five different samples. 17

Figure 2.8: Optical profiler and AFM used to gather surface roughness data for the glass substrates. [A] Optical profiler used to gather surface roughness data. [B] AFM used to gather surface roughness data. Two methods were used to ensure accuracy of the results. AFM picture provided courtesy of Nanqin Mei. 18

Figure 2.9: Diagram of tensile testing setup for soda-lime glass. Bonded samples were glued to aluminium plates with super glue to increase rigidity of the samples for testing. Samples were compressed at 1 mm/min until failure at the bond site or bulk material. Samples that broke before force was applied or broke at the glue bond were not considered in the results. This method is based on the testing method reported in reference 23. [A] Labelled diagram of tensile testing setup. [B] Actual tensile testing setup. 20

Figure 2.10: Examples of interfacial and bulk material damage after shear testing. [A] Shear damage at the center of the sample. If damage appeared only in this center area after shear testing, fail-

ure at the interface occurred. [B] Shear damage in the bulk material. If the center remained intact and damage occurred elsewhere, failure in the bulk material occurred...................................... 21

Figure 2.11: Shear testing setup designed for fused silica samples, both coated and uncoated. [A] Labelled diagram of shear testing setup. Samples are tested in compression mode, and compressed at a rate of 0.5 mm/min. [B] Picture of actual shear testing setup before compression is started........................................................................................................................ 22

Figure 2.12: Examples of fractured coated and uncoated fused silica bonded samples after shear testing. [A] Image of uncoated fused silica pucks shows damage after shear testing on both sides of the interface. [B] Image of coated fused silica pucks shows damage after shear testing on both sides of the interface. ....................................................................................................... 22

Figure 2.13: CW laser testing setup for both soda-lime glass and fused silica samples. Laser is encased by an atmosphere-controlled glove box. Notable features of the box and the laser itself are highlighted. ........................................................................................................... 23

Figure 2.14: FS laser testing setup for both soda-lime glass and fused silica samples. Laser is directed into the work area via several mirrors and focused using a 20 cm or 5 cm focal length lens. Important parts of the setup, such as control systems for 3-axis movement and power control using beam splitting and polarization are labelled..................................................................... 25

Figure 3.1: Example of optical profiler surface roughness results for soda-lime glass before cleaning. [A] The micrograph on the left shows a 2D representation of the surface roughness. [B] The graph on the right shows the detrended surface roughness over a single ridge for about 100 µm. This ridge distance is highlighted by the red line in the micrograph......................................... 26

Figure 3.2: Example of optical profiler surface roughness results for uncoated fused silica before cleaning. [A] The micrograph on the left shows a 2D representation of the surface roughness. [B] The graph on the right shows the detrended surface roughness over a single ridge for about 100 µm. This ridge distance is highlighted by the red line in the micrograph. Surface roughness artifacts are also labelled....................................................................................................... 27

Figure 3.3: Example of optical profiler surface roughness results for coated YAG after cleaning. [A] The micrograph on the left shows a 2D representation of the surface roughness. [B] The graph on the right shows the surface profile across one of the imperfections along the surface. The surface profile reveals a deep hole in the surface of the sample. This profile is highlighted by the red line within the micrograph.................................................................................. 28

Figure 3.4: [A] AFM topography image of the sample before applying the cleaning process. The image is 700 nm × 700 nm in scale. [B] Cross-sectional profile of the selected white line in the image in part A. [C] 3D view of the sample surface. ................................................................. 29

Figure 3.5: [A] AFM topography image of the sample after the cleaning process. The image is 700 nm × 700 nm in scale. [B] Cross-sectional profile of the selected white line in the image in part A. [C] 3D view of the sample surface. ....................................................................... 29

Figure 3.6: Model of microscopic bonding mechanism at the glass-to-glass interface, based on high resolution XPS results and model outlined by reference 9. The mechanism shows the structure of temporary hydrogen bonding formed before thermal treatment (right), as well as permanent covalent bonding (Si-O-Si and Si-N-N-Si bonds) that occurs after thermal treatment (left) [9,27]. Ammonia is presented as a hydrogen bond mediator in this image because an ammonium hydroxide rinse was used in our experiments. In the traditional RCA-1 cleaning rinse, interfacial hydrogen bonding is mediated by water. Illustration was created using Chemspace (https://chemspace.com/real-space). ........ 30

Figure 3.7: XPS results comparing soda-lime glass sample interfaces before and after the cleaning procedure. [A] Broad XPS scan of soda-lime glass surface before cleaning. Location of nitrogen binding energies is circled. [B] Broad XPS scan of soda-lime glass surface after cleaning. Location of nitrogen binding energies is circled. [C] High resolution XPS scan focused on nitrogen binding energies before cleaning. No clear nitrogen peak present. [D] High resolution XPS scan focused on nitrogen binding energies after cleaning. Clear nitrogen peak present. High resolution spectroscopy calibrated using C 1s to 284.8 eV reveals a clear nitrogen peak in the cleaned sample, and the absence of a peak before cleaning. Nitrogen peak is centered around 399.81 eV in the cleaned sample. ........ 31

Figure 3.8: [A] SEM image of bonding interface for soda-lime glass sample. [B] SEM image of bonding interface for uncoated fused silica sample. [C] SEM image of bonding interface for coated fused silica sample. [D] EDX results for bonding interface of soda-lime glass sample. [E] EDX results for bonding interface of uncoated fused silica sample. [F] EDX results for bonding interface of coated fused silica sample. ........ 32

Figure 3.9: SEM and EDX results for coated YAG sample. [A] SEM image of top of sample, showing coating. [B] SEM image of cross-section of sample. Position of sample shown in top right. [C] EDX analysis of sample coating elemental composition. Area measured is shown with a pink rectangle. [D] EDX analysis of cross-sectional elemental composition. Area measured is shown with a pink rectangle. ........ 33

Figure 3.10: Images of 3 different soda-lime glass samples, showing bonded and unbonded areas of glass. Metric scales are given. Newton rings are apparent, as they separate the bonded areas from the unbonded areas. ........ 34

Figure 3.11: Several images showing bonded fused silica samples, highlighting some contamination that occurs at the interface. [A] Side view of uncoated fused silica bonded sample. [B] Top view of uncoated fused silica bonded sample. [C] Top view of contaminated, coated, fused silica sample. Highlighted discolouration indicates contamination. [D] Microscope image of contamination at the interface of a bonded, uncoated fused silica sample. ........ 35

Figure 3.12: Graph showing load experienced by a bonded soda-lime glass sample relative to the distance compressed. There is deviation from a linear relationship between load and compression distance. ........ 36

Figure 3.13: Shear strength of bonded soda-lime glass samples tested mechanically using a tensile tester (Instron 5548). This is compared to the temperature at which each sample was treated in a furnace (Binder oven) for 30 min. All samples were clamped with an approximate pressure of 0.88 MPa. Samples were in the furnace for 30 min, excluding a 7 min ramp/time before stabilization. The complete overlap bonding configuration was used for all tested samples. There seemed to be one outlier with a measured shear strength (19.9 MPa) much higher than the average. Temperature values of 280 °C and higher were measured using the Binder oven's internal temperature probe. Temperature values below 280 °C were measured using an external resistive temperature detector.
........................................ 37

Figure 3.14: Graphs showing load experienced by bonded fused silica samples relative to the distance compressed. [A] Shear graph for uncoated fused silica sample. There is a small period of no load due to initial clamping position. [B] Shear graph for coated fused silica sample. Both sample loads increased relatively linearly and reached similar peak loads. ........................................ 38

Figure 4.1: Directly bonded soda-lime glass sample annealed at 160 °C. Bond delamination is observed at the location where the laser irradiated the sample, indicated by the bending of Newton rings around the damage site. A magnification of the sample shows melting after exposure to a 375 W CW laser for 4 s. ........................................ 41

Figure 4.2: Images of samples used in soda-lime FS laser induced damage threshold (LIDT) experiment. [A] Irradiated sample of soda-lime glass bonded using modified RCA-1 procedure. [B] Irradiated bulk material sample of soda-lime glass. [C] Irradiated sample of two taped soda-lime glass substrates to simulate a poor bond. ........................................ 41

Figure 4.3: LIDT analysis results for three conditions of soda-lime glass samples to test optical robustness of bonds. The poor bonding condition has the highest rate of laser damage increase as well as the highest peak for laser damage. The bonding condition and the bulk material condition both had similar reactions to the laser. ........................................ 42

Figure 4.4: Results for FS induced laser damage in uncoated fused silica samples. [A] Micrograph of cross-section of poor bonding condition fused silica sample, processed to highlight damage caused by the FS laser within the sample. [B] Damage width versus position along damage line measured along red lines in poor bonding condition micrograph, with position pixel measurements converted to metric units using a known approximate scale. Average damage width for each power is shown by the thicker horizontal plotted lines. [C] Diagram of sample irradiation geometry. Laser focus begins to the left of the bonding interface, and is moved to the right. [D] Micrograph of cross-section of bonding condition fused silica sample, processed to highlight damage caused by the FS laser within the sample. [E] Damage width versus position along damage line measured along red lines in bonding condition micrograph, with position pixel measurements converted to metric units using a known approximate scale. Average damage width for each power is shown by the thicker horizontal plotted lines. [F] Original image of poor bonding condition sample used for analysis, before image processing. The samples were irradiated from the right, then cross-sectioned and polished for viewing. [G] Original image of bonding condition

sample used for analysis, before image processing. The samples were irradiated from the right, then cross-sectioned and polished for viewing. ............................................................ 43

Figure 4.5: Images of bonded, uncoated, fused silica samples before dicing workflow. [A] Side view of sample, including dimensions. [B] Top view of sample, including dimensions. ............ 44

Figure 4.6: Pictures of devices used for thinning fused silica samples. [A] Low speed saw used for coarse sectioning of samples. [B] Polishing device used for cleaning up the surfaces after cutting. ........................................................................................................................ 45

Figure 4.7: Pictures of thinned fused silica samples after cutting and polishing......................... 45

Figure 4.8: Processing of thinned fused silica samples into 2 mm3 samples. [A] Thinned fused silica sample after dicing, bonded using dicing adhesive to rigid carrier. [B] Thinned fused silica sample after dicing. [C] Side view of single diced fused silica 2 mm3 cube. Bonding interface is not visible, and cut edges are sharp. ........................................................................... 46

Figure A-1: CAD design for bottom piece of bonding apparatus with single plunger. Sizes are in mm. Design created by Montfort Laser and Prof. Michael Mayer. ............................................ 53

Figure A-2: CAD design for top piece of bonding apparatus with single plunger. Sizes are in mm. Design created by Montfort Laser and Prof. Michael Mayer. ........................................................................................................................ 54

Figure A-3: Updated CAD design for bottom piece of bonding apparatus with 5 plungers. Sizes are in mm. ........................................................................................................................ 55

Figure A-4: Updated CAD design for top piece of bonding apparatus with 5 plungers. Sizes are in mm. ........................................................................................................................ 56

Figure B-1: Code used to load surface roughness data collected using interferometry into Matlab for data processing. Code was originally written by Prof. Michael Mayer. filename: DataLoading.m ........................................................................................................................ 57

Figure B-2: Code used to visualize surface roughness data collected using interferometry. Data is graphed initially as a contour plot of the surface of the substrate, with other graphs included such as a detrended surface profile along a specified line to determine RMS surface roughness and a graph for the determination of the waviness of the profile. Code was originally written by Prof. Michael Mayer. filename: DataVisualisation.m.......................................................................... 59

Figure B-3: Code used to control multimeter that measures temperature of the oven during bonding thermal treatment. Temperature is measured using 4-wire resistance readings received from a temperature sensor connected to the multimeter. Code was modified, using existing code from a previous master's student who used the system [58]. filename: Laser Temp measure.py ............ 65

Figure B-4: Code used to process uncoated fused silica LID results. Image processing was used to generate a mask of the brightest pixels in the image, which were the damaged areas within the material. The damage width was then measured along a line to characterize damage severity. file-name: laserdmgmask.m ........................................................................................................ 69

# Chapter 1: Introduction

Bonding is a general term to refer to materials which are connected in some way to form a new, single, entity. This is a very old technique, dating back as far as the mesolithic and neolithic ages, where rope was used to bind objects together [1]. Cold welding is another technique that was used prominently by ancient civilizations. By pressing a malleable metal into another metal using great force without the application of heat, intricate designs were created on objects such as daggers and plates. An example of this is shown in fig. 1.1 [1,2].

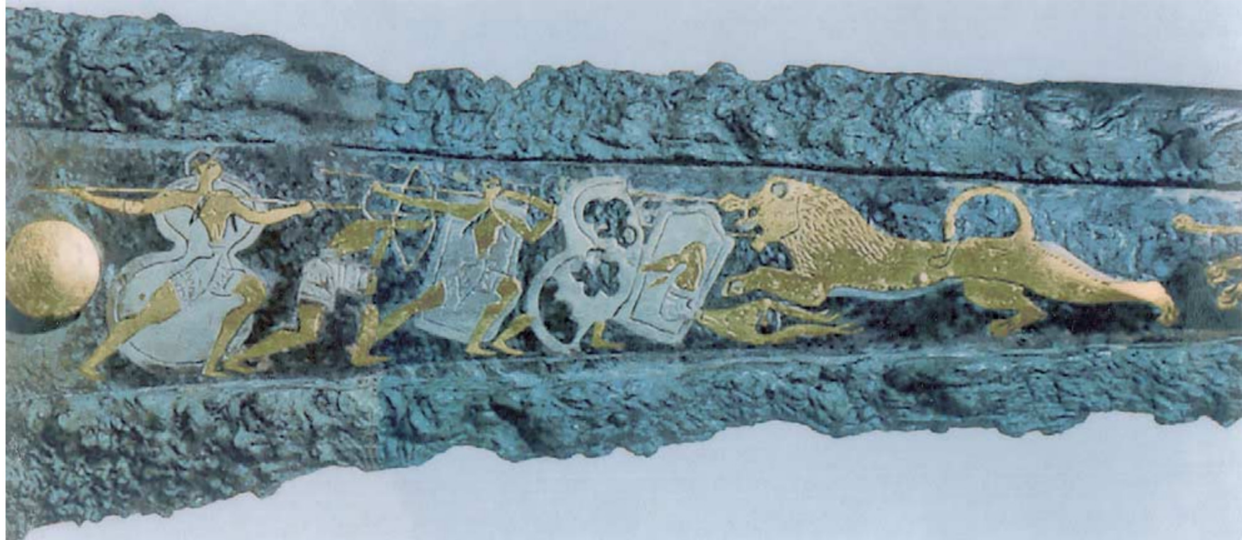

Figure 1.1: Cold-welded bronze dagger with intricate designs made of gold and silver pressed into it (reproduced with permission) [1].

Cold welding is a type of direct bonding [2]. Direct bonding is a process used to join substrates across an interface without the need for an interlayer or filler material [3-6]. As shown in fig. 1.1, this can be done with metals, such as gold and silver, but modern applications typically focus on glass and other silicon-based materials. Glass joints made with direct bonding are important in a number of applications, including chemical analysis [3-7], microfluidics [8-11], and in the development of ultrafast, pulsed, microchip lasers, the last of which is the motivation for this study [10-13].

Devices used in microfluidics contain microchannels for applications such as single molecule sorting and analysis. They need to be made of glass for visual observation and chemical stability, as well as be mechanically robust for stability of the channels. These channels are sealed with glass-to-glass bonding [14]. An example of these devices is shown in fig. 1.2. For laser applications, the glass bonds need to be strong enough to withstand high powered laser pulses without breaking or fracturing.

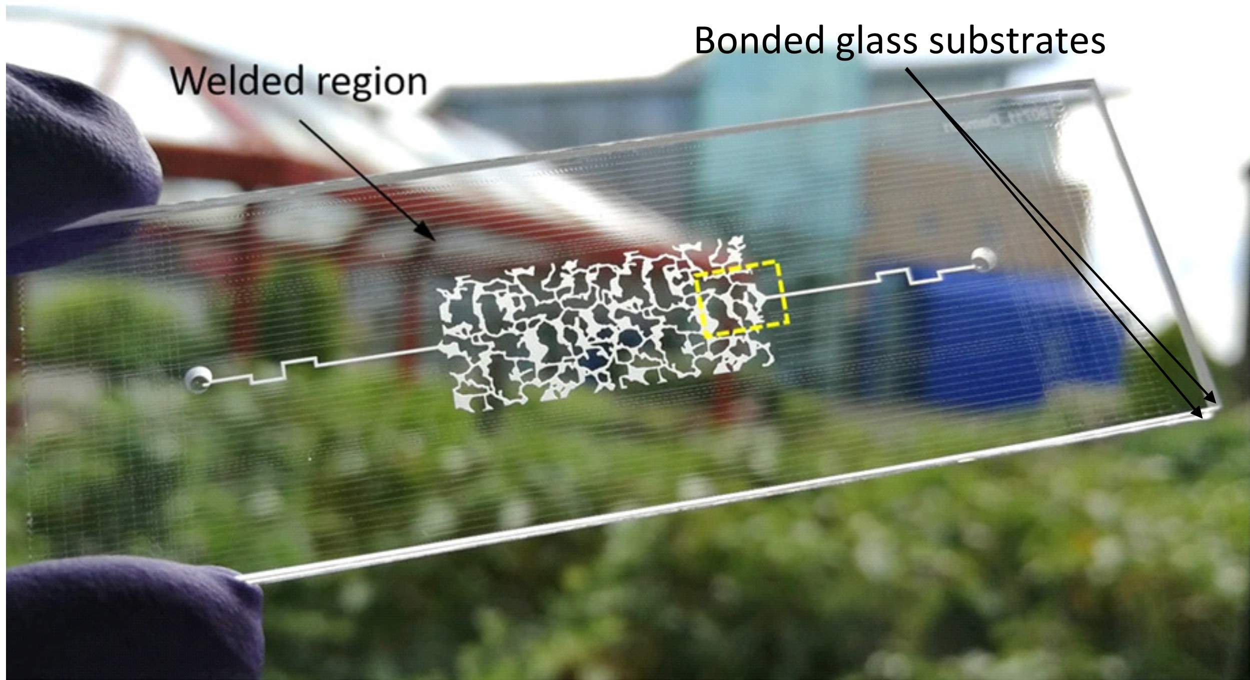


Figure 1.2: Example of glass microfluidic device that is formed using direct glass-to-glass bonding [15].

There are several important characteristics of glass bonds. For distances under 20 nm, an equation for the collective attractive van der Waals force between two materials can be calculated using the equation

$$F = \frac{A_{132}}{6\pi d^3} \tag{1}$$

where $F$ is the attractive force between materials *1* and *3* in medium *2*, $d$ is the distance between the materials, and $A$ is the Hamaker's constant specific to the materials and medium used. This equation may help to predict the shear strength of our bonds [1].

Additionally, there was the famous discovery of Newton rings. Sir Isaac Newton studied the properties of prisms. He pressed two prisms, one curved and one flat, against each other and noted two interesting observations:

1. The presence of a central black spot at the point at which the curved and flat prisms met.
2. Surrounding this black spot, he saw multicoloured rings (these were Newton rings).

While he may not have known it at the time, he had discovered an optical phenonemon that occurs when two transparent solids come into intimate contact with each other. When two transparent bodies are close together, the point of contact naturally suppresses light reflection, resulting in the black spot described in the first observation [1]. Although, depending on phase, the center may also appear bright [16]. Surrounding this central area, there are alternating bright and dark bands

which are a result of constructive and destructive interfering light waves within a layer of air that exists between the curved and flat surfaces as you move outwards from the point of contact [16]. This phenomenon is useful in glass-to-glass bonding research to visually determine locations of unbonded areas caused by contamination. An example of Newton rings is shown in fig. 1.3.

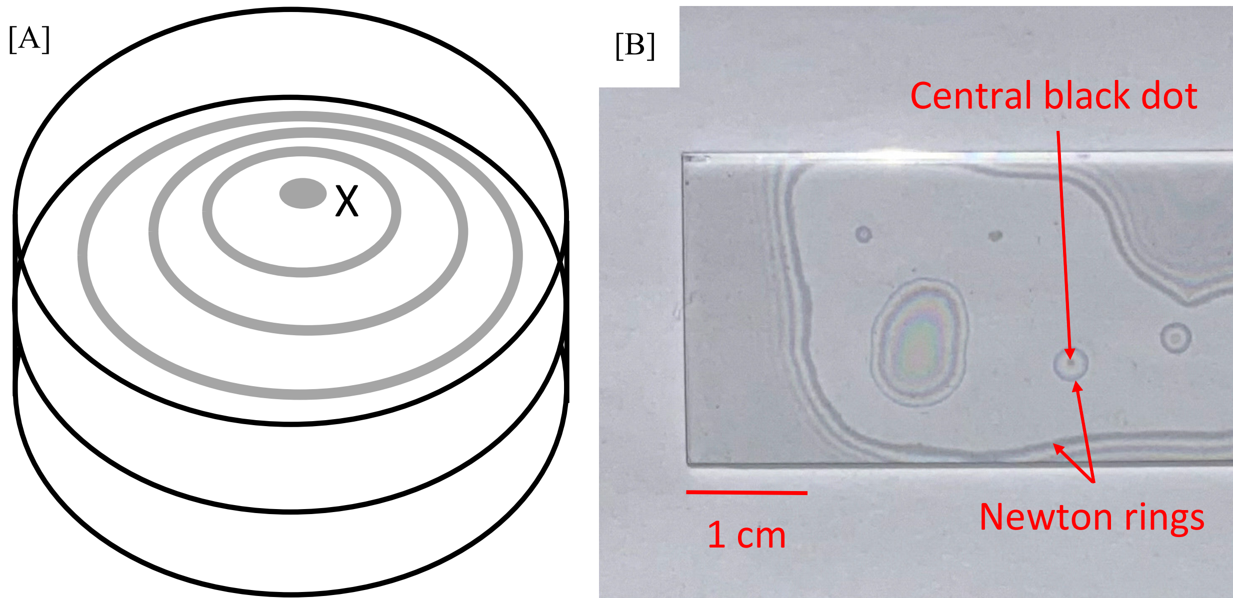


Figure 1.3: Examples of Newton rings. [A] Diagram of Newton rings and central black dot observed by Newton. The central black dot is labelled with an X [17]. [B] Sample of bonded soda-lime glass, with an example of the central black dot and Newton rings labelled.

Due to the brittle nature of glass, cold welding is not very effective in making direct glass bonds. To make permanently strong glass bonds, high process temperatures, pressures, and bonding times are usually used [3,4,18]. This type of direct bonding is called silicon fusion bonding, where the surfaces are cleaned and heated to their softening point, forming a welding interface [4]. Pyrex glass fusion bonding needs a process temperature of ≈650 °C [4]. High purity fused silica fusion bonding can reach as high as 1000 °C [4,9]. However, for the construction of high-technology components in the optical, microelectronic, and microfluidic fields, lower process temperatures are beneficial [3,4,9,19-22]. Elevated temperatures can limit the use of sensitive functional elements in the bonding stack, as well as cause thermomechanical stress when using materials with different thermal expansion coefficients [3,4,9,20,22].

## 1.1 Literature Review: Low Temperature Glass-to-Glass Bonding

Specialized cleaning procedures are required to prepare glass surfaces for low temperature direct bonding [9,10,20]. Reference 23 reports a study on the effects of various cleaning reagents for direct bonding of glass-to-glass. While the authors achieved strong bonding (≈6 MPa) without the use of adhesives, their procedure still required relatively high temperatures (400 °C) and relatively long bonding times (10 h) [23]. Reference 24 reports an optimized solution for cleaning soda-lime glasses, however they also use high temperatures (560 °C) and bond times (4 h).

More recently, surface-activated bonding (SAB) approaches have been shown to be a promising technique to lower process temperatures [9,10,19,20]. These include techniques such as plasma cleaning and ultraviolet irradiation to activate and clean the bonding interface of substrates before contact. Reference 10 used vacuum ultraviolet irradiation (VUV) for this purpose. After heat treatment at relatively low temperatures (150 °C to 300 °C) for 8 h, the samples were shear tested. A peak bonding strength of around 8 MPa was achieved (fig. 1.4a), which is reportedly much higher than traditional silicon bonding. Reference 20 reports a similar method, using VUV radiation to activate dissimilar materials for bonding, followed by prebonding and annealing at low temperatures (<200 °C). This resulted in robust dissimilar bonding strengths, with a peak bonding strength of around 10 MPa achieved. Reference 19 used yet another method, bonding samples of silicon carbide (SiC) using an Ar beam to activate the wafer surface at room temperature under pressure. This technique was shown to generate higher bonding energies than standard SAB (fig. 1.4b).

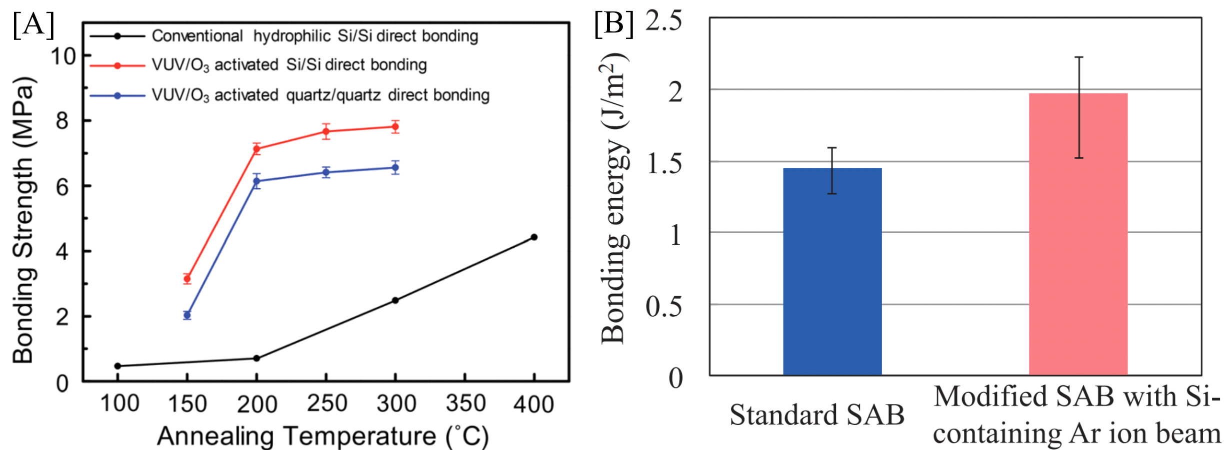


Figure 1.4: Shear graphs showing the advantage of new methods over traditional ones. [A] Shear graph showing that VUV irradiated bonding silicon samples had a much higher shear strength than traditional silicon directly bonded samples. The peak bonded shear strength for the VUV irradiated samples was at around 8 MPa [10]. [B] Shear graph showing that Ar ion beam SAB is much more effective than standard SAB methods. The peak bond energy for the Ar ion beam exposed samples was around 2 $J/m^2$ [19]. Fig. 1.4b is reproduced with permission.

As is evidenced by the examples given, while these techniques have achieved strong bonding at low temperatures (24 °C to 300 °C), they are often complex, multistep processes that still require extensive bonding times (2 h to 24 h) in order to function [9,10,20,25]. There is a gap in knowledge regarding fast, direct bonding processes for silicon materials at low temperatures. Such knowledge would be helpful to accommodate industry mass production of reliable bonds. More information also needs to be known about how laser induced damage affects the bonding interface for microchip laser applications.

## 1.2 Proposed Microchip Laser Design

For the present study, there are several proposed designs for the microchip within the laser, a few of which are included in fig. 1.5a. One of these designs (1.5b) will be described here in more detail to exemplify the need for a directly bonded component within the laser. This design is derived from reference 26.

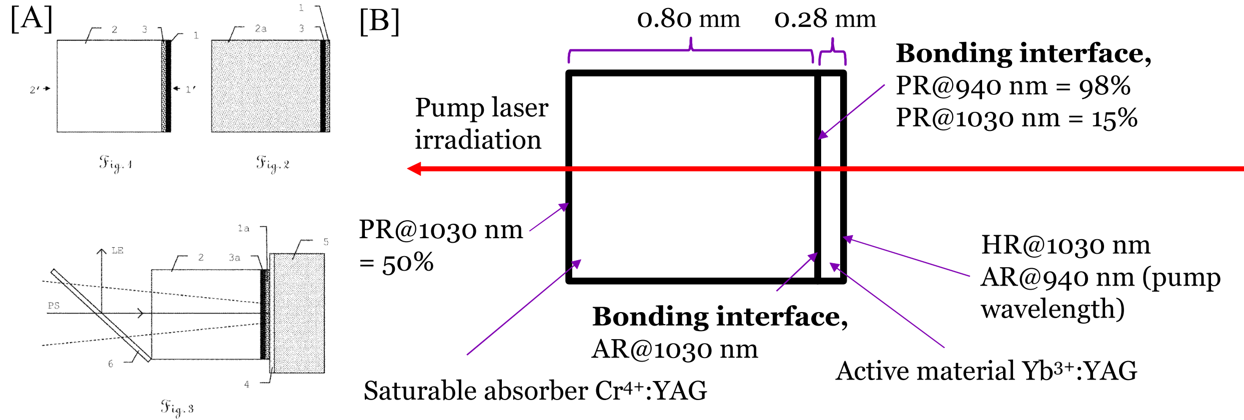


Figure 1.5: Multiple possible designs for the microchip component within the laser. [A] Original patent designs proposed by Montfort Laser, showing many possible variations. [B] An updated microchip design based on a more recent publication from Montfort Laser. Important components are labelled. HR = highly reflective coating, AR = anti-reflective coating, PR = partially reflective coating. Fig. 1.5a is reproduced with permission.

In fig. 1.5b, a thin active material ground to a thickness of 0.28 mm is bonded directly to a 0.8 mm saturable absorber. Both of these components have optical coatings on their surfaces, which allow the pumped laser light to change within the material before being ejected out the other side. Specifically, the distribution of HR, AR, and PR coatings result in power, wavelength, and pulse length changes [26]. Both of these substrates should be made of the same material, in order to avoid cracking due to differences in coefficients of thermal expansion. Direct bonding is required for several reasons, including structural support for the thin active material, to conserve space within the microchip laser, and maintain stable cavity length [26].

## 1.3 Factors Affecting Direct Bonding

There are two major factors that affect low temperature direct bonding. These are the chemical composition at the interface and topology of the material interface.

### 1.3.1 Chemical composition and mechanism of direct glass-to-glass bonding

There are many possible bonding mechanisms for glass substrates, depending on the procedure used to prepare them. An example mechanism will be discussed here. There exists on the surface of glass a vast number of silanol groups [23,27]. These groups form when silicon is exposed to ambient water in the air, resulting in increased hydrophilicity of the glass surface [27]. This property encourages the surface groups of glass substrates to form hydrogen bonds. Such bonds can bridge across the interface of two glass surfaces when they are brought close together, creating

temporary links that can be converted to stronger, permanent covalent bonds through a condensation reaction activated by thermal treatment [23,27].

### 1.3.2 Surface material topology

The bonding mechanisms for glass substrates require enough surface area contact at a nanometer distance [9,27,28]. This contact area is determined by the asperities at the glass surface and particle contamination. Dust, debris, and organic contaminants can prevent the mechanism from occuring by blocking contact between the silanol groups or causing excessive physical separation between glass substrates [23]. Separation that is too large can prevent permanent, covalent bonds from forming since these bonds only act over relatively small distances [29]. Thus, such separations result in either no bonding between the substrates, or weak hydrogen bonding [29].

Asperities are a feature of the material surface itself and typically need to be within a certain range to allow for two surfaces to bond [28,30]. An example of the asperities that could be found at a glass-to-glass interface is shown in fig. 1.6. Pressure can help to overcome the effects of particle contamination and rough surfaces, as substrates can deform elastically to allow for more effective contact [27]. At higher temperatures, materials are more malleable and compliant, also contributing to an increased effective contact area [27].

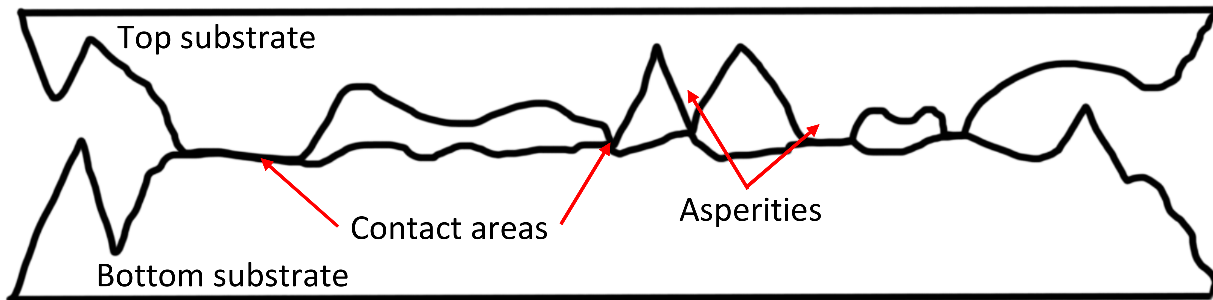


Figure 1.6: Example of possible surface topology at the interface of two glass substrates. Note the roughness of the surface on both samples. These are asperities.

## 1.4 Description of Laser Mechanics

Another important factor to consider for the goal of this research is the optical robustness of the bonds for the design of ultrafast, pulsed, microchip lasers. For this, some background on laser mechanics and laser interactions with glass materials is discussed.

### 1.4.1 Continuous versus pulsed wave lasers

For many years, lasers have been studied in many potential applications, including precision laser cutting for material processing, DNA sequencing, and electronics manufacturing [31]. For those unfamiliar with lasers, visible lasers, such as laser pointers, are the first thing that typically comes to mind. These are a type of continuous wave (CW) laser, since their light output is a continuous,

uninterrupted beam. However, even the most powerful CW lasers have lower peak power than many pulsed wave lasers. Pulsed wave (PW) lasers, as the name suggests, are not continuous. Rather, there are periods of on/off, which helps to condense the energy and achieve higher peak powers. Taken to the extreme, lasers can have pulse durations in the range of 5 fs to 100 ps. These lasers are considered ultrafast, and have the highest peak powers [31]. A visual comparison of these laser types is shown in fig. 1.7.

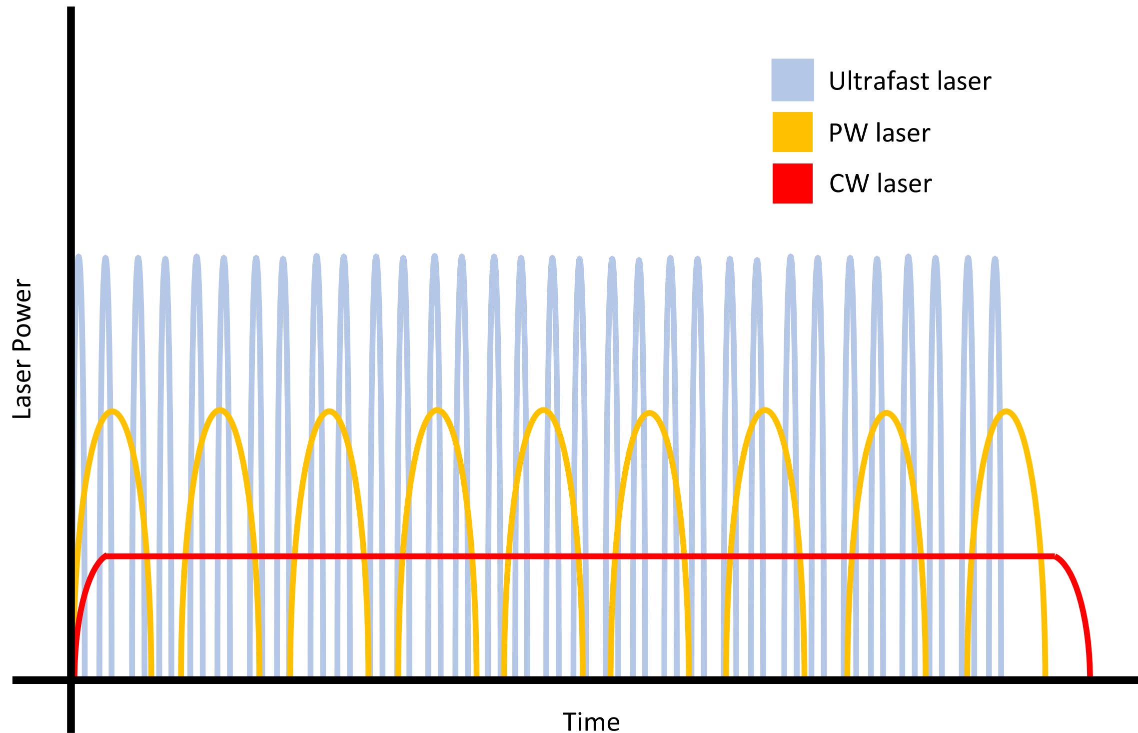


Figure 1.7: Graph showing laser power versus time relative to type of laser. CW lasers have continuous output, but generally have the lowest peak power. PW lasers have higher peak powers and are pulsed. Ultrafast lasers have very short pulses and the highest peak powers [31].

Ultrafast lasers are very interesting for material applications, due to their unique ablative effects. In CW and long PW lasers, material damage is generally caused by thermal effects which are carried through the material beyond the initial irradiated area. On the other hand, ultrafast lasers have such high peak powers that irradiation of the material results in ablations without significant heating [31]. This results in very precise machining capabilities, as only the irradiated area is removed [32].

### 1.4.2 FS laser interactions in fused silica and other transparent solids

In transparent solids, the typical mechanism of FS laser-induced bulk material and surface damage is a combination of processes involving multiphoton ionization leading to coulomb explosion

[32,33]. Laser irradiation causes a jump of electrons from the valence band to the conduction band, resulting in ionization of the atoms [32]. These ions experience coulomb repulsive forces, which will eventually exceed the attractive bonds holding the material together, creating an explosion that causes damage [33]. Reference 32 provides some results to support this mechanism, as shown in fig. 1.8. The occupancy of the conduction bands within laser irradiated silicon material significantly increases as you increase the pulse fluence of a 30 fs laser pulse with wavelength 800 nm [32]. Reference 34 also supports an avalanche ionization mechanism for the laser-induced breakdown of fused silica.

Another interesting phenomenon that occurs at the surface of silica glass when interacting with ultrafast lasers is the formation of ripples or laser-induced periodic surface structures (LIPSS). In reference 35, they investigate the process of femtosecond laser ablation in silica glass, determining specific interactions between the laser and the glass. They found the creation of stress waves at the surface of the substrates, caused by a single ejected laser pulse. These stress waves were found to propagate through the material for some time after the initial laser pulse. This is corroborated by the descriptions provided in reference 36. Within the material itself, a filament was also created due to the deep penetrative ability of ultrafast laser pulses [35].

A number of different factors affect these mechanisms, including the presence of inclusions on the surface [37]. These are contaminating particles which could be introduced during the bonding process [23]. It is plausible then that inclusions may also be present at the interface of directly bonded substrates, as unbonded areas in these materials can be caused by contaminants. They prevent the surfaces of the substrates from coming into close enough contact for the bonding process to occur [23]. Contaminants can absorb or scatter laser light, which may cause additional damage at the interface or surface when irradiated with a laser [37].

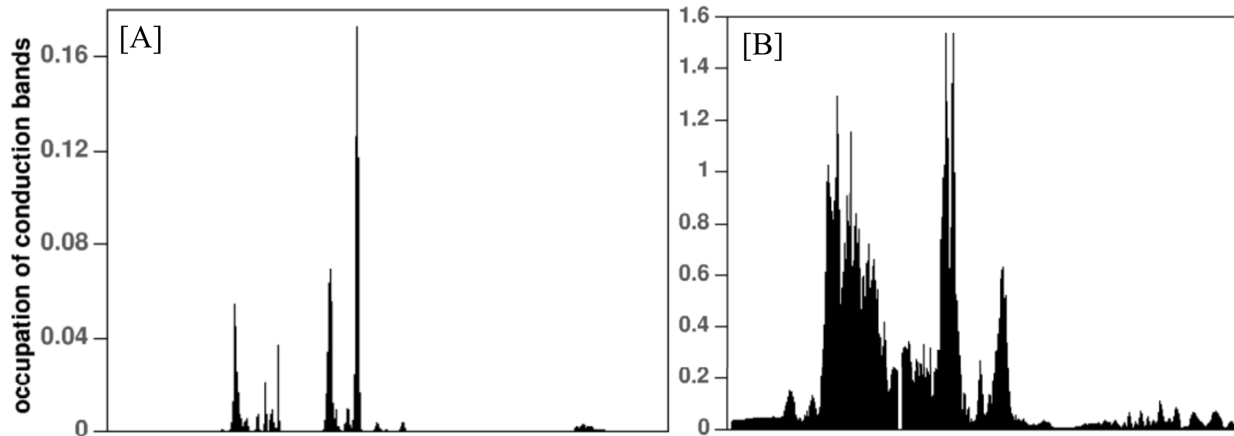


Figure 1.8: Occupancy of electron conduction bands within irradiated silicon material as laser fluence of 30 fs pulses with wavelength 800 nm is increased [32]. [A] Occupancy of electron conduction bands within irradiated silicon material at 0.9 J/cm$^2$ laser fluence. Occupancy is relatively low. [B] Occupancy of electron conduction bands within irradiated silicon material at 2.7 J/cm$^2$ laser fluence. Occupancy is much higher. Both graphs reproduced with permission.

## 1.5 Factors Affecting Laser Damage at the Interface of Bonded Materials

### 1.5.1 Average power density

The main parameter to be tested is average power density. As described in section 1.2, the focus of this research is the microchip, a bonded, coated optical material that will conduct and change the laser energy to output short pulses with high peak powers. Thus, testing the average power density the component can handle is important to determine an energy input at which the device operates without internal damage to the laser. This can be done quantitatively using the laser induced damage threshold (LIDT). This term is defined within ISO 21254 as the "highest quantity of laser radiation incident upon the optical component for which the extrapolated probability of damage is zero" [38]. While it is a useful tool for measuring bulk material damage limits, it must be used in conjunction with other factors. This is especially prevalent for laser irradiation at material surfaces and interfaces, since contaminants at the surface or interface may significantly decrease the LIDT relative to the bulk material [37]. Other factors need to be considered and controlled for to calculate an accurate LIDT. This is discussed in the following section, 1.5.2. LIDT is typically quantified in terms of laser fluence, a measure of energy density per unit area. Calculations for this are given in chapter two, section 2.6.2.

### 1.5.2 Other factors

Factors such as sample thickness, laser feed rate, and movement direction of the laser all have a significant effect on how damage appears in the material. The lasers used in this research are gaussian, which have a characteristic hourglass beam, as shown in fig. 1.9.

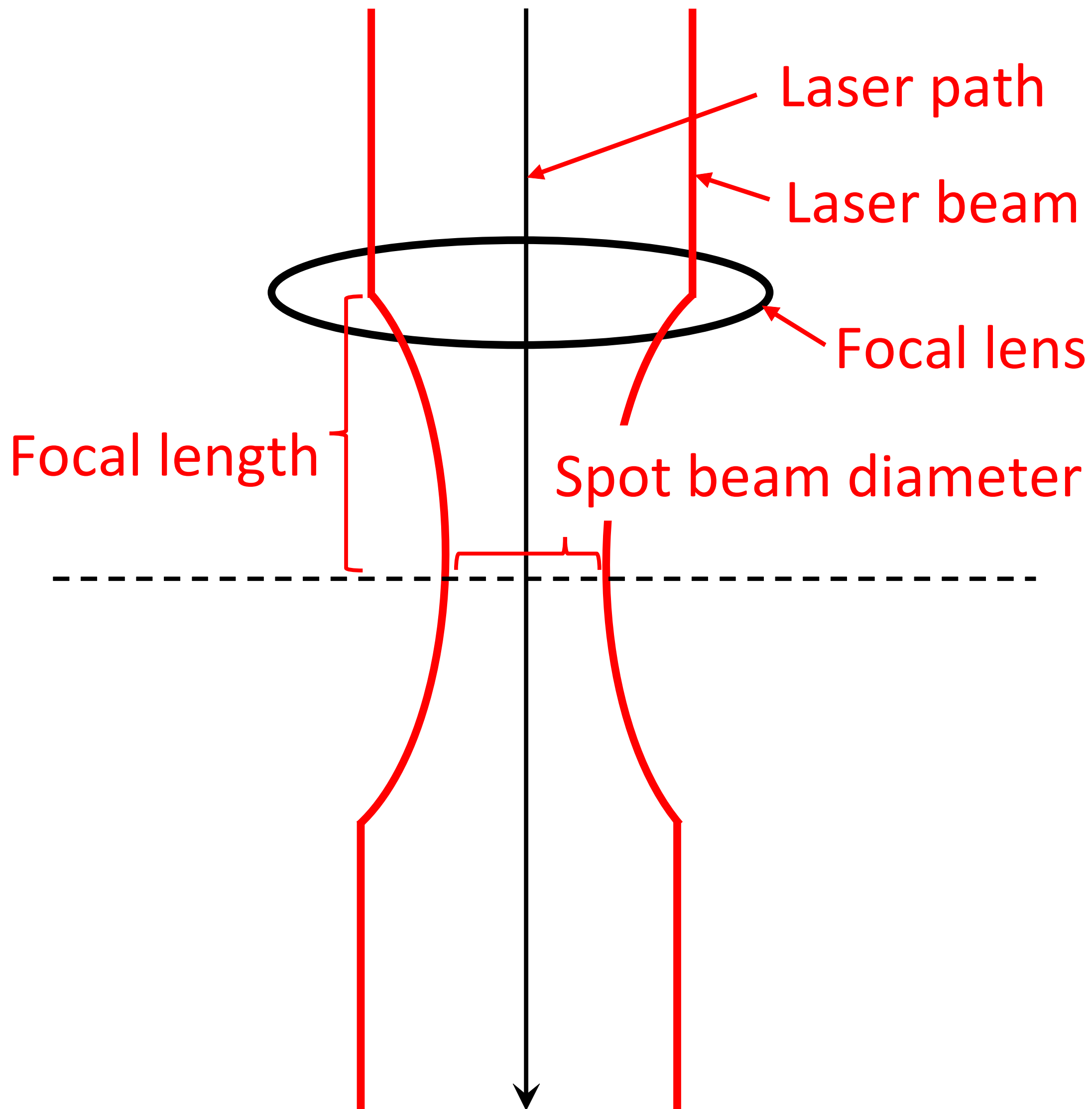


Figure 1.9: Diagram showing beam shape of focused gaussian laser used in this research. Note the hourglass shape that forms the focused laser spot.

In a thick glass sample, the radius of the beam (and thus the energy density) will be different at different heights within the sample, resulting in some points in the material showing more damage than others. Laser feed rate also affects laser damage within materials, as welding speed traditionally influences power density within different sections of material [39]. A higher welding speed results in less energy per unit area, whereas a lower welding speed results in more energy per unit area. In this same vein, movement direction is another key factor. In a 3-dimensional material, moving the focal point perpendicular to the beam propagation direction results in a different section of the material being irradiated at each point in time, resulting in a lower overall energy density per unit area. On the other hand, moving the beam parallel to the beam propagation direction ensures that the laser is constantly irradiating the same section of material, resulting in an overall higher energy density per unit area.

## 1.6 Scope and Objectives

For the design of ultrafast, pulsed, microchip lasers, coated and uncoated glass substrates need to be bonded directly to each other at low temperatures in order to preserve sensitive optical coatings within the bonding stack. Substrates need to be bonded without gaps or a filler layer at the interface, as any imperfections may affect the ability of the material to interact with the diode laser, resulting in laser damage within the material [12,13]. In order to evaluate how well a procedure produces these types of bonds, the bonding process needs to be evaluated on a number of different parameters, including mechanical strength and resistance to laser damage. Additionally, better understanding of the bonding mechanism would assist in any adjustments that may need to be made to the bonding process.

Thus the specific objectives are as follows:

1. Produce glass-to-glass bonds developed using a simple, low temperature chemical bonding procedure.
2. Investigate how differences in bonding pressure, annealing temperature, annealing time, and surface roughness affect bond strength.
3. Evaluate bond strength, mechanically and optically.
4. Modify the bonding process, when needed, to accomodate different materials, including soda-lime glass, fused silica, coated fused silica, and YAG.
5. Develop a cutting process to section the substrates into smaller pieces in order to accomodate mass production of the microchip lasers.
6. Using chemical analysis and imaging techniques, determine the mechanism through which the bonding process acts on the interface of the substrates, as well as visualize the appearance of features at the interface.

## 1.7 Chapter 1 Summary

I discussed the evolution of bonding, from cold welding to modern direct bonding applications in microfluidics, optics, and chemical analysis fields. Review of current literature highlights the need for a simple, low temperature bonding method, an essential component of a novel, ultrafast microchip laser design that was the motivation for this study. Background on factors affecting low temperature direct bonding, such as the chemical mechanism and surface roughness at the bonding interface were introduced. CW, PW, and ultrafast laser mechanics were described as well.

# Chapter 2: Sample Preparation

## 2.1 Cleaning Procedure

### 2.1.1 Concentration determination for the cleaning solution

The cleaning solution used to prepare the glass substrates is based on the classic RCA-1 method from the semiconductor industry used to remove organic contaminants and films from the surface of silicon wafers [40]. The cleaning solution also oxidizes the silicon, leaving a thin oxide layer that helps to ensure abundant silanol groups exist on the surface of the substrates for bonding [40]. The cleaning solution is a mixture of 1 part 28 % to 30 % ammonium hydroxide, 1 part 30 % hydrogen peroxide, and 5 parts deionized (DI) water. Prior to process optimization, 200 mL of DI water, and 40 mL of both 28 % to 30 % ammonium hydroxide and 30 % hydrogen peroxide were used. To better accomodate the smaller containers used in the experiments, these values were reduced, resulting in an optimized process using 120 mL of DI water and 24 mL of both 28 % to 30 % ammonium hydroxide and 30 % hydrogen peroxide.

### 2.1.2 General cleaning procedure

The process was conducted in a Hamilton SafeAire fumehood (Hamilton Laboratory Solutions, Manitowoc, Wisconsin, USA) in order to minimize contamination at the glass-to-glass interface and prevent escape of RCA fumes. First, a beaker filled with DI water was heated to 70 °C and checked with a thermometer or temperature sensor. The temperature was controlled at 70 °C as 28 % to 30 % ammonium hydroxide and 30 % hydrogen peroxide were added to the water. This mixture was left to rest for 1 min to 2 min to allow the solution to start bubbling. The glass substrates were then immersed in the solution for ≈15 min while swirling them occasionally. Afterwards, the glass substrates were rinsed in 28 % to 30 % ammonium hydroxide instead of the traditional DI water rinse [41]. A picture of the fumehood setup is shown in fig. 2.1.

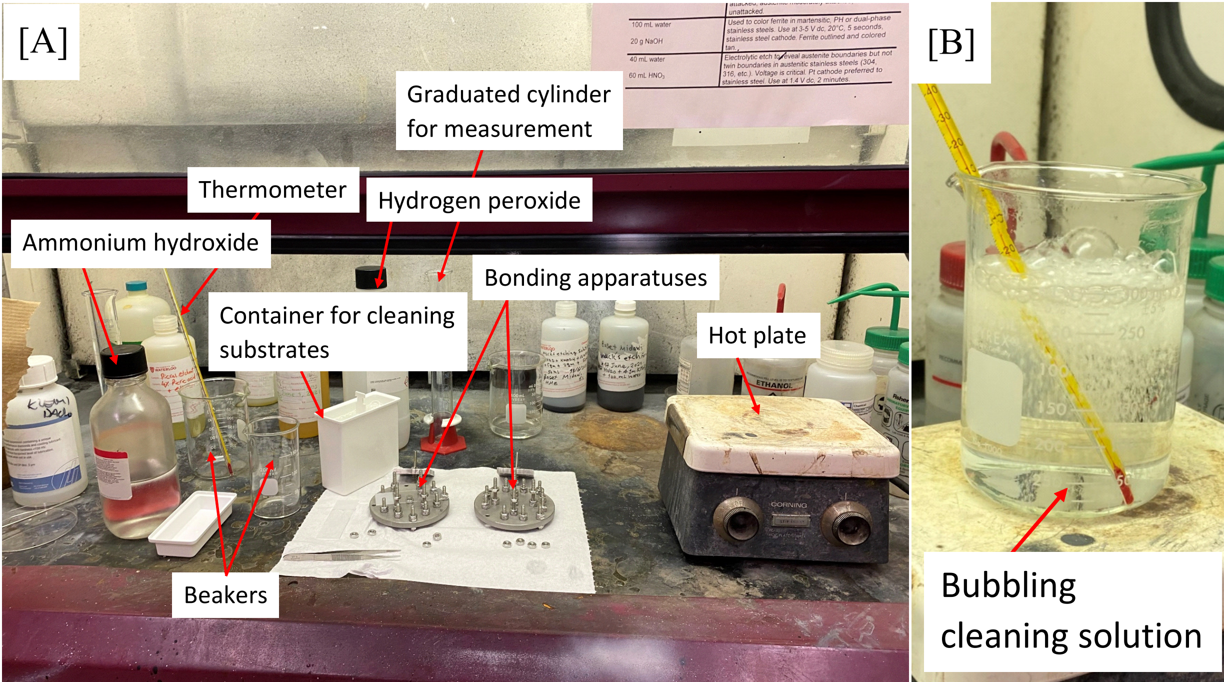


Figure 2.1: Fume hood workspace for creating the cleaning solution and applying it to the glass substrates. [A] Fume hood workspace, with all tools used in the experiments labelled. [B] Picture showing the cleaning solution after all chemicals have been combined at the correct temperature.

## 2.2 Bonding Procedure

### 2.2.1 General bonding procedure

After treating the glass with the cleaning solution in the fumehood, the samples were clamped with a unidirectional force using a custom bonding apparatus. The bonding apparatus is shown in fig. 2.2. The samples were wet mounted, meaning that they were not dried between cleaning and mounting. The bonding apparatus was designed in stainless steel to hold the samples under a constant, known force applied by a spring as they were bonded at various temperatures and pressures. Pressure was applied throughout the bonding process to increase the effective contact area, helping to overcome possible particle contamination and asperities [28,41]. Force applied to the samples was calculated using Hooke's Law for springs

$$F = kx \tag{2}$$

where $F$ is the force applied by the spring, $k$ is the reported spring constant (given by the manufacturer), and $x$ is the distance the spring is compressed. This force is then divided by the area of the head of the plunger to calculate the pressure applied to the glass substrates during the bonding process.

After clamping, the samples are heated to consolidate the bonds. The thermal treatment was conducted in a Binder precision oven (Binder, Tuttlingen, Germany) and temperature was monitored using 4-wire resistance readings from a resistive temperature detector. This oven setup is shown in fig. 2.3. Soda-lime glass and uncoated fused silica were used for a majority of the bonding. Parameters for each of these materials will be described in the following sections.

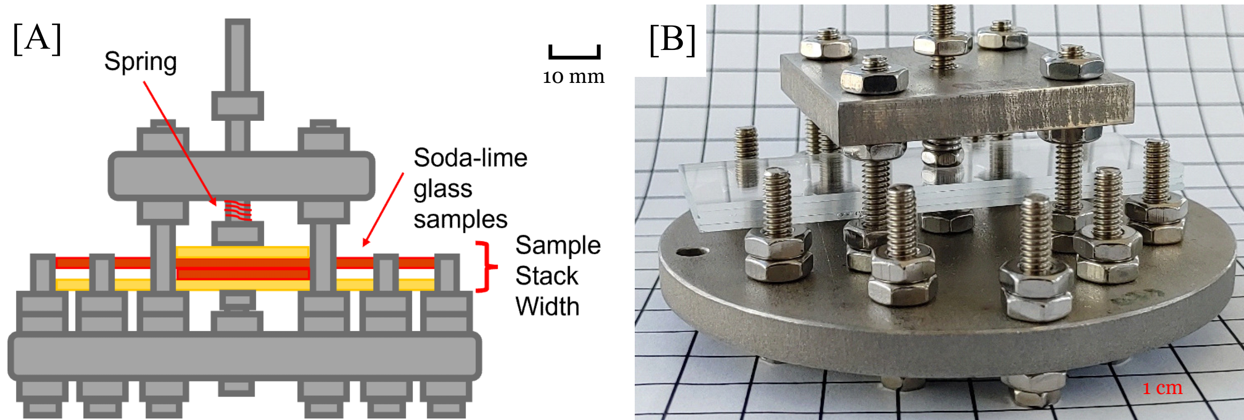


Figure 2.2: [A] Schematic diagram of clamping apparatus used for bonding process. Glass sample dimensions: Brand - Thermo Scientific, 1 mm × 76 mm × 26 mm, Brand - VWR, 1 mm × 75 mm × 25 mm [42,43]. Red represents the cleaned glass substrates, whereas yellow represents the uncleaned glass substrates. [B] Image of custom bonding apparatus clamping soda-lime glass samples. Note that the configuration of the glass substrates is different in the diagram versus the image.

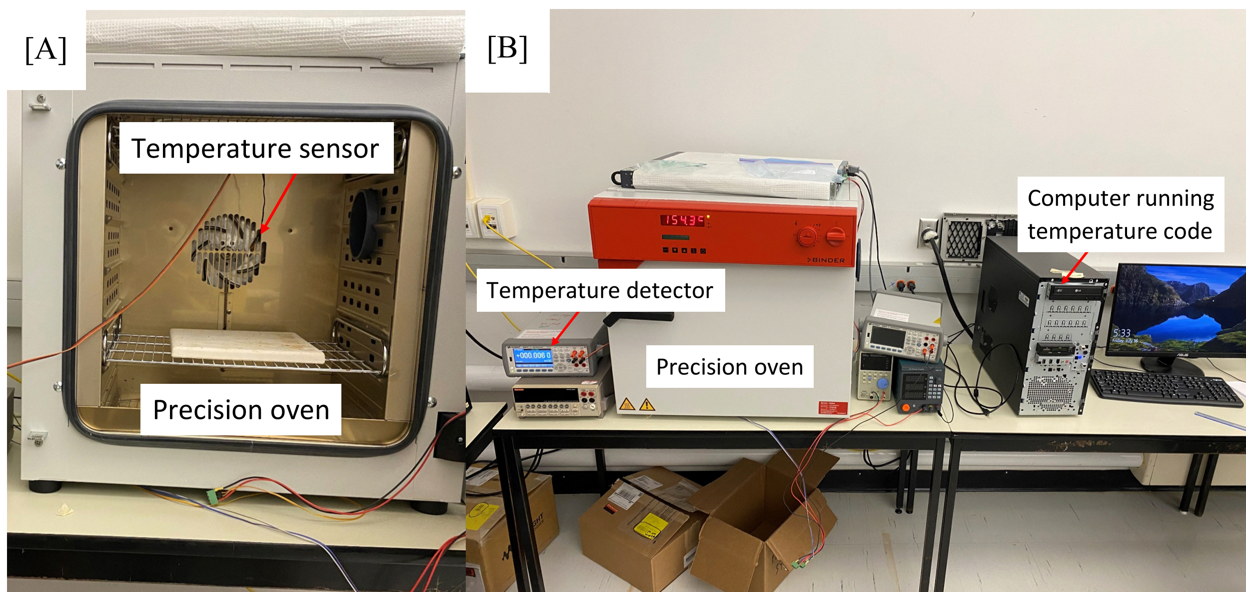


Figure 2.3: Thermal treatment setup used to bond glass to glass. [A] Inside of precision oven, showing temperature sensor that measures temperature of the oven. [B] Full thermal

treatment setup, showing temperature detector connected to temperature sensor, as well as computer used to run temperature measurement code.

### 2.2.2 Parameters used for soda-lime glass

The substrates were contacted in a number of different configurations, shown in fig. 2.4, to help accommodate the sample for the planned type of strength testing. Samples were bonded at temperature levels ranging from 40 °C to 300 °C, held for 30 min at a specified temperature, excluding an extra ≈7 min for temperature stabilization after the samples were placed into the oven. The force applied to the samples was about 26 N. Dividing this force by the area of the hexagonal plunger head gives a pressure of about 0.88 MPa. These parameters were chosen because after some initial shear testing, they created very consistently strong bonds [41]. The apparatus that applied this pressure is shown in fig. 2.2.

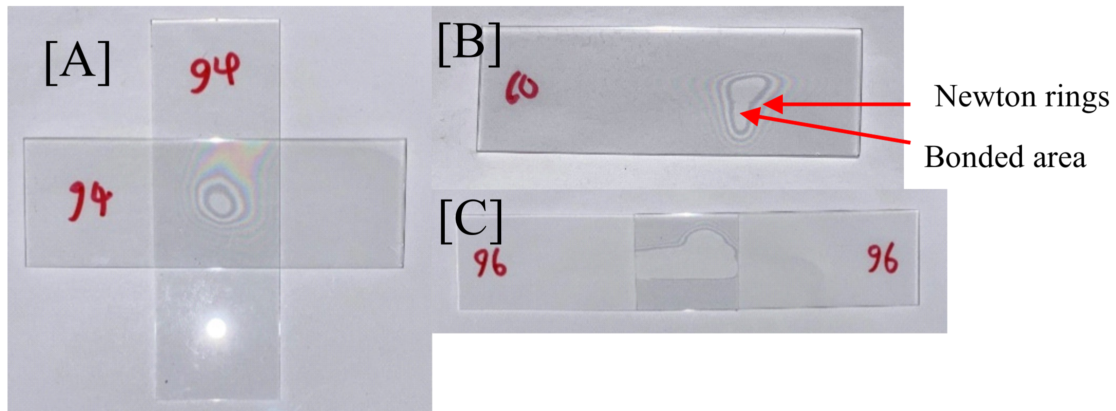


Figure 2.4: Various configurations used to bond the glass substrates. This was done to accommodate the bond strength testing method that each sample would undergo. [A] Initial configuration used during qualitative testing. Bonding was limited to a 3 cm × 3 cm area. [B] Complete overlap configuration. Offers the most opportunity for bonding since it has the greatest overlapping area. [C] Partial overlap configuration. Was originally designed for quantitative shear testing applications, but glass was too brittle to be gripped effectively. Ultimately the least used configuration.

### 2.2.3 Parameters used for fused silica pucks

These substrates were cylindrical samples of fused silica, including samples that were covered with optical coatings, and samples that were not. The substrates were 5 mm in thickness and 8 mm in diameter. After bonding, the samples doubled in thickness to 10 mm. Both coated and uncoated samples are shown in fig. 2.5. Since the samples are much smaller than the soda-lime glass samples, different configurations were not needed. Samples were bonded at a temperature of 180 °C, held for 30 min, excluding an extra ≈7 min for stabilization after the samples were placed into the oven. The force applied to the samples was about 36.9 N. Dividing this force by the area of the hexagonal plunger head gives a pressure of about 1.23 MPa. These parameters were chosen because after some initial shear testing, they created very consistently strong bonds. The appara-

tus that applied this pressure is shown in fig. 2.2, although because of the thickness, the plunger head needed to be moved upwards to accomodate the samples.

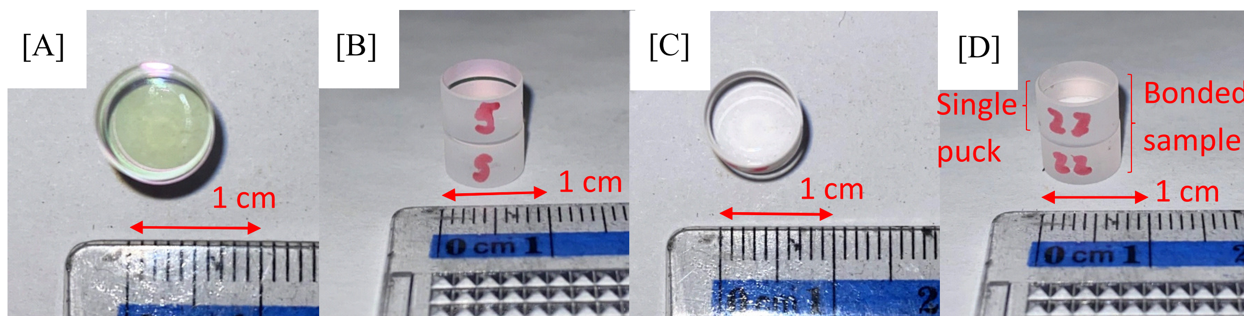


Figure 2.5: [A] Top view of coated fused silica sample. Coating causes surface to appear green. [B] Side view of coated fused silica sample. [C] Top view of uncoated fused silica sample. [D] Side view of uncoated fused silica sample. An example of a single puck and full bonded sample is shown in this image.

### 2.2.4 Iterations of the bonding apparatus

The bonding apparatus went through several modifications before reaching the final design. In the first design, scrap steel was used to expedite the construction process. Unfortunately, after several heat treatments, the steel began to oxidize (fig. 2.6), which placed the samples at risk for contamination. The apparatuses were eventually changed to stainless steel, which was shown to resist repeated temperature treatments much more effectively. This design is shown in fig. 2.2.

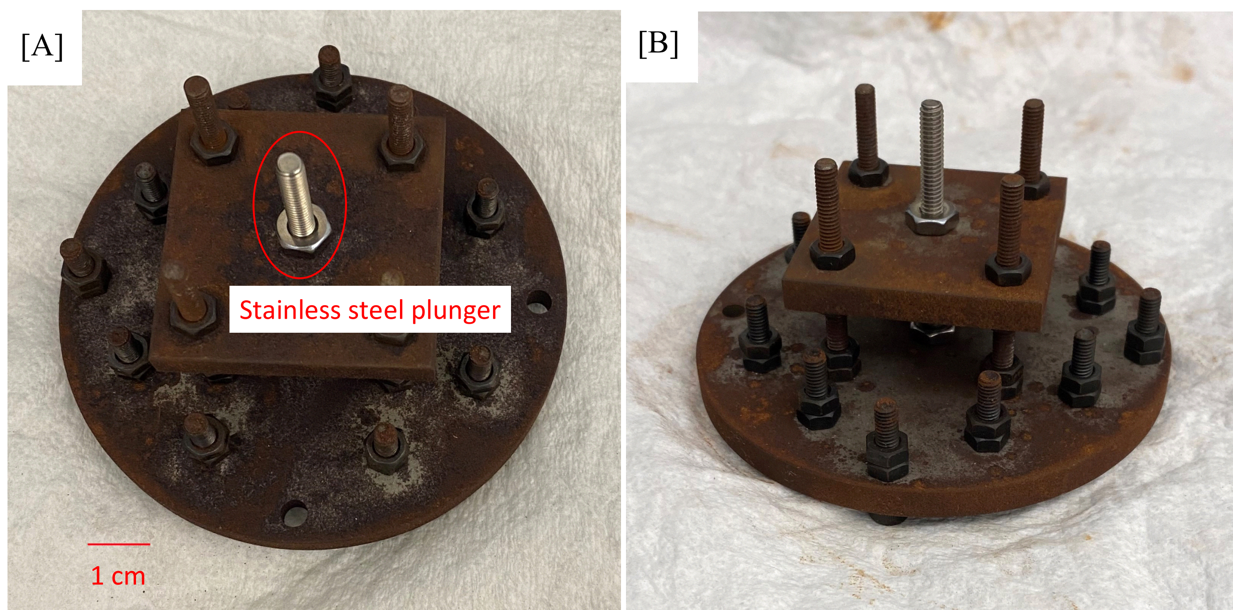


Figure 2.6: Oxidation present on the first design of the bonding apparatus. [A] Top view of the bonding apparatus. Stainless steel plunger used shows resistance to repeated heat treatments relative to scrap steel. [B] Side view of bonding apparatus.

While the apparatus in fig. 2.2 succeeded in bonding the samples well, it was not suitable for mass production, which is essential for the microchip laser design. Modifications were made to produce a newer bonding apparatus, which can accomodate five fused silica bonding samples instead of one. This design is shown in fig. 2.7.

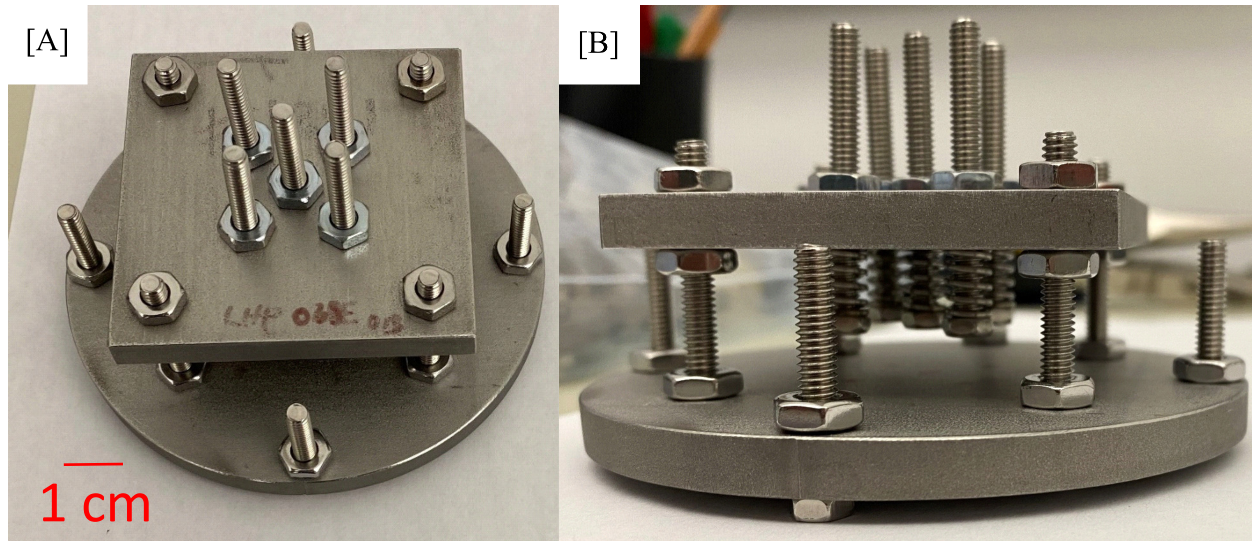


Figure 2.7: Pictures of newer bonding apparatus. [A] Top view of apparatus. [B] Side view of apparatus. Note that there are five plungers to apply pressure to five different samples.

The design widens the top plate to accomodate five plungers instead of one. This increases the efficiency of the workflow by allowing five samples to be bonded at once.

## 2.3 Surface Roughness Characterization

### 2.3.1 Optical profiler interferometry

Surface roughness was measured initially using interferometry, as it was easily accessible and produced an easy to interpret image of the sample surface. A WYKO NT1100 Optical Surface Profiler (Veeco, Plainview, New York, USA) was used. This optical profiler is shown in fig. 2.8a. As will be discussed in chapter three, interferometry was able to detect imperfections on the surface of glass samples, but struggled with determining the actual surface roughness due to artifacts produced by the transparency of the glass samples. These results are discussed in section 3.1.1.

### 2.3.2 Atomic force microscopy (AFM)

Atomic force microscopy (AFM) was used as a more accurate method to determine the surface features of the glass samples, as has been done in previous studies [44-47]. Since AFM uses mechanical means to measure the surface roughness, it wouldn't be affected by the transparency of the glass samples. A JPK NanoWizard II AFM was used in intermittent contact mode with a line rate of 0.7 – 0.9 Hz, with the HQ:NSC14/AL BS AFM probes from µMasch (resonance freq. 160 kHz). The Gwyddion Software [48] was used for surface roughness (RS) analysis of the AFM

images. In Gwyddion, RS is expressed as the mean square roughness (RMS) of height irregularities which is calculated using the 2nd central moment of the data values [48]. 2D FFT filtering was used to remove background noise and the plane background was also removed to properly level the images [48]. All data analysis was performed on images after applying only the mentioned filters to best preserve the raw data while eliminating the impact of noise and unleveled background. A picture of the AFM is shown in fig. 2.8b. AFM results are discussed in section 3.1.2.

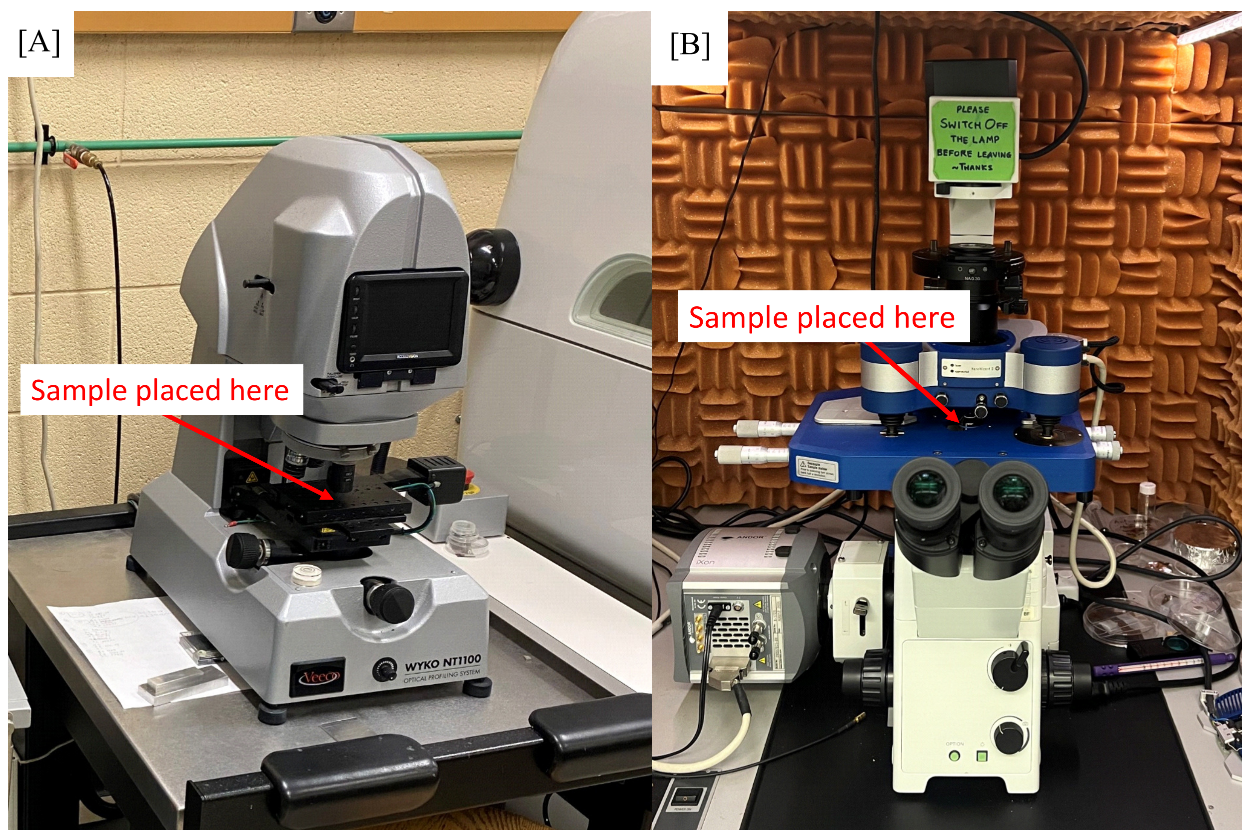


Figure 2.8: Optical profiler and AFM used to gather surface roughness data for the glass substrates. [A] Optical profiler used to gather surface roughness data. [B] AFM used to gather surface roughness data. Two methods were used to ensure accuracy of the results. AFM picture provided courtesy of Nanqin Mei.

## 2.4 Bonding Interface Visual and Chemical Analysis

### 2.4.1 X-ray Photoelectron Spectroscopy (XPS) Analysis

The chemical composition of the bonding interface was investigated in order to confirm the chemical mechanism of our bonding procedure. Surface species at the bonding interface were detected using X-ray photoelectron spectroscopy (XPS). The instrument used was a Thermo-VG Scientific ESCALab 250 microprobe (Thermofisher, Waltham, Massachusetts, USA). Data was analysed using CasaXPS software, after calibrating the data by setting the true value of the C 1s

high resolution readings to 284.8 eV, the adventitious carbon [49]. These results are discussed in section 3.2.1.

### 2.4.2 Scanning Electron Microscopy (SEM) and Energy Dispersive X-ray (EDX) Analysis

The SEM used in this experiment was a combination system of SEM and EDX, allowing for both scanning electron imaging and elemental composition analysis of the bonding interface. The SEM used was the FEI Quanta Feg 250 Environmental SEM with EDX (FEI, Hillsboro, Oregon, USA). The samples were carbon taped to SEM dies for stability and run in a vacuum to produce a high quality image. The SEM images and EDX analysis results for all materials are shown in section 3.2.2.

## 2.5 Tensile Shear Testing

In order to test the mechanical strength of the bonds produced using our bonding method, destructive shear tensile testing was done. A micro tensile tester (Instron 5548 Micro Tester, Instron, Norwood, Massachusetts, USA) in compression mode was used. This tensile tester was located in E3-2169 at the University of Waterloo. For each of the different materials, a different setup was used. These results are discussed in section 3.4.

### 2.5.1 Soda-lime glass shear testing

A diagram of the destructive test setup is given in fig. 2.9. Shear strength was calculated by dividing the force load that a given sample could handle before breaking by the total bonded area of the sample. The total bonded area was determined using GIMP image processing software (https://www.gimp.org/) to measure pixel distances of the bonded area, converting them to metric units using a known scale. If the bonded area was too large to be tested effectively, the sample bonding configuration was changed or the samples were cut using a carbide scriber so a smaller subset of the total area could be tested. Interface and bulk breaks were confirmed based on damage location [41]. Fig. 2.10 shows examples of damage that would be classified as originating at the interface or bulk material.

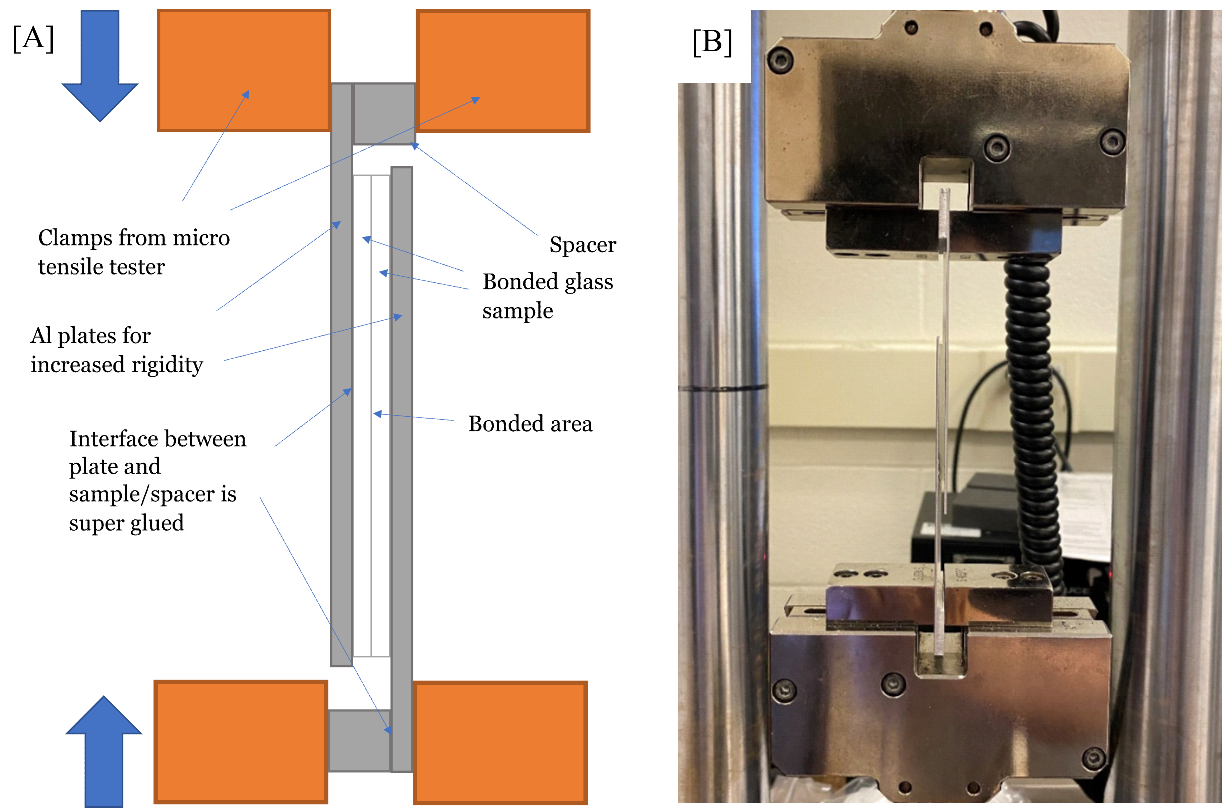


Figure 2.9: Diagram of tensile testing setup for soda-lime glass. Bonded samples were glued to aluminium plates with super glue to increase rigidity of the samples for testing. Samples were compressed at 1 mm/min until failure at the bond site or bulk material. Samples that broke before force was applied or broke at the glue bond were not considered in the results. This method is based on the testing method reported in reference 23. [A] Labelled diagram of tensile testing setup. [B] Actual tensile testing setup.

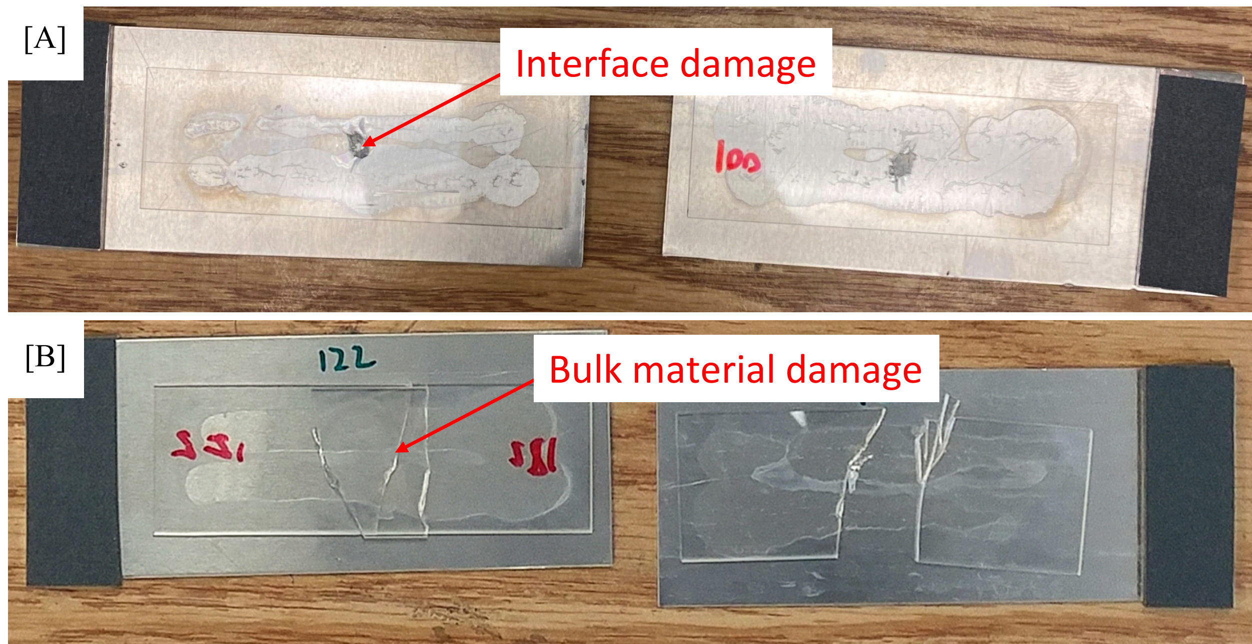


Figure 2.10: Examples of interfacial and bulk material damage after shear testing. [A] Shear damage at the center of the sample. If damage appeared only in this center area after shear testing, failure at the interface occurred. [B] Shear damage in the bulk material. If the center remained intact and damage occurred elsewhere, failure in the bulk material occurred.

Because pressure is only applied to the center of the soda-lime glass samples during bonding, shear damage at the bonding interface would only be seen at the center of the sample (fig. 2.10a). On the other hand, if stresses resulted in damage at a location other than the interface, significant bulk material fracturing would be observed (fig. 2.10b).

### 2.5.2 Fused silica shear testing

A diagram of the destructive test setup is given in fig. 2.11. The shear strength was calculated in the same way as the soda-lime glass samples. However, unlike the soda-lime glass samples, the entire surface area of the fused silica pucks is expected to be bonded, due to the thickness and smaller size of the glass substrates. Bulk material breaks were not prevalent because of the smaller size of these glass substrates as well. Some examples of fractured samples (both coated and uncoated fused silica) are shown in fig. 2.12.

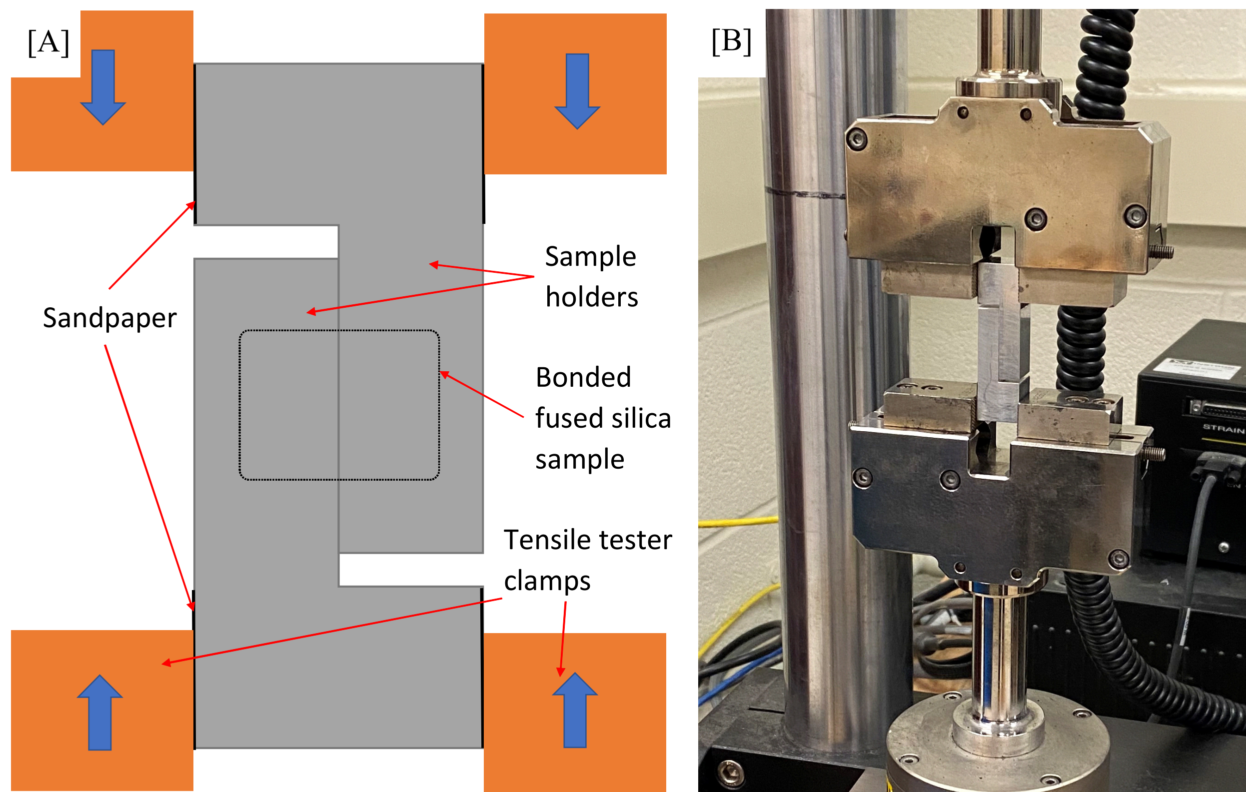


Figure 2.11: Shear testing setup designed for fused silica samples, both coated and uncoated. [A] Labelled diagram of shear testing setup. Samples are tested in compression mode, and compressed at a rate of 0.5 mm/min. [B] Picture of actual shear testing setup before compression is started.

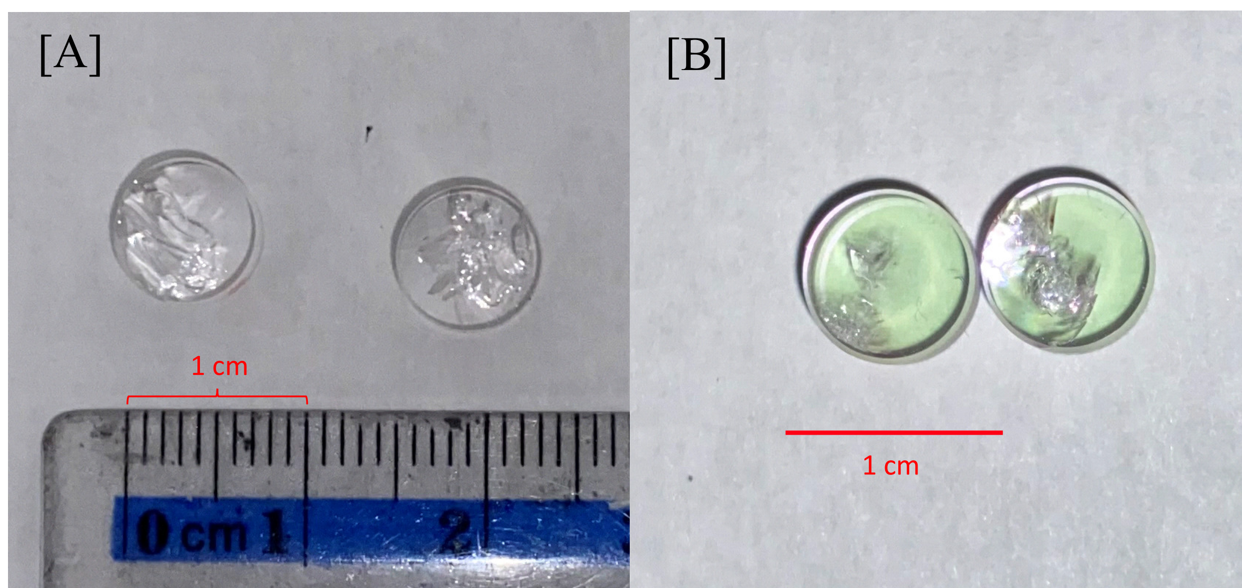


Figure 2.12: Examples of fractured coated and uncoated fused silica bonded samples after shear testing. [A] Image of uncoated fused silica pucks shows damage after shear testing on

both sides of the interface. [B] Image of coated fused silica pucks shows damage after shear testing on both sides of the interface.

## 2.6 Laser Induced Damage (LID) Testing

### 2.6.1 Continuous wave (CW) laser damage setup

To test the optical robustness of the bonds, the bonds were irradiated with a powerful CW welding laser. The laser setup is shown in fig. 2.13. The laser used was an IPG YLR-500 Ytterbium CW Fiber Laser (IPG Photonics, Oxford, Massachusetts, USA). The focused, gaussian laser had a nominal wavelength of 1070 nm, a maximum power of 500 W, and a core fiber with 50 µm diameter. At the time of laser installation, the beam spot was measured to have a radius of 37.2 µm [41]. An updated measurement was not available at the time of writing. Both soda-lime and fused silica samples were tested with progressively increasing powers and dwell times, until damage/delamination occured at the bonding interface. These results are discussed in section 4.1.

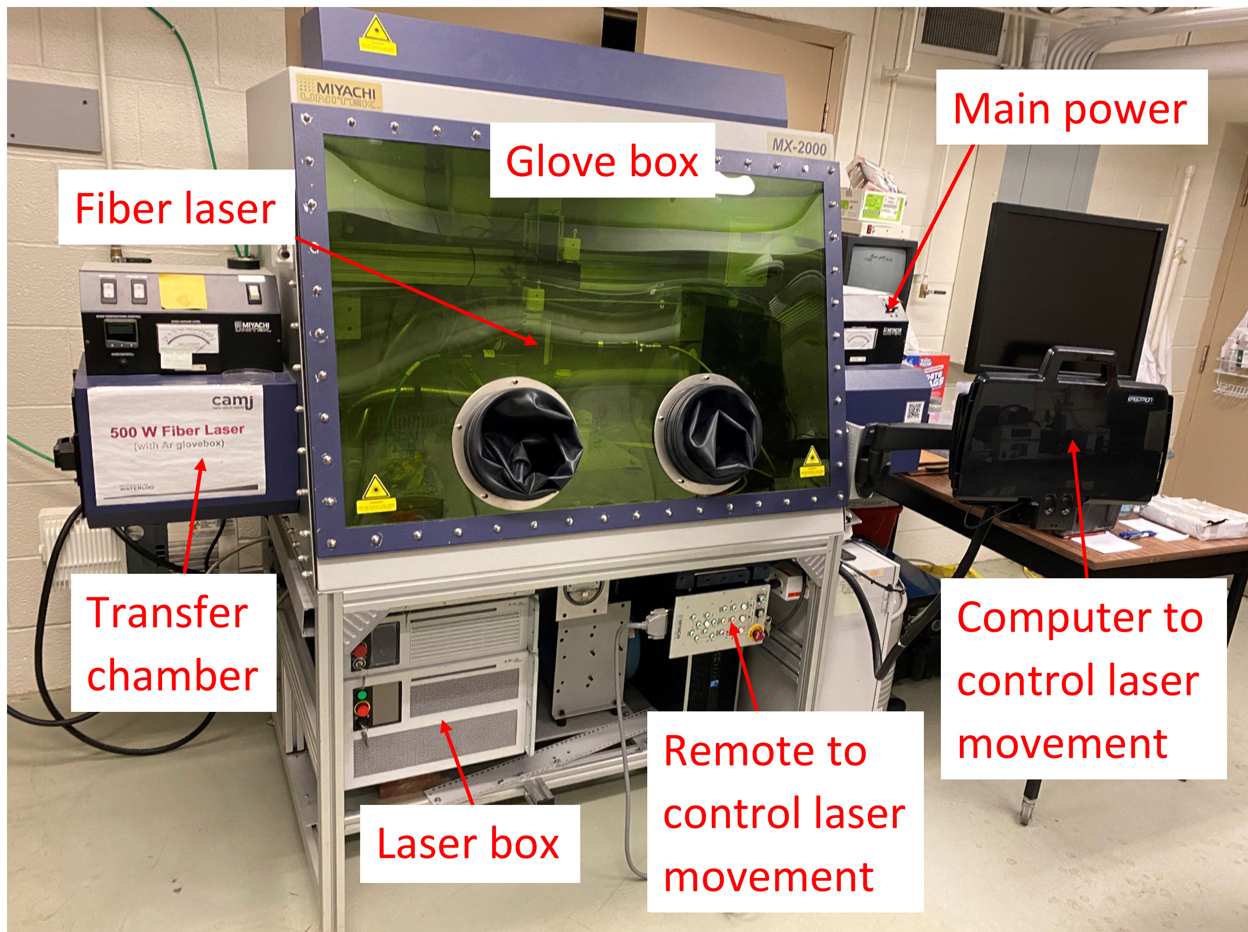


Figure 2.13: CW laser testing setup for both soda-lime glass and fused silica samples. Laser is encased by an atmosphere-controlled glove box. Notable features of the box and the laser itself are highlighted.

### 2.6.2 Femtosecond (FS) laser damage setup

Laser damage tests with short pulsed lasers also needed to be done, since our microchip laser design is for a pulsed laser. The FS laser setup is shown in fig. 2.14. The laser is an mks Spectra Physics Spitfire Ace Pulsed FS Laser (Spectra Physics Inc, Milpitas, California, USA). The focused, gaussian laser has a nominal wavelength of 800 nm, a maximum pulse energy of 4 mJ, and a pulse repetition rate of 1 kHz. The pulse duration is about 35 fs. The beam spot size depends on the focal lens used. For a 20 cm focal lens, the calculated spot size should be around 20 µm [50]. For a 5 cm focal lens, the calculated spot size should be around 5 µm. Both soda-lime and fused silica samples were irradiated and evaluated on certain characteristics (ex. width of interface damage relative to bulk damage, relative colourmetric data values) while increasing laser power, in order to evaluate LIDT and LID in bulk and bonded samples. Laser power was quantified by calculating laser fluence. The equation for laser fluence [51] is defined as

$$Laser\ Fluence\ \left(\frac{J}{cm^2}\right) = \frac{Laser\ \ Energy\ \ (J)}{Effective\ \ Focal\ \ Spot\ \ Area\ \ (cm^2)} \tag{3}$$

where laser energy is determined by the equation

$$Laser\ Energy\ (J) = \frac{Average\ \ Power\ \ (W)}{Repetition\ \ Rate\ \ (Hz)} \tag{4}$$

where average power can be measured using a power meter, and repetition rate is a characteristic of the laser itself. On the other hand, effective focal spot size (assuming the laser is an ideal gaussian beam) can be calculated using the equation [52]

$$w_f = \frac{\lambda f}{\pi w_0} \tag{5}$$

where...

$w_f$ is the beam diameter
$f$ is the focal length of the laser system
$w_0$ is the waist of the unfocused beam
$\lambda$ is the wavelength of the laser

All these parameters can be obtained experimentally or is a characteristic of the laser. Using the beam diameter, the focal spot area can be calculated using the equation for the area of a circle ($\pi r^2$). The results for these pulsed laser experiments are discussed in section 4.1.

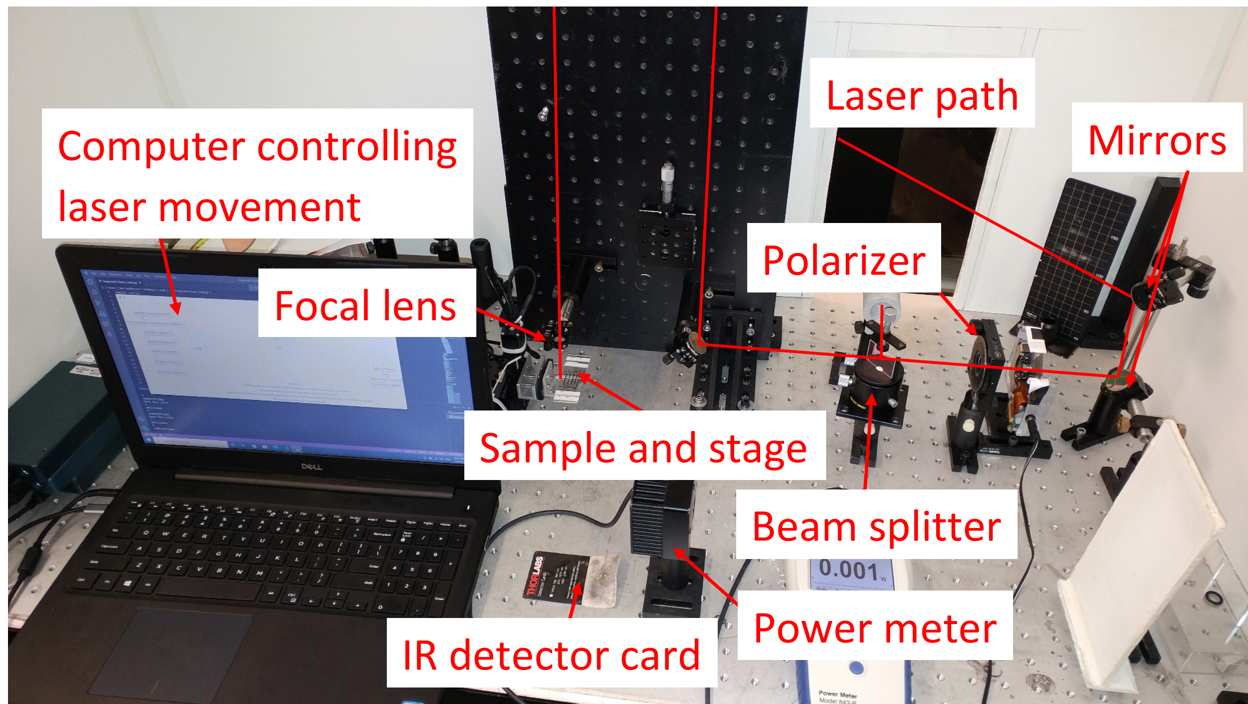


Figure 2.14: FS laser testing setup for both soda-lime glass and fused silica samples. Laser is directed into the work area via several mirrors and focused using a 20 cm or 5 cm focal length lens. Important parts of the setup, such as control systems for 3-axis movement and power control using beam splitting and polarization are labelled.

## 2.7 Chapter 2 Summary

A modified RCA-1 method was used to join glass samples through direct bonding. Bonding parameters for soda-lime glass and fused silica samples were introduced, including pressure applied during annealing and design of the bonding apparatuses to accomodate the geometry of the samples. Optical interferometry and AFM were used to evaluate surface roughness. XPS, SEM, and EDX were used to determine the visual quality and chemical activity at the bonded interface. Mechanical evaluation of bond quality was done through destructive shear testing. Optical bond quality evaluation was done through LID testing.

# Chapter 3: Properties of the Bonded Interface

As described in the introduction, two of the major factors affecting low-temperature bonding of glass substrates is the surface roughness at the interface of the samples, as well as the chemical composition of the interface. These will both be characterized in the following sections, followed by an analysis of the shear strength of these samples.

## 3.1 Surface Roughness Testing

### 3.1.1 Interferometry-based optical profiler results

To evaluate surface roughness of the glass samples, interferometry was used. This method was easily accessible and required very little calibration. The surface roughness of 3 different materials (soda-lime glass, uncoated fused silica, and coated YAG[1]) were evaluated. The results can be seen in fig. 3.1, 3.2, 3.3 below. Initially, the surface roughness of the samples seemed to make sense. Soda-lime glass samples had clear waviness present in the 2D contour plot, which was expected because of how soda-lime glass is made. Since they are floated on top of a liquid before solidifying, it is not unexpected that they would have a wavy surface appearance [53]. The RMS surface roughness also made sense when different materials were compared, as the uncoated fused silica samples should have a lower overall RMS surface roughness than the soda-lime glass, as they are polished beforehand, whereas the soda-lime glass samples are not. The presence of surface imperfections were also detected on samples of coated YAG (fig. 3.3), providing evidence for why these samples were not capable of strong bonding, the main reason for their investigation.

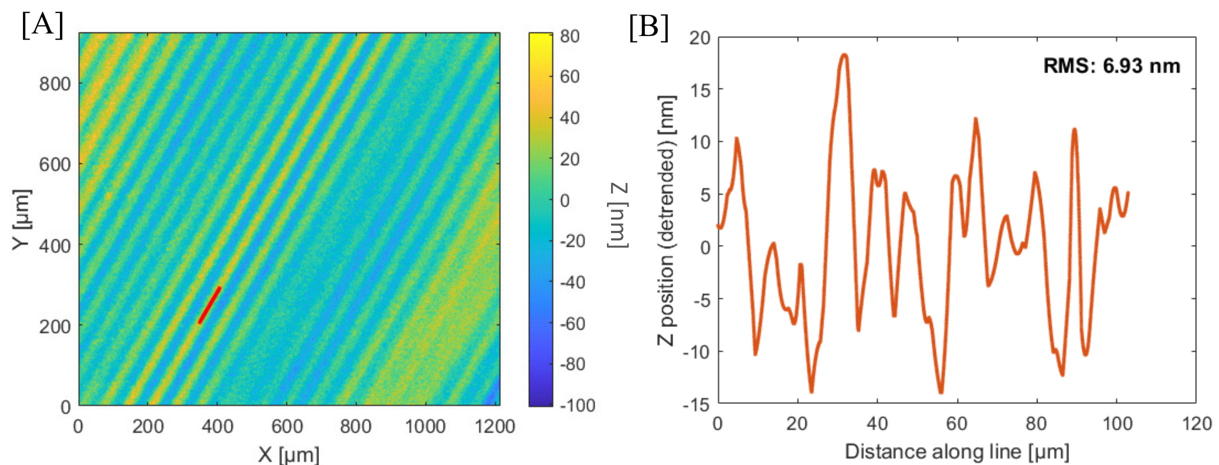


Figure 3.1: Example of optical profiler surface roughness results for soda-lime glass before cleaning. [A] The micrograph on the left shows a 2D representation of the surface roughness. [B] The graph on the right shows the detrended surface roughness over a single ridge for about 100 μm. This ridge distance is highlighted by the red line in the micrograph.

1. YAG material coated with fused silica and other components. Similar composition to active material to be used in microchip laser design.

However, further tests with other materials (fig. 3.2, 3.3) and review of the literature raised a few questions as to the validity of the results. The RMS surface roughness of the example soda-lime glass sample was measured to be 6.93 nm. However, according to previous literature, bonding can only occur at much lower RMS surface roughnesses, specifically between 0.3 nm to 0.9 nm per micron squared [5,10,20,41,54].

This may be due to errors in the measuring method itself. Since glass is transparent and interferometry is a light based method, the measurement of the glass surface may not be entirely accurate. All samples seemed to show a wavy surface pattern that was expected in the soda-lime glass results, but should not be present in the uncoated fused silica and coated YAG results. These samples have a different manner of manufacturing that would not produce the wavy surface features observed. Additionally, when the samples are rotated, surface features would be expected to move. It was observed that while the features did rotate, they did not do so uniformly, providing evidence that the waviness I observed in the glass samples are artifacts of the measurement method, rather than actual features. To confirm this, atomic force microscopy (AFM) was used.

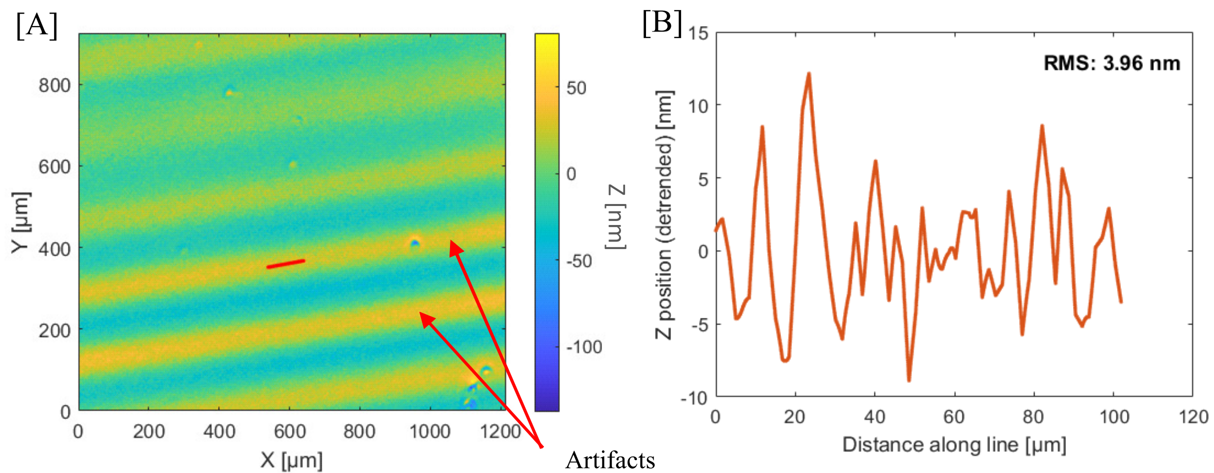


Figure 3.2: Example of optical profiler surface roughness results for uncoated fused silica before cleaning. [A] The micrograph on the left shows a 2D representation of the surface roughness. [B] The graph on the right shows the detrended surface roughness over a single ridge for about 100 µm. This ridge distance is highlighted by the red line in the micrograph. Surface roughness artifacts are also labelled.

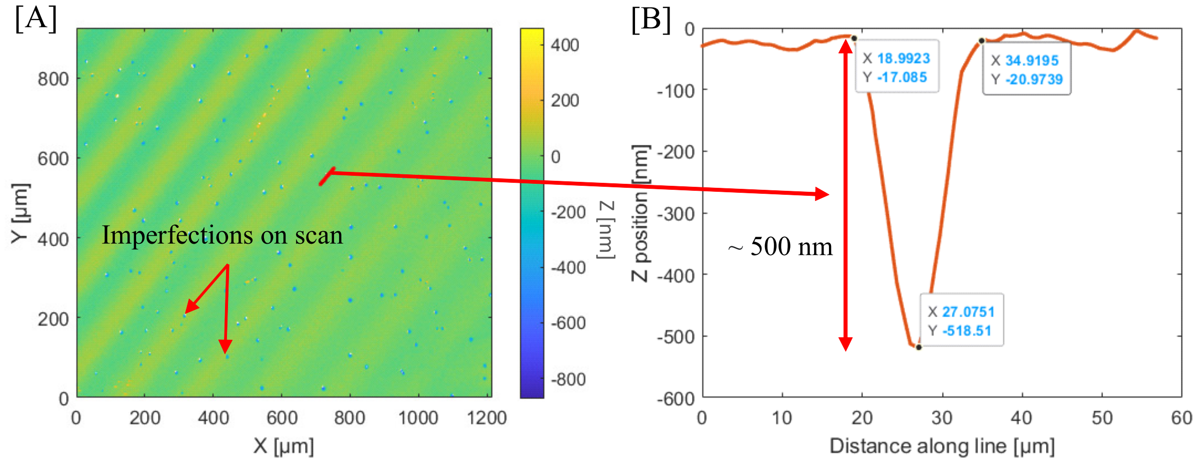


Figure 3.3: Example of optical profiler surface roughness results for coated YAG after cleaning. [A] The micrograph on the left shows a 2D representation of the surface roughness. [B] The graph on the right shows the surface profile across one of the imperfections along the surface. The surface profile reveals a deep hole in the surface of the sample. This profile is highlighted by the red line within the micrograph.

### 3.1.2 Soda-lime glass AFM surface roughness results

Figs. 3.4 and 3.5 are AFM topography images and height profiles for soda-lime glass samples before and after applying the cleaning process. The cross-sections of the surface (figs. 3.4b, 3.5b) for each image together with the 3D views (figs. 3.4c, 3.5c) show that the largest height difference between the low and high features of the sample before cleaning is close to 3 nm; that of the sample after cleaning is close to 6 nm. The surface before cleaning (fig. 3.4) had an RMS surface roughness of 262.9 pm, whereas the surface after cleaning (fig. 3.5) had an RMS surface roughness of 525.2 pm. The values are similar to what is reported as typical RMS surface roughness values for bonding in literature, ranging from 0.3 nm to 0.9 nm for an area of 1 µm squared [5,10,20,41,54]. While other studies report much higher surface roughnesses (6 nm), they do not specify how the values were measured, making them difficult to compare [9]. Our cleaning process does not noticeably affect RMS surface roughness as both values before and after cleaning fall within the typical range for bonding (or lower), providing evidence that supports the direct bonding mechanism [27,41]. These surface roughness readings also suggest that the RMS surface roughness readings measured using interferometry are likely incorrect, as the AFM results are more consistent with previous results found in literature.

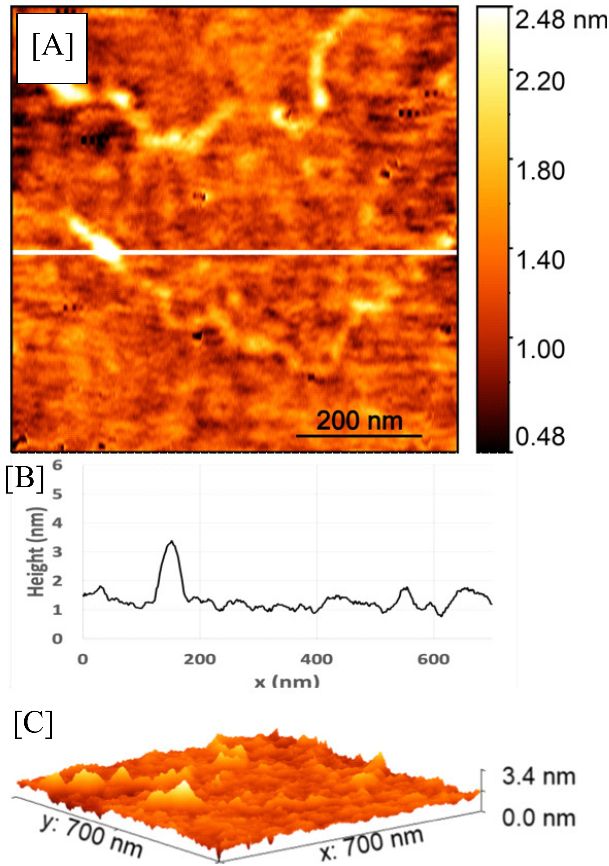


Figure 3.4: [A] AFM topography image of the sample before applying the cleaning process. The image is 700 nm × 700 nm in scale. [B] Cross-sectional profile of the selected white line in the image in part A. [C] 3D view of the sample surface.

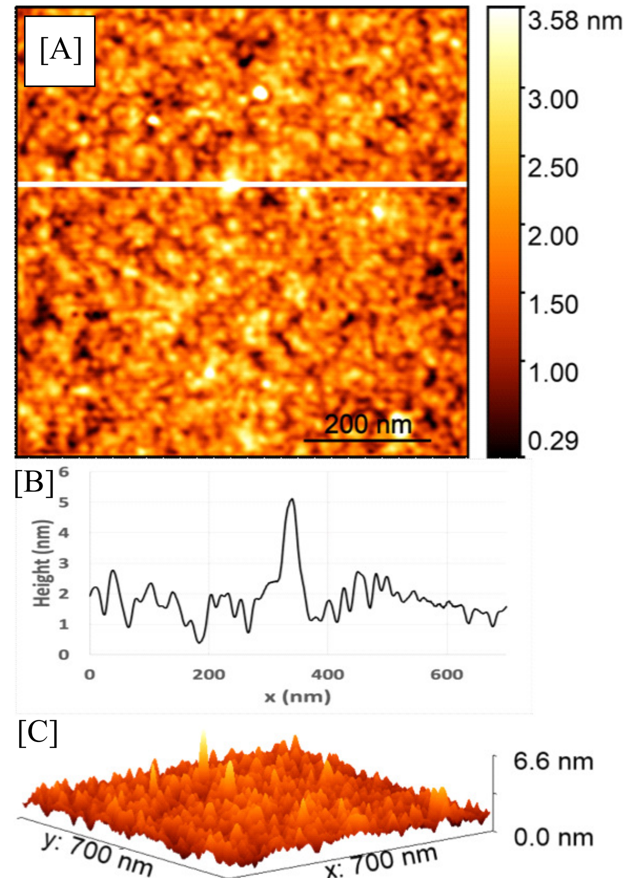


Figure 3.5: [A] AFM topography image of the sample after the cleaning process. The image is 700 nm × 700 nm in scale. [B] Cross-sectional profile of the selected white line in the image in part A. [C] 3D view of the sample surface.

## 3.2 Analysis of Bonding Interface

### 3.2.1 X-ray photoelectron spectroscopy (XPS) analysis

The other major factor that needs to be considered with bonding at the interface of glass substrates is the chemical composition and bonding mechanism. As mentioned in the introduction, there exists on the surface of glass a vast number of silanol groups [23,27]. These groups form when silicon is exposed to ambient water in the air, resulting in increased hydrophilicity of the glass surface [27]. This property encourages the surface groups of glass substrates to form hydrogen bonds. Such bonds can bridge across the interface of two glass surfaces when they are brought close together, creating temporary links that can be converted to stronger, permanent covalent bonds through a condensation reaction activated by thermal treatment [23,27]. With the modified RCA-1 chemical treatment, Si-O-Si/Si-N-N-Si bonds can form, with water/$NH_3$/$H_2$ as a byproduct [5,9,27]. Any of the byproducts are expected to be driven out of the interface to allow an even

more intimate level of contact between the glass substrates, which is required for covalent bond formation [27,29]. This is the direct bonding mechanism for our cleaning method. It is supported by reference 9, where they also used an RCA-1 based cleaning method. A model summarizing the bonding mechanism is given in fig. 3.6.

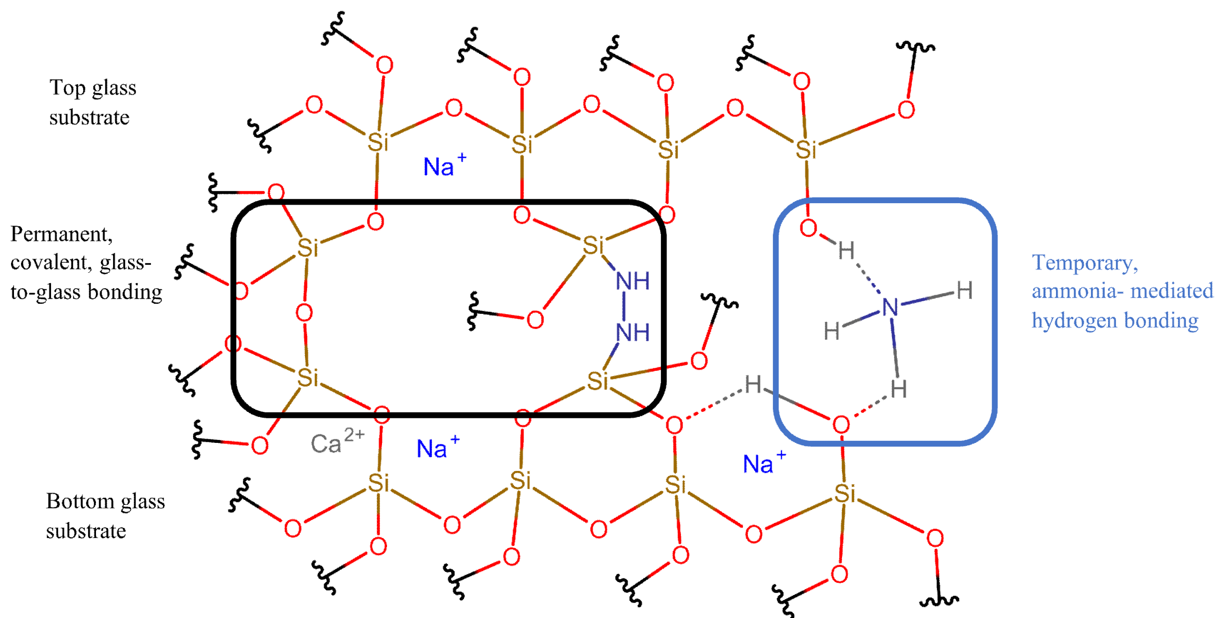


Figure 3.6: Model of microscopic bonding mechanism at the glass-to-glass interface, based on high resolution XPS results and model outlined by reference 9. The mechanism shows the structure of temporary hydrogen bonding formed before thermal treatment (right), as well as permanent covalent bonding (Si-O-Si and Si-N-N-Si bonds) that occurs after thermal treatment (left) [9,27]. Ammonia is presented as a hydrogen bond mediator in this image because an ammonium hydroxide rinse was used in our experiments. In the traditional RCA-1 cleaning rinse, interfacial hydrogen bonding is mediated by water. Illustration was created using Chemspace (https://chem-space.com/real-space).

The direct bonding mechanism is supported by the XPS results shown in fig. 3.7. A broad XPS scan before (fig. 3.7a) and after (fig. 3.7b) cleaning was done first to observe the general composition of the soda-lime glass. The major observations of note are the presence of large amounts of oxygen and silicon, as well as the presence of nitrogen in the sample after applying the cleaning process to the surface. All of these elements are necessary to facilitate the direct bonding mechanism. Looking more closely at the high-resolution nitrogen XPS results (fig. 3.7, c and d), the presence of a nitrogen peak at the cleaned sample interface which is absent before cleaning suggests the incorporation of nitrogen species into the substrates due to the cleaning procedure. These samples had also been left to sit in ambient air for about 48 hours prior to testing, supporting the idea that the detected N is likely residual N incorporated into the surface by the ammonium hydroxide bath, subsequently facilitating the bonding mechanism through Si-N-N-Si bonds [9,55,41,56]. Peak intensity was around 399.81 eV, which, according to reference 56, is close to the bonding energy for H-N-H bonds (399.7 eV) and Si-N bonds (400.9 eV). From data in the

NIST XPS database, Si-$NH_2$ bonds (397.5-398.6 eV) and/or $NH_3$ bonds (398.6-399.6 eV) at the interface may also be present [41,55].

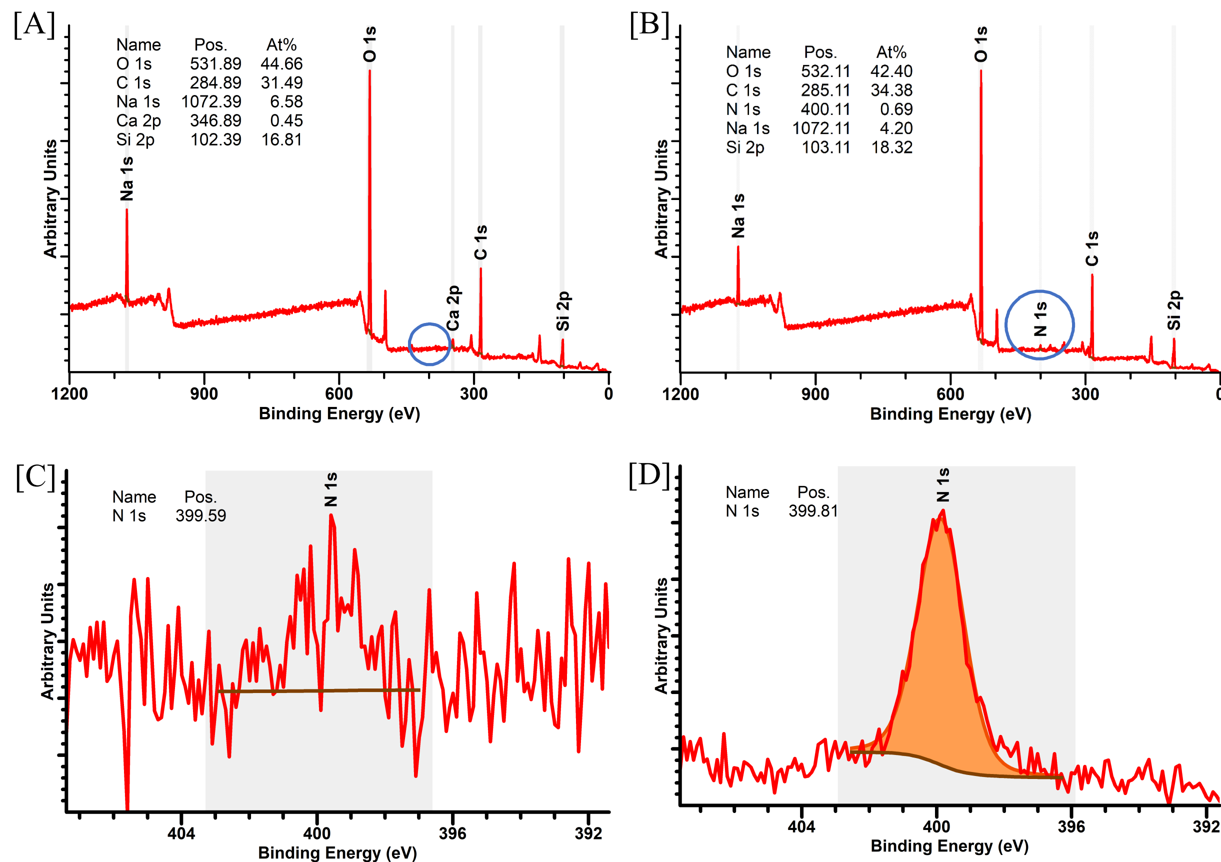


Figure 3.7: XPS results comparing soda-lime glass sample interfaces before and after the cleaning procedure. [A] Broad XPS scan of soda-lime glass surface before cleaning. Location of nitrogen binding energies is circled. [B] Broad XPS scan of soda-lime glass surface after cleaning. Location of nitrogen binding energies is circled. [C] High resolution XPS scan focused on nitrogen binding energies before cleaning. No clear nitrogen peak present. [D] High resolution XPS scan focused on nitrogen binding energies after cleaning. Clear nitrogen peak present. High resolution spectroscopy calibrated using C 1s to 284.8 eV reveals a clear nitrogen peak in the cleaned sample, and the absence of a peak before cleaning. Nitrogen peak is centered around 399.81 eV in the cleaned sample.

### 3.2.2 Scanning electron microscopy (SEM) and energy dispersive x-ray (EDX) analysis

SEM pictures of the bonded interface were taken for several materials, including soda-lime glass, coated fused silica, uncoated fused silica, and coated YAG. This was done in order to observe the interface directly for any notable features (ex. microgaps) that remain to be optimized, as well as characterize the quality of the bond. EDX analysis was done to confirm the composition of both the bulk material, as well as any coatings at the interface. SEM images and EDX results for soda-lime glass, coated fused silica, and uncoated fused silica are shown in fig. 3.8.

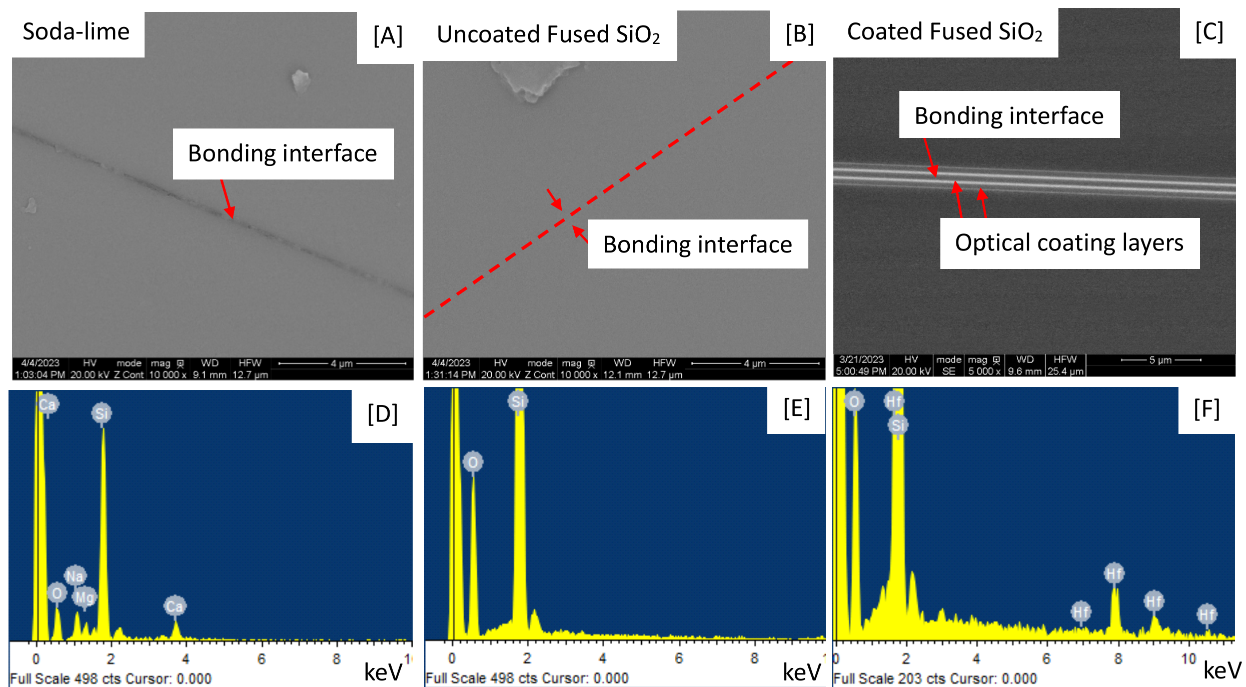


Figure 3.8: [A] SEM image of bonding interface for soda-lime glass sample. [B] SEM image of bonding interface for uncoated fused silica sample. [C] SEM image of bonding interface for coated fused silica sample. [D] EDX results for bonding interface of soda-lime glass sample. [E] EDX results for bonding interface of uncoated fused silica sample. [F] EDX results for bonding interface of coated fused silica sample.

As shown in fig. 3.8, only the SEMs of optical grade materials, uncoated and coated fused silica, reveal a lack of a visible bonding interface. The soda-lime glass, although polished using the same method as the other samples, shows a visible bonding interface, indicative of trapped water or contamination [50]. The most interesting image is of the coated fused silica sample (fig. 3.8c), as the optical coating layers can be clearly seen on either side of the bonding interface. The white lines represent the detected Hf in the sample, as heavier metals tend to show up brighter under SEM than lighter elements, such as Si [57]. This Hf is a part of the coating, as shown in the EDX results for the coated fused silica bonding interface (fig. 3.8f). The EDX results (fig. 3.8, d and e) correctly identify the elements expected for soda-lime glass (i.e. Na, Ca, Si, O) and uncoated fused silica (i.e. Si, O) bonding interfaces, respectively. Overall, the bonds for optical materials seem to be strong visually, but investigation into the bondability of a real active material, such as YAG, is ideal. This is discussed next.

There were some concerns regarding the bondability of the YAG samples. The samples did not bond well, presumably due to imperfections on the surface of the samples described previously in this chapter (fig. 3.3). However, the chemical composition needs to be investigated as well, since the bonding method was designed specifically for silica bonding. With the bulk material being YAG, there is a possibility of incompatibility with the bonding mechanism. Some SEM images of

these samples are shown in fig. 3.9. EDX analysis was also conducted in conjunction with these pictures.

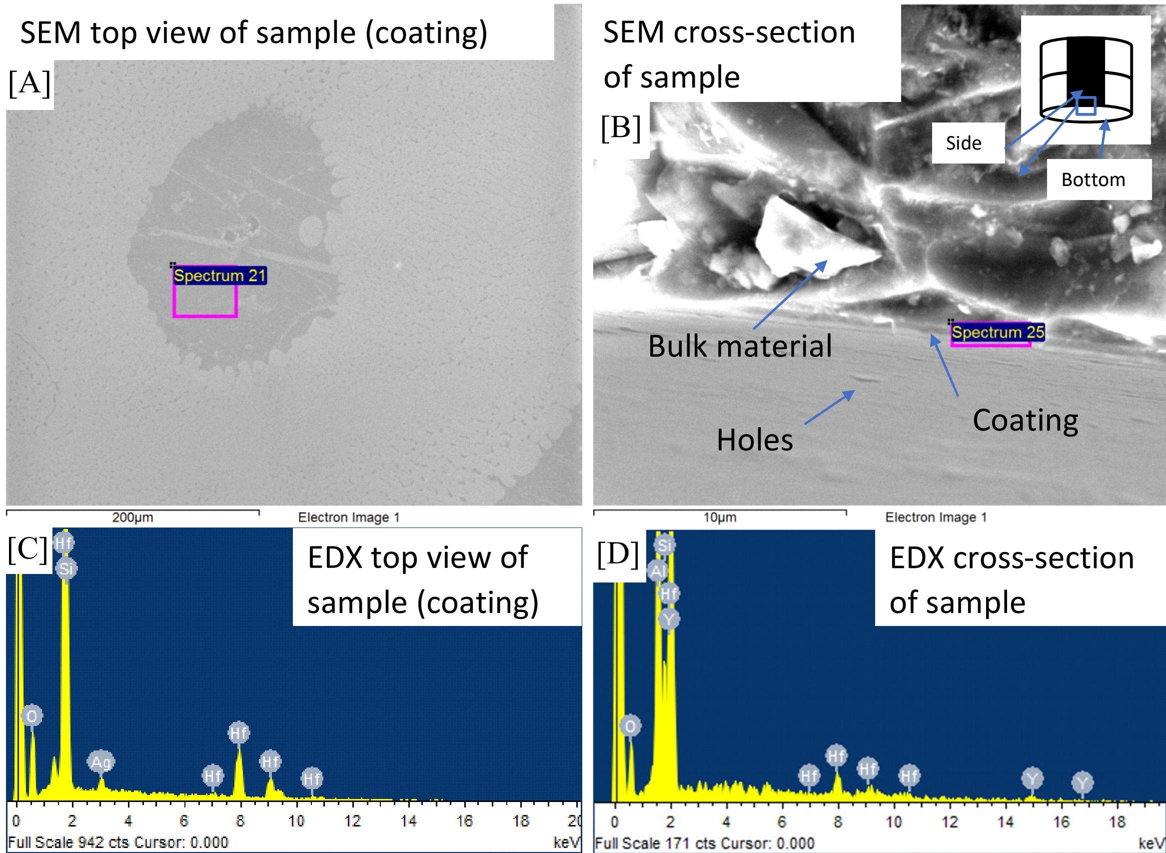


Figure 3.9: SEM and EDX results for coated YAG sample. [A] SEM image of top of sample, showing coating. [B] SEM image of cross-section of sample. Position of sample shown in top right. [C] EDX analysis of sample coating elemental composition. Area measured is shown with a pink rectangle. [D] EDX analysis of cross-sectional elemental composition. Area measured is shown with a pink rectangle.

From the images, the coatings, bulk material, and imperfections on the surface of the sample are all apparent (fig. 3.9b). Looking at the cross sectional EDX results (fig. 3.9d), the presence of Hf, Si, O, Y, and Al are clear. Y and Al are components of the bulk material, whereas Si, O, and Hf are a part of the coatings. The large presence of Si and O over the other elements at the interface supports the feasibility of the bonding mechanism. Successful bonding has also been achieved using smooth fused silica samples of similar geometry, providing additional evidence that the cause of the poor bonding was the imperfections at the surface of the samples.

## 3.3 Qualitative Shear Testing

### 3.3.1 Soda-lime glass

After proof of concept for the wet mounted bonding procedure was demonstrated, the next step was to conduct a few initial bonding tests to replicate the results. These initial qualitative results laid the foundation for future experiments and directions. An arbitrary classification scheme was created for the bonds observed. These initial bonds were created using soda-lime glass samples. “Strong” bonding is defined as bonding that shows a perfectly bonded area surrounded by Newton rings, unable to be broken by hand even with a considerable amount of force (about 30 N to 40 N) and/or when broken, leads to damage at the interface, indicating bulk material fracturing. “Weak” bonding is defined as bonding that shows a perfectly bonded area surrounded by Newton rings that is easily broken at the interface with little force and when broken, does not leave any visible damage at the interface. “No bond” is defined as the absence of a perfectly bonded area. Examples of “strong” bonds are given in fig. 3.10.

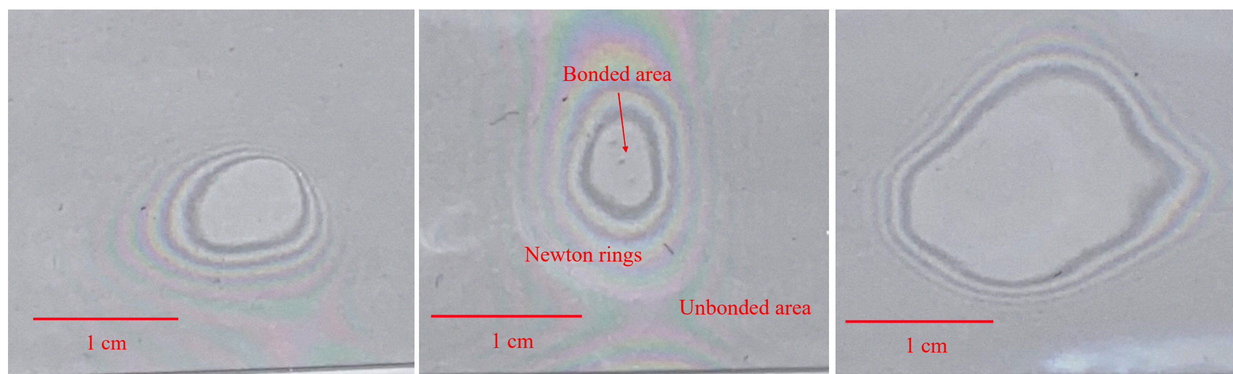


Figure 3.10: Images of 3 different soda-lime glass samples, showing bonded and unbonded areas of glass. Metric scales are given. Newton rings are apparent, as they separate the bonded areas from the unbonded areas.

From our qualitative results, it was found that high applied pressures and temperatures during bonding tended to yield the strongest bonds. Increased pressures and temperatures help to overcome common bonding inhibitors, such as particle contamination and low asperity contact, resulting in a higher proportion of covalent bonds being formed and an overall stronger interface adhesion [27]. Other results also helped to determine a pressure at which bonding occurs consistently (0.88 MPa), while avoiding sample cracking from too much pressure. However, these findings are not sufficent to formally characterize the strength of the bonds. Bonded area plays an important role in determining bond strength, as larger areas of remaining hydrogen bonds may resist an equivalent amount of shear as a smaller area of interfacial covalent bonds, even though covalent bonds are vastly stronger than hydrogen bonds individually. Therefore, destructive shear strength tests were conducted while controlling for bonded area.

### 3.3.2 Fused silica

A similar procedure was done with both coated and uncoated fused silica samples, which are materials that have a similar geometry to the material used in the microchip laser design. An example of a bonded sample is shown in fig. 3.11, a and b. Due to the thickness of the samples, there are no Newton rings present. However, imperfections in the bond can still be seen. After a new apparatus was adapted for higher throughput workflow, some contamination seemed to

appear. After additional testing, it seemed like this was due to the extended amount of time between washing the glass samples and mounting them in the bonding apparatus. This is supported by two pieces of evidence. In the previous iteration of the bonding apparatus, only one sample is bonded per apparatus, meaning that the time from washing to mounting is much lower than when five samples are bonded in parallel. Because of this, there is a lower chance of contamination. Additionally, when using the new apparatus, speeding up the process in a second trial resulted in only 1/5 samples showing some contamination, whereas most samples were contaminated in the first trial due to a lengthy wash to mounting time. Some examples of contamination can be found in fig. 3.11, c and d. Samples were tested manually to observe the strength of the bonds, using the same criteria as soda-lime glass. Overall, the additional contamination did not seem to affect the shear strength of the bonds, but may require further investigation, if needed.

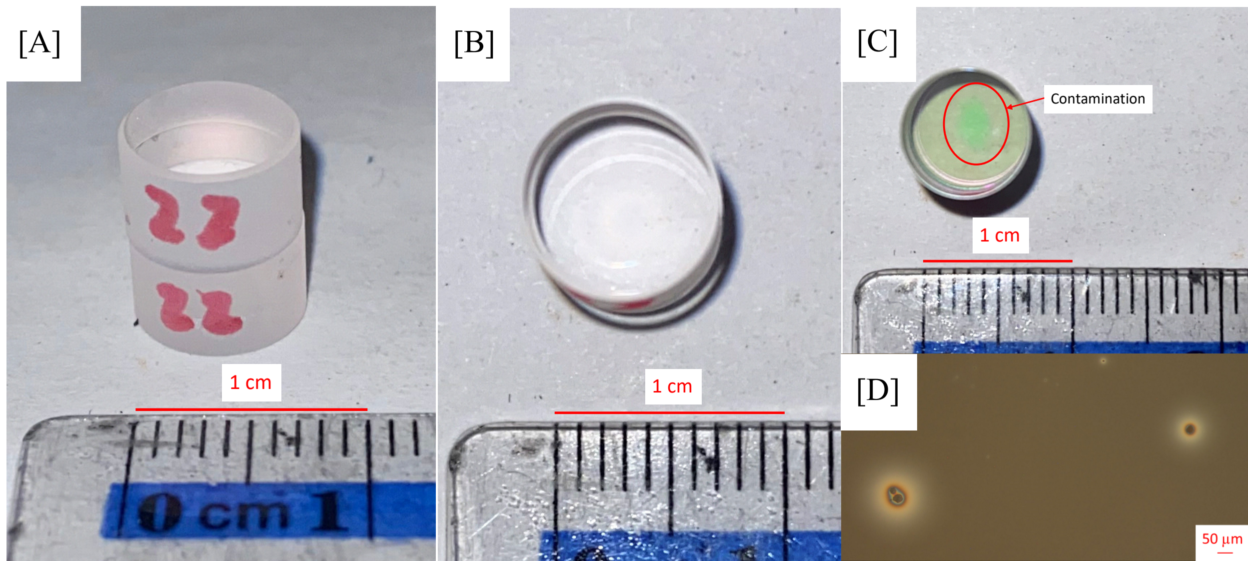


Figure 3.11: Several images showing bonded fused silica samples, highlighting some contamination that occurs at the interface. [A] Side view of uncoated fused silica bonded sample. [B] Top view of uncoated fused silica bonded sample. [C] Top view of contaminated, coated, fused silica sample. Highlighted discolouration indicates contamination. [D] Microscope image of contamination at the interface of a bonded, uncoated fused silica sample.

## 3.4 Quantitative Shear Testing

### 3.4.1 Soda-lime glass

An example of a shear reading is shown in fig. 3.12. The sample is compressed until fracturing at the interface, which is when the load drops significantly. Note that the shear curve has a deviation from the expected linear increase. This will be discussed in section 3.4.2.

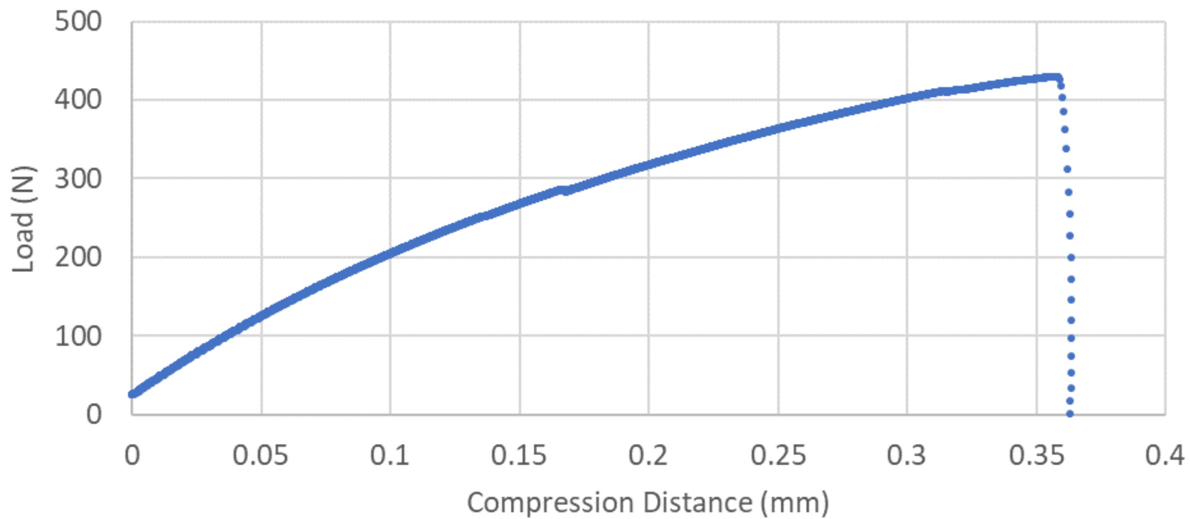


Figure 3.12: Graph showing load experienced by a bonded soda-lime glass sample relative to the distance compressed. There is deviation from a linear relationship between load and compression distance.

The compiled results for the destructive shear tests are shown in fig. 3.13. The hatched region in fig. 3.13 indicates the estimated shear strength region for our process as bonding temperature increases. Our results show shear strength values ranging from 3.9 MPa to 19.9 MPa for bonding temperatures of 160 °C to 300 °C, using a 30 min temperature treatment time. The strength of the bonds was found to increase with process temperature. This is likely due to the conversion of weaker hydrogen bonds to stronger covalent bonds reported to occur during temperature treatment [27]. The strength values are in the range of those found in previous research. One paper reported values between 3.45 MPa and 12.2 MPa using an annealing temperature of 400 °C and bonding time of 10 h [23]. Another paper reported strong bonding when samples were pre-bonded at room temperature for 24 h, then annealed at 150 °C for 12 h [8]. More recent studies show bond strengths in the range of 4.5–15 MPa for temperatures ranging from 24 °C to 560 °C, with pre-bonding and annealing steps requiring 4–24 h [9,10,20,24,25]. Our process generated bonds comparable to those obtained with recent SAB and other methods [9,10,20,24,25]. At the same time, our process has reduced complexity, a reduced 30 min heat treatment time, and is thus very suitable for mass production [41].

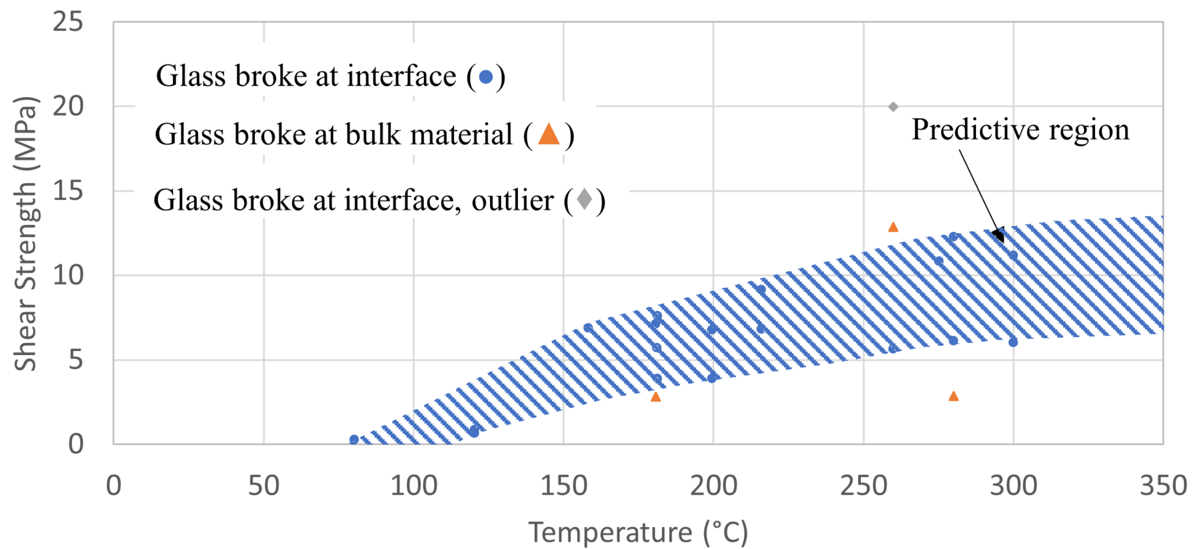


Figure 3.13: Shear strength of bonded soda-lime glass samples tested mechanically using a tensile tester (Instron 5548). This is compared to the temperature at which each sample was treated in a furnace (Binder oven) for 30 min. All samples were clamped with an approximate pressure of 0.88 MPa. Samples were in the furnace for 30 min, excluding a 7 min ramp/time before stabilization. The complete overlap bonding configuration was used for all tested samples. There seemed to be one outlier with a measured shear strength (19.9 MPa) much higher than the average. Temperature values of 280 °C and higher were measured using the Binder oven's internal temperature probe. Temperature values below 280 °C were measured using an external resistive temperature detector.

Bulk material breaks are also shown in fig. 3.13, which can occur when the bond is much stronger than the bulk glass or when there is residual heat stress within the material, causing the break to occur at a point away from the interface.

### 3.4.2 Fused silica

Similar to the soda-lime glass testing, the shear strength of coated and uncoated fused silica glass samples was also measured. Examples of both coated and uncoated sample shear strengths are shown in fig. 3.14.

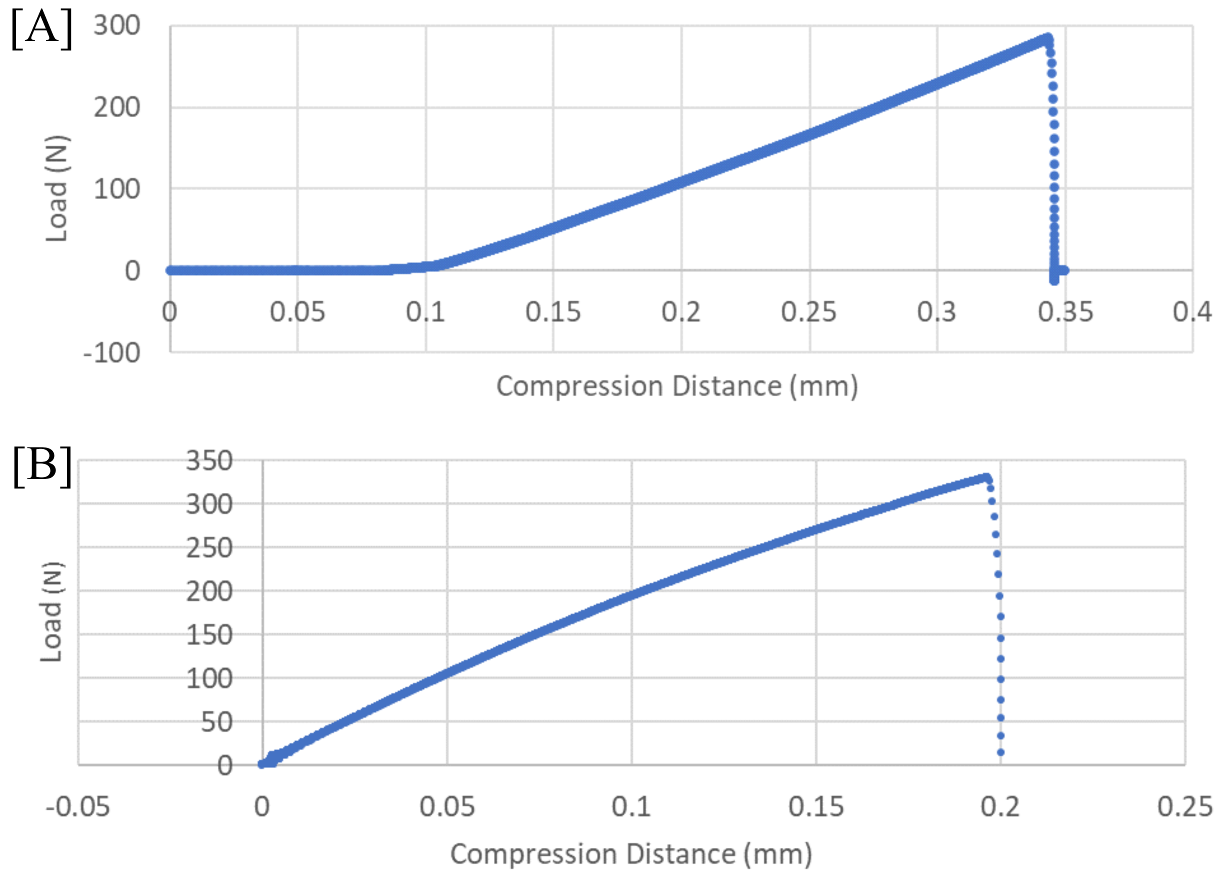


Figure 3.14: Graphs showing load experienced by bonded fused silica samples relative to the distance compressed. [A] Shear graph for uncoated fused silica sample. There is a small period of no load due to initial clamping position. [B] Shear graph for coated fused silica sample. Both sample loads increased relatively linearly and reached similar peak loads.

Comparing these shear results to the soda-lime glass results, the bonds of coated and uncoated fused silica had similar shear strengths to soda-lime glass bonds, which have been shown to be a strong bond, as discussed in section 3.2.1. Comparing the shape of the shear graphs for fused silica to soda-lime glass, the load on the fused silica samples increases more linearly relative to the soda-lime glass samples. This is consistent with the shape of the samples. With the soda-lime glass substrates being more thin and flat, they are more elastic. On the other hand, the fused silica samples are taller and thicker, resulting in less elasticity.

## 3.5 Chapter 3 Summary

Using optical interferometry, the surface roughnesses of the bonded interface for soda-lime glass, uncoated fused silica, and coated YAG were measured. Interferometry showed waviness artifacts, but still resolved micrographs of the bonded interface. To determine an accurate RMS surface roughness, AFM was used. The RMS values were within range for successful direct bonding, according to previous literature. Using XPS, SEM, and EDX, a bonding model proposed in previ-

ous literature was verified, while also allowing visual inspection of the bonded interface. Bond quality was then evaluated quantitatively using destructive shear testing, which revealed a similarly strong bond compared to previous literature, but created using a much more efficient process.

# Chapter 4: Design Considerations for the Microchip Laser

There are two other factors that may affect the performance of the bond within the microchip laser design. These are optical robustness and ability to survive processing. Optical robustness is important because this bond must not interfere with the laser beam. A poor bond is at risk of absorbing or reflecting the laser light within the active material, reducing the efficacy of the laser. The active material must also be cut down to a much smaller size after bonding as part of the design and to accomodate mass production. This means that a dicing workflow should be tested to investigate any mechanical problems that may occur.

## 4.1 Laser Damage Results

### 4.1.1 Continuous wave (CW) laser damage results

Since this bonding process will be used in the design of microchip lasers, bonds should not impede the transmittance of the laser through the material. First, I conducted an exploratory study of bond robustness under intense laser irradiation using a powerful CW fiber laser. An example of the laser induced damage is shown in fig. 4.1, where the laser was directed onto a previously bonded region of soda-lime glass. When a sample bonded at 160 °C was irradiated with a laser at 75 % power (≈375 W) for 2 s, the interface did not show any fracturing or delamination [41]. Only when the power was increased to 425 W or the dwell time was increased to 4 s did damage occur, indicated by a loss of bonded area as shown by a shift in the Newton rings. The damage is highlighted in the magnified picture of fig. 4.1. The magnified picture reveals melting of the surface material indicated by the presence of bubbles. Since no interfacial damage was observed without the presence of melting, the robustness of the bonds under CW laser irradiation is at least as high as that of the soda-lime glass bulk material [41].

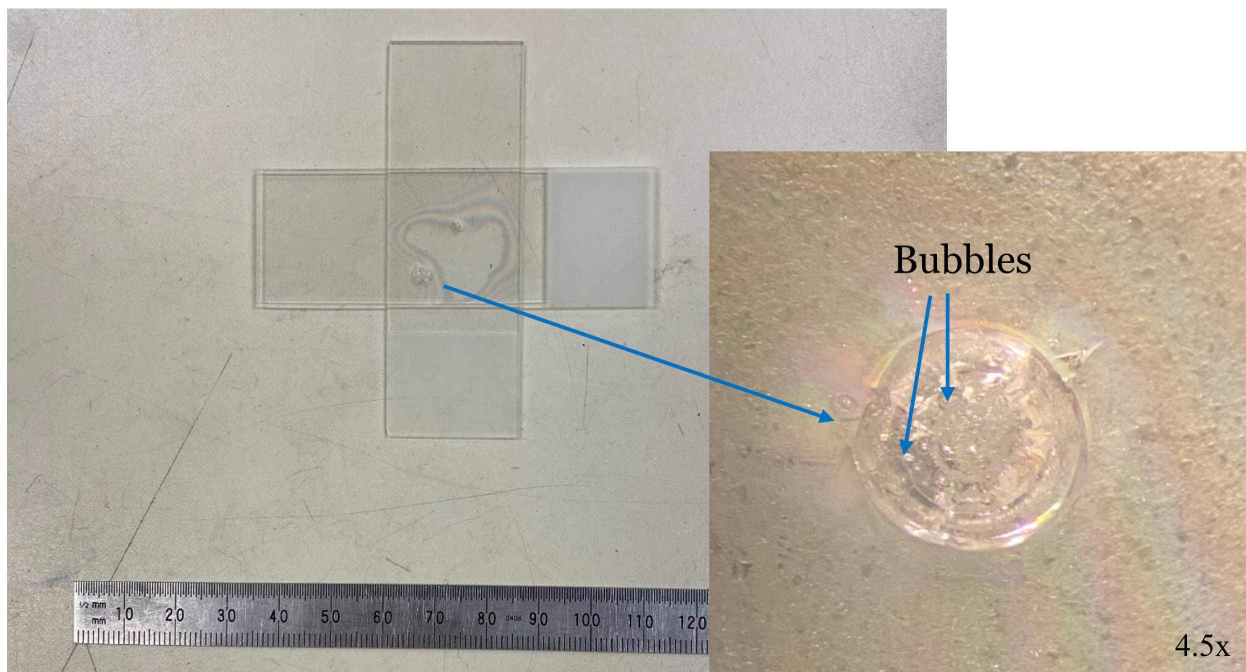

Figure 4.1: Directly bonded soda-lime glass sample annealed at 160 °C. Bond delamination is observed at the location where the laser irradiated the sample, indicated by the bending of Newton rings around the damage site. A magnification of the sample shows melting after exposure to a 375 W CW laser for 4 s.

### 4.1.2 Soda-lime femtosecond (FS) laser damage results

Because the bonds will be used in ultrafast pulsed laser design, testing the bonds using a short pulse length laser is essential. The mechanism of action for ultrafast pulsed lasers (described in section 1.4.2) is very different from a CW laser, which provides another perspective on the optical robustness of the bonds. This was first tested using soda-lime glass. 3 types of samples were irradiated with the FS laser, a poor bonding condition, bulk control condition, and bonding condition. The bonding condition involved the irradiation of a sample that was successfully bonded using our method. The bulk condition involved the irradiation of a bulk sample of soda-lime glass. The poor bonding condition was a sample that was intended to simulate a poor bond, by irradiating a sample of two soda-lime glass slides taped to one another. Pictures of the 3 conditions are shown in fig. 4.2.

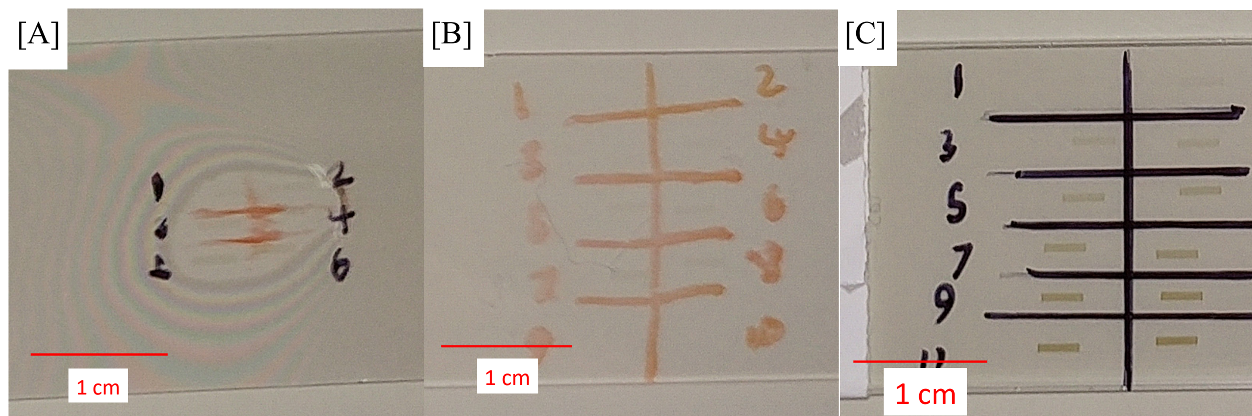


Figure 4.2: Images of samples used in soda-lime FS laser induced damage threshold (LIDT) experiment. [A] Irradiated sample of soda-lime glass bonded using modified RCA-1 procedure. [B] Irradiated bulk material sample of soda-lime glass. [C] Irradiated sample of two taped soda-lime glass substrates to simulate a poor bond.

After characterizing the damage using colour intensity, the results were compiled and are shown in fig. 4.3.

Comparing the laser induced damage threshold (LIDT) of the different samples, some observations are clear. The poor bonding condition had the lowest LIDT at about 15.27 J/cm$^2$. The damage also increased at the highest rate, and reached the highest amount of damage out of all three conditions. On the other hand, both the bonding condition and the bulk material condition had similar rates of damage increase and peak laser damage. The LIDTs for these conditions are about 35.65 J/cm$^2$ and 20.37 J/cm$^2$, respectively. This suggests that the optical robustness of the bonded

samples are as strong, if not stronger, than the bulk material when irradiated with a powerful FS laser.

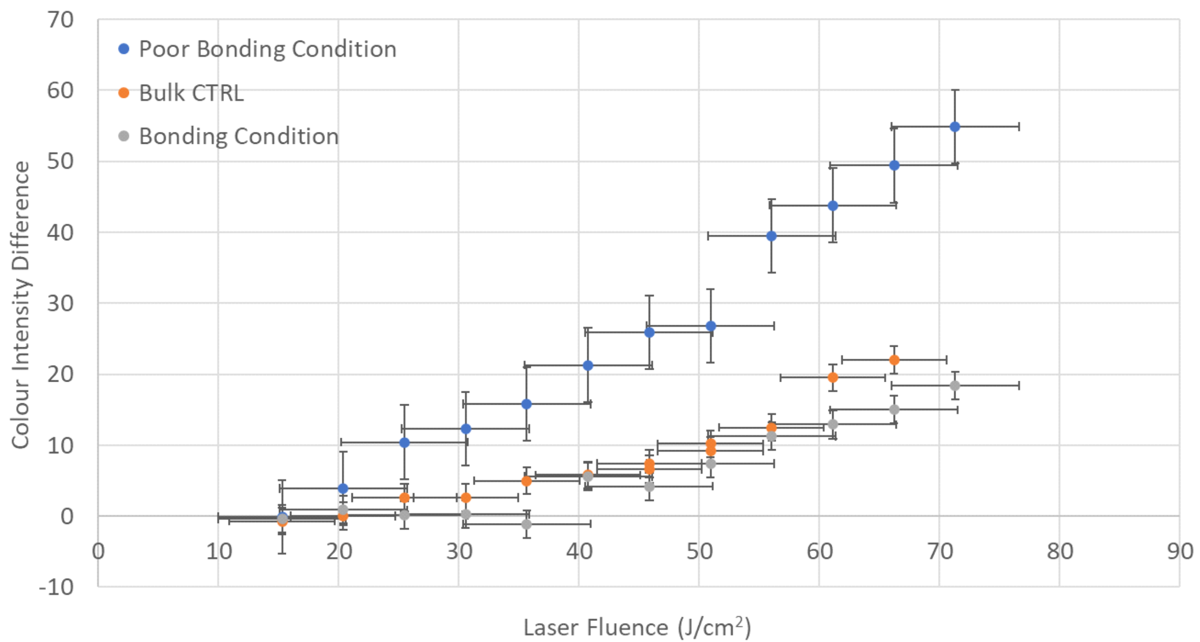


Figure 4.3: LIDT analysis results for three conditions of soda-lime glass samples to test optical robustness of bonds. The poor bonding condition has the highest rate of laser damage increase as well as the highest peak for laser damage. The bonding condition and the bulk material condition both had similar reactions to the laser.

### 4.1.3 Fused silica FS laser damage results

Next, uncoated fused silica samples were tested using the same methodology, as pure fused silica is more representative of the optical material that will be used in the final microchip laser design. The bulk condition was omitted from these experiments, as the geometry was too different from the poor bonding and bonding conditions. In this test, instead of the laser focal point moving perpendicular to the beam (like in the soda-lime glass experiements), the laser focal point was moved parallel to the beam. This is because consistent bulk material damage was difficult to produce within such thick material, according to preliminary tests. The results are shown in fig. 4.4 below.

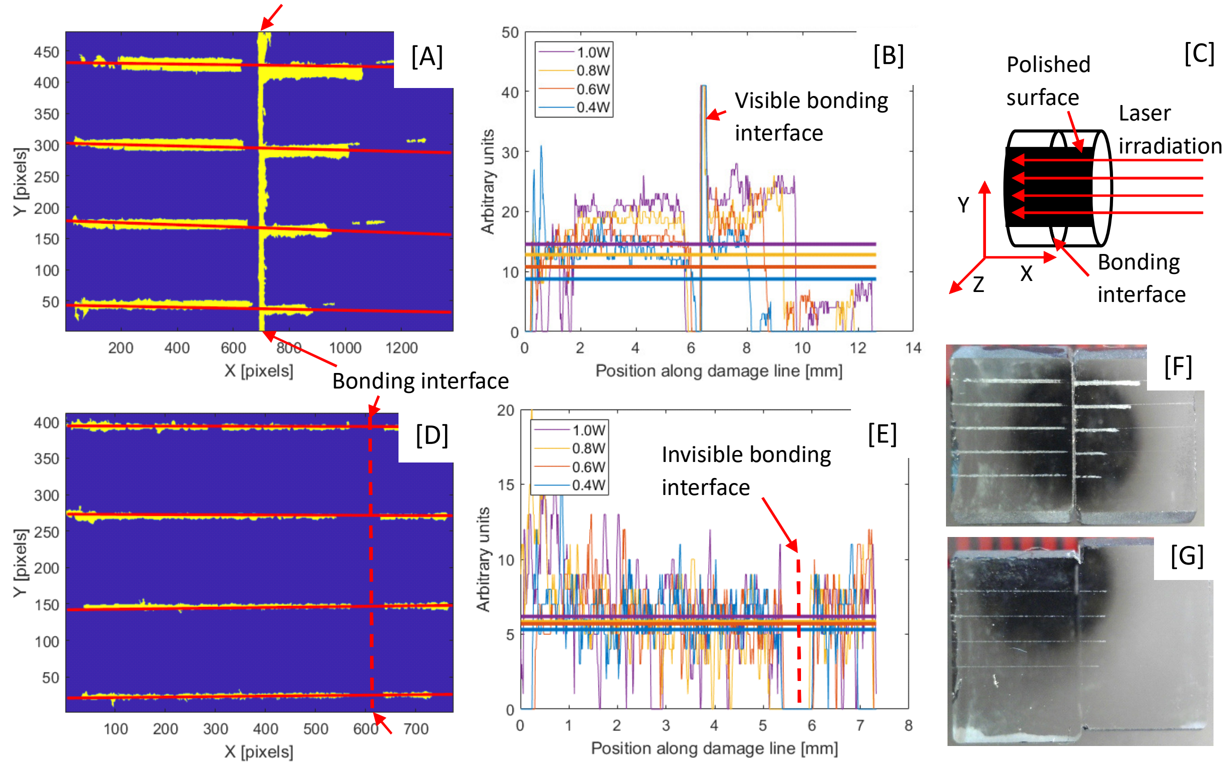


Figure 4.4: Results for FS induced laser damage in uncoated fused silica samples. [A] Micrograph of cross-section of poor bonding condition fused silica sample, processed to highlight damage caused by the FS laser within the sample. [B] Damage width versus position along damage line measured along red lines in poor bonding condition micrograph, with position pixel measurements converted to metric units using a known approximate scale. Average damage width for each power is shown by the thicker horizontal plotted lines. [C] Diagram of sample irradiation geometry. Laser focus begins to the left of the bonding interface, and is moved to the right. [D] Micrograph of cross-section of bonding condition fused silica sample, processed to highlight damage caused by the FS laser within the sample. [E] Damage width versus position along damage line measured along red lines in bonding condition micrograph, with position pixel measurements converted to metric units using a known approximate scale. Average damage width for each power is shown by the thicker horizontal plotted lines. [F] Original image of poor bonding condition sample used for analysis, before image processing. The samples were irradiated from the right, then cross-sectioned and polished for viewing. [G] Original image of bonding condition sample used for analysis, before image processing. The samples were irradiated from the right, then cross-sectioned and polished for viewing.

In fig. 4.4, a and d, the laser fluences that caused each of the damage lines (from top to bottom) are 5092.96 J/cm$^2$, 4074.37 J/cm$^2$, 3055.77 J/cm$^2$, and 2037.18 J/cm$^2$. From the graphs, it is clear that damage doesn't seem to change very much with laser fluence in the bonding condition, whereas it does in the poor bonding condition. Most importantly, while a visible bonding interface and damage can be seen in the poor bonding condition, no visible interface and little damage can be seen in the bonding condition. This suggests that the behaviour of the directly bonded sample

when irradiated with an FS laser is more similar to a cohesive bulk material than two independent surfaces, as damage is not exasperated by gaps and contaminants at the interface [37]. The bonds seem to be optically strong enough to handle powerful FS laser irradiation.

## 4.2 Developing a Dicing Workflow

As part of the microchip laser design, the designed bond needs to be able to survive a dicing workflow. This was tested using uncoated, fused silica samples, where an 8 mm diameter, 10 mm thick, cylindrical sample was cut and polished down to form 2 mm × 2 mm × 2 mm bonded cubes. A picture of an initial sample is given in fig. 4.5.

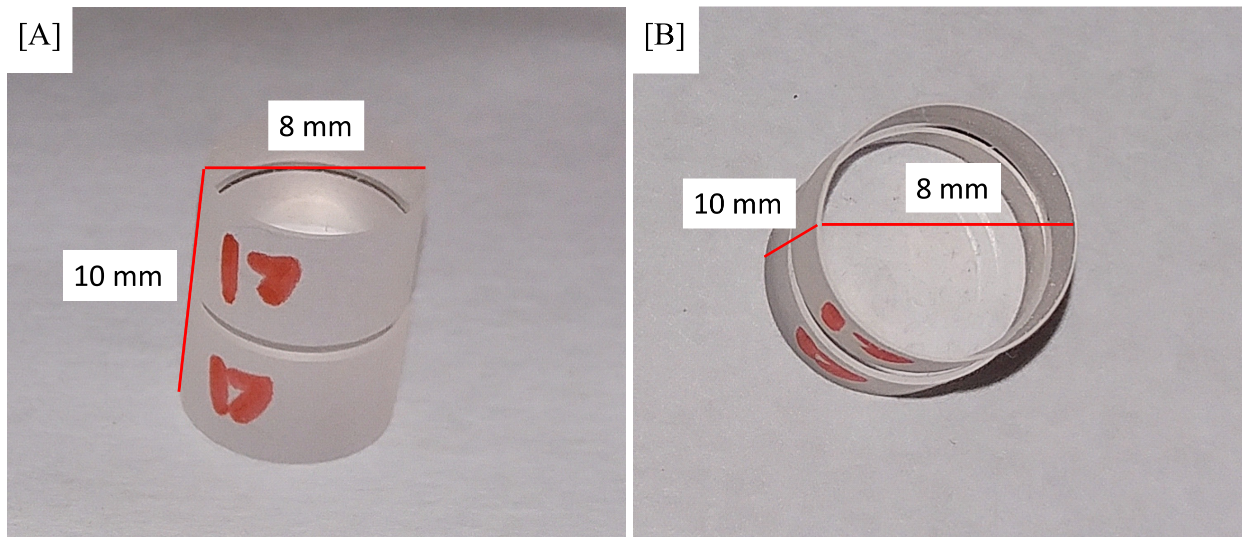


Figure 4.5: Images of bonded, uncoated, fused silica samples before dicing workflow. [A] Side view of sample, including dimensions. [B] Top view of sample, including dimensions.

### 4.2.1 Preparing samples for dicing

Dicing was only able to be done on thin samples. Because our initial samples were so thick, the first problem that needed to be addressed was thinning the samples. This was done using a low speed saw. A picture of this saw can be seen in fig. 4.6a. The saw was used over other options because its low speed offered greater control over the cuts. After cutting, the sample surfaces needed to be polished to allow the laser to pass through the material without unintended impedence. A picture of the polisher used is shown in fig. 4.6b. The much thinner sample is shown in fig. 4.7.

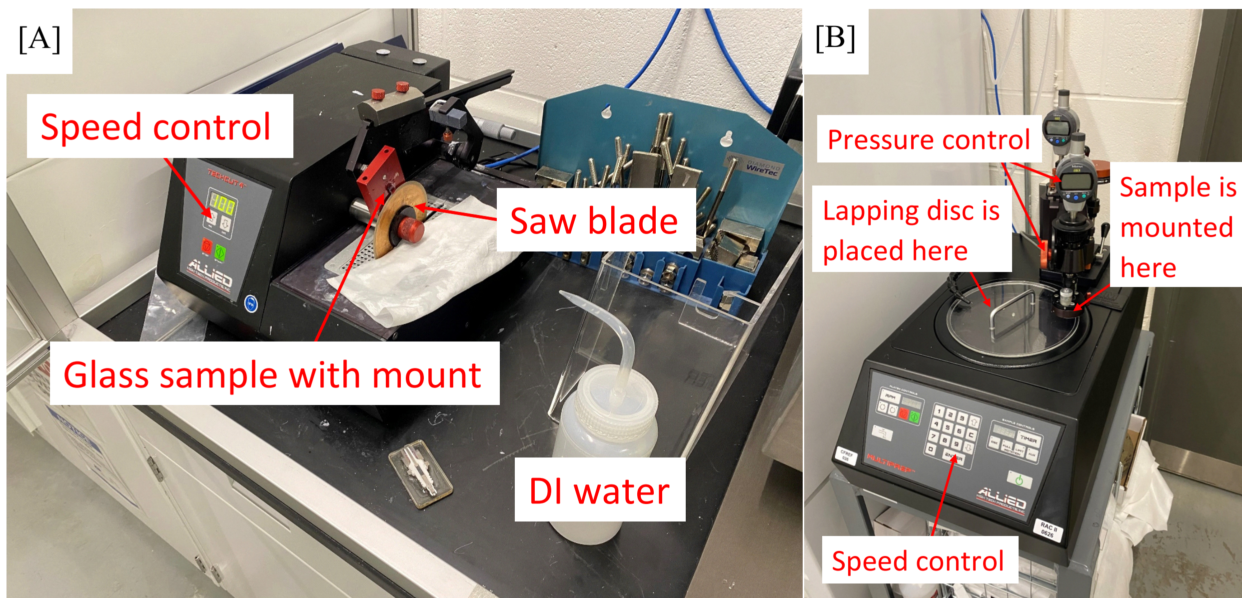


Figure 4.6: Pictures of devices used for thinning fused silica samples. [A] Low speed saw used for coarse sectioning of samples. [B] Polishing device used for cleaning up the surfaces after cutting.

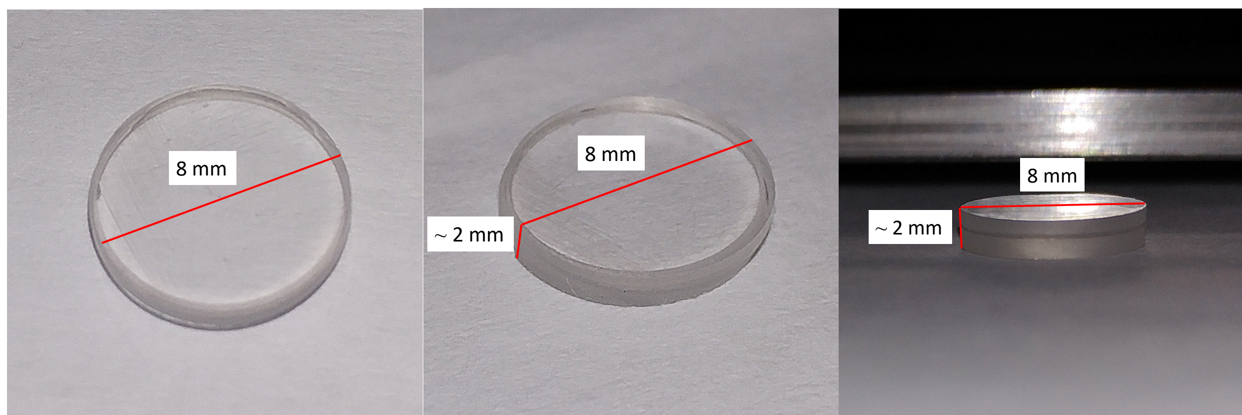


Figure 4.7: Pictures of thinned fused silica samples after cutting and polishing.

### 4.2.2 Dicing the samples

After the samples were thinned, the samples were diced using a DISCO DAD3240 dicing saw. With previous attempts, the samples were mounted directly on the dicing tape. However, this method proved to be too flimsy as the blade rotates at 18,000 RPM, causing the cuts to be incomplete and damage the edges. To rectify this, the samples were mounted on a rigid carrier glass substrate using dicing adhesive (fig. 4.8a). The samples were then able to be diced successfully (fig. 4.8b). The bonded interface for a single bonded cube is shown in fig. 4.8c. Note the sharp cut edges and lack of observable interface. This provides evidence that the bond is strong enough to stay intact during a dicing workflow to form cubes as small as 2 $mm^3$.

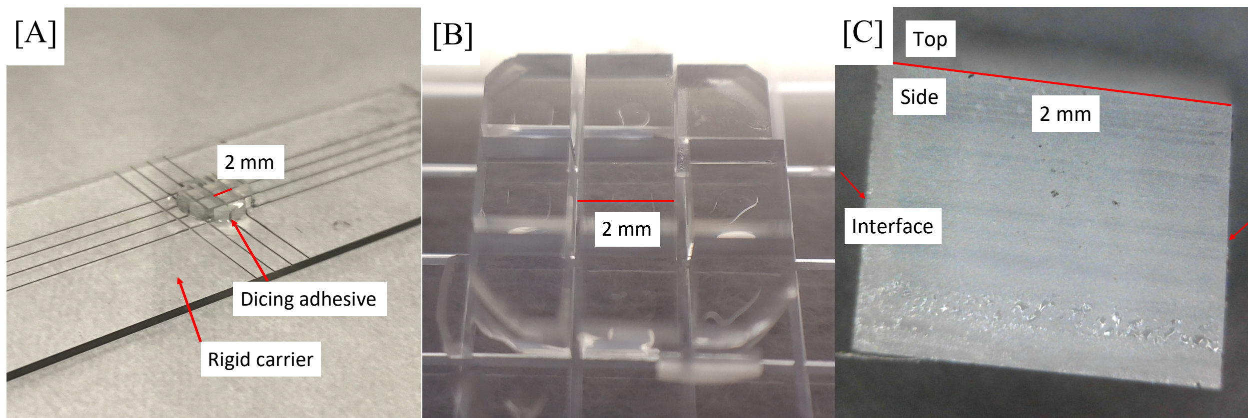


Figure 4.8: Processing of thinned fused silica samples into 2 $mm^3$ samples. [A] Thinned fused silica sample after dicing, bonded using dicing adhesive to rigid carrier. [B] Thinned fused silica sample after dicing. [C] Side view of single diced fused silica 2 $mm^3$ cube. Bonding interface is not visible, and cut edges are sharp.

## 4.3 Chapter 4 Summary

In order to evaluate the optical quality of the bonds produced using the modified RCA-1 method, CW and ultrafast laser irradiation were used to produce damage within soda-lime glass and uncoated fused silica bonded samples. CW irradiation resulted in unified melting of the interface and bulk material, suggesting a strong optical bond. This was confirmed using ultrafast laser irradiation, which caused significantly less damage in well bonded samples as opposed to poorly bonded samples. The development of a dicing method for mass production of bonds was also described.

# Chapter 5: Conclusions and Future Directions

In order to design cheap, ultrafast, microchip lasers, a simple, low temperature, glass-to-glass bonding process was successfully developed. This was shown through evaluation of bond shear strength, optical robustness, surface roughness, and interface chemical analysis. Four different substrates were used in the testing, starting with cheap soda-lime glass, then fused silica, then optically coated fused silica, and finally optically coated YAG, which is a good approximation for the proposed final material. Through compression testing, the process generated bond shear strengths similar to recent methods found in literature, but was faster and was perceived to be easier to operate. Fracturing of the samples during testing accentuated these conclusions as it demonstrated the mechanical failure of the bulk material in tandem with the bonded interface, suggesting that the produced bonds are as strong, if not stronger, than the bulk material.

The bonds were also successfully irradiated using both a CW fiber laser and an ultrafast, pulsed FS laser to test optical robustness. The results highlight a bond with laser damage evolution closer to the behaviour of bulk material rather than a surface, which traditionally has a lower LIDT due to contamination. This suggests that the bonding interface was optically strong and relatively contamination-free.

Surface roughness measurements were collected using optical interferometry and AFM, in order to ensure that the surface profiles observed were accurate. This is important, as optical measurement methods are not always effective when working with transparent materials. Regardless, the surface roughness results were small enough for bonding and similar to ranges found in literature.

To support our chemical bonding model, XPS was used to collect data on the elements and molecules present at the bonding interface, before and after cleaning. Evidence of silica bonds and nitrogen incorporation into the glass interface as a result of the cleaning process supports the proposed bonding model and suggests a possible advantage for using our method over traditional RCA-1 cleaning, as the ammonium bath at the end of the process may facilitate greater opportunity for direct bonding.

SEM pictures of the contacting substrates revealed a high quality bonding interface in optical grade materials. Additionally, a cutting process was successfully developed to show that the bonds are able to survive the reduction in size necessary for incorporation into the microchip lasers as a mass producible technology.

Bond time and applied pressure during temperature treatment are other factors that remain to be optimized to further improve bonding, if needed. As a next step, parameter studies with the actual material and coatings to be used in the microchip laser are necessary to show similar behaviour to already tested materials such as fused silica. A method to determine the proportion of microgaps within a sample would be useful as another tool to characterize bond quality.

# References

[1] J. Haisma and G.A.C.M. Spierings, "Contact bonding, including direct-bonding in a historical and recent context of materials science and technology, physics and chemistry: Historical review in a broader scope and comparative outlook," Mater. Sci. Eng. R Rep., vol. 37, no. 1-2, Jan. 2002, pp. 1-60. https://doi.org/10.1016/S0927-796X(02)00003-7.

[2] W. Zhang and N. Bay, "A Numerical Model for Cold Welding of Metals," CIRP Ann. - Manuf. Technol., vol. 45, no. 1, 1996, pp. 215-220. https://doi.org/10.1016/S0007-8506(07)63050-9.

[3] A. Sayah, D. Solignac, T. Cueni and M.A.M. Gijs, "Development of novel low temperature bonding technologies for microchip chemical analysis applications," Sens. Actuator A Phys., vol. 84, no. 1-2, Aug. 1999, pp. 103-108. https://doi.org/10.1016/S0924-4247(99)00346-5.

[4] R. Sabia, "Direct bonding of articles containing silicon,", vol. 10/255,926, no. US6949164B2, Sept. 2005.

[5] P. Birckigt, K. Grabowski, G. Leibeling, T. Flügel-Paul, M. Heusinger, H. Ouslimani and S. Risse, "Effects of static load and residual stress on fused silica direct bonding interface properties," Appl. Phys. A, vol. 127, Nov. 2021, pp. 938. https://doi.org/10.1007/s00339-021-05076-6.

[6] Q.Y. Tong, T.H. Lee and U. Gösele, "The Role of Surface Chemistry in Bonding of Standard Silicon Wafers," J. Electrochem. Soc., vol. 144, no. 1, Jan. 1997, pp. 384-389. https://doi.org/10.1149/1.1837415.

[7] D.J. Harrison, K. Fluri, K. Seiler, Z. Fan, C.S. Effenhauser and A. Manz, "Micromachining a Miniaturized Capillary Electrophoresis-Based Chemical Analysis System on a Chip," Science, vol. 261, no. 5123, Aug. 1993, pp. 895-897. https://doi.org/10.1126/science.261.5123.895.

[8] J. Xu, C. Wang, S. Zhou, R. Zhang and Y. Tian, "Low-temperature direct bonding of Si and quartz glass using the APTES modification," Ceram. Int., vol. 45, no. 13, Sept. 2019, pp. 16670-16675. https://doi.org/10.1016/j.ceramint.2019.05.098.

[9] C. Mai, M. Li and S. Yang, "Low temperature direct bonding of silica glass via wet chemical surface activation," RSC Adv., vol. 5, no. 53, May 2015, pp. 42721-42727. https://doi.org/10.1039/C5RA06705G.

[10] J. Xu, C. Wang, T. Wang, Y. Wang, Q. Kang, Y. Liu and Y. Tian, "Mechanisms for low-temperature direct bonding of Si/Si and quartz/quartz via VUV/O3 activation," RSC Adv., vol. 8, no. 21, Mar. 2018, pp. 11528-11535. https://doi.org/10.1039/C7RA13095C.

[11] J. Wei, S.M.L. Nai, C.K.S. Wong, Z. Sun and L.C. Lee, "Low temperature glass-to-glass wafer bonding," IEEE Trans. Adv. Packag., vol. 26, no. 3, Aug. 2003, pp. 289-294. https://doi.org/10.1109/TADVP.2003.818054.

[12] D. Kopf, "Ultrashort pulse microchip laser, semiconductor laser, laser system, and pump method for thin laser media,", vol. EP11720794.4A, no. EP2577818A1, Apr. 2013.

[13] D. Kopf, "Microchip laser,", vol. EP15737952.0A, no. EP3167516B1, Feb. 2020.

[14] K. Shoda, M. Tanaka, K. Mino and Y. Kazoe, "A Simple Low-Temperature Glass Bonding Process with Surface Activation by Oxygen Plasma for Micro/Nanofluidic Devices," Micromachines, vol. 11, no. 9, Aug. 2020, pp. 804. https://doi.org/10.3390/mi11090804.

[15] K.L. Wlodarczyk, D.P. Hand and M.M. Maroto-Valer, "Maskless, rapid manufacturing of glass microfluidic devices using a picosecond pulsed laser," Sci. Rep., vol. 9, Dec. 2019, pp. 20215. https://doi.org/10.1038/s41598-019-56711-5.

[16] A.K. Dwivedi, "Newton's rings,", pp. 1-8.

[17] Britannica, The Editors of Encyclopaedia., "Newton's rings," Encyclopedia Britannica, vol. 2023, no. 01/18, Jun. 2022. https://www.britannica.com/science/Newtons-rings.

[18] W.P. Maszara, G. Goetz, A. Caviglia and J.B. McKitterick, "Bonding of silicon wafers for silicon-on-insulator," J. Appl. Phys., vol. 64, no. 10, Jul 1988, pp. 4943-4950. https://doi.org/10.1063/1.342443.

[19] F. Mu, K. Iguchi, H. Nakazawa, Y. Takahashi, M. Fugino, R. He and T. Suga, "A comparison study: Direct wafer bonding of SiC–SiC by standard surface-activated bonding and modified surface-activated bonding with Si-containing Ar ion beam," Appl. Phys. Express, vol. 9, no. 8, Jul. 2016, pp. 081302. https://doi.org/10.7567/APEX.9.081302.

[20] C. Wang, J. Xu, S. Guo, Q. Kang, Y. Wang, Y. Wang and Y. Tian, "A facile method for direct bonding of single-crystalline SiC to Si, SiO2, and glass using VUV irradiation," Appl. Surf. Sci., vol. 471, Mar. 2019, pp. 196-204. https://doi.org/10.1016/j.apsusc.2018.11.239.

[21] A. Berthold, B. Jakoby and M.J. Vellekoop, "Wafer-to-wafer fusion bonding of oxidized silicon to silicon at low temperatures," Sens. Actuator A Phys., vol. 68, no. 1-3, Jun. 1998, pp. 410-413. https://doi.org/10.1016/S0924-4247(98)00028-4.

[22] J. Kiihamäki, H. Kattelus, M. Blomberg, R. Puurunen, M. Laamanen, P. Pekko, J. Saarilahti, H. Ritala and A. Rissanen, "Low-Temperature Processes for MEMS Device Fabrication," Advanced Materials and Technologies for Micro/Nano-Devices, Sensors and Actuators, Jan. 2010, pp. 167-178. https://doi.org/10.1007/978-90-481-3807-4_13.

[23] T. Mayer, A.N. Marianov and D.W. Inglis, "Comparing fusion bonding methods for glass substrates," Mater. Res. Express, vol. 5, no. 8, Jul 2018, pp. 085201. https://doi.org/10.1088/2053-1591/aad166.

[24] Q. Chen, Q. Chen and M. Ferraris, "Optimization of thermal assisted direct bonding of soda-lime glasses for lab-on chip application," Microsyst. Technol., vol. 16, no. 4, Apr. 2010, pp. 527-532. https://doi.org/10.1007/s00542-010-1025-9.

[25] M.M.R. Howlader, S. Suehara and T. Suga, "Room temperature wafer level glass/glass bonding," Sens. Actuator A Phys., vol. 127, no. 1, Feb. 2006, pp. 31-36. https://doi.org/10.1016/j.sna.2005.11.003.

[26] A. Giese, M. Körber, K. Kostourou, D. Kopf, M. Kottcke, J. Lohbreier, J. M. Schmidbauer, and B. Braun, "Passively Q-switched sub-100 ps Yb3+:YAG/Cr4+:YAG microchip laser: experimental results and numerical analysis," Proc. SPIE, vol. 12399, Mar. 2023, pp. 123990S. https://doi.org/10.1117/12.2649057.

[27] A. Plößl and G. Kräuter, "Wafer direct bonding: tailoring adhesion between brittle materials," Mater. Sci. Eng. R Rep., vol. 25, no. 1-2, Mar. 1999, pp. 1-88. https://doi.org/10.1016/S0927-796X(98)00017-5.

[28] C. Gui, M. Elwenspoek, N. Tas and J.G.E. Gardeniers, "The effect of surface roughness on direct wafer bonding," J. Appl. Phys., vol. 85, no. 10, Feb. 1999, pp. 7448-7454. https://doi.org/10.1063/1.369377.

[29] Y.N. Zhou, '"Microjoining and nanojoining,", ed. 1, 2008.

[30] R. Günther, W.R. Caseri and C. Brändli, "Direct bonding and de-bonding on demand of polystyrene and polyamide surfaces, treated with oxygen plasma," J. Appl. Polym. Sci., vol. 139, no. 10, Oct. 2021, pp. e51753. https://doi.org/10.1002/app.51753.

[31] Coherent Inc., '"Lasers: Understanding the Basics,", vol. 2023, no. 01/18. https://www.photonics.com/Articles/Lasers_Understanding_the_Basics/a25161.

[32] T. Apostolova and B. Obreshkov, '"Femtosecond optical breakdown in silicon," Appl. Surf. Sci., vol. 572, no. 151354, Jan. 2022. https://doi.org/10.1016/j.apsusc.2021.151354.

[33] P. Sharma and K. Vatsa, "Chapter 16 - Nanoclusters Under Extreme Ionization Conditions," Materials Under Extreme Conditions, no. 1, Jan 2017, pp. 575-613. https://doi.org/10.1016/B978-0-12-801300-7.00016-4.

[34] D. Du, X. Liu, G. Korn, J. Squier and G. Mourou, "Laser-induced breakdown by impact ionization in SiO2 with pulse widths from 7 ns to 150 fs," Appl. Phys. Lett., vol. 64, no. 23, Mar. 1994, pp. 3071-3073. https://doi.org/10.1063/1.111350.

[35] H. Hu, X. Wang and H. Zhai, "High-fluence femtosecond laser ablation of silica glass: effects of laser-induced pressure," J. Phys. D: Appl. Phys., vol. 44, Mar. 2011, pp. 135202. https://doi.org/10.1088/0022-3727/44/13/135202.

[36] J. Bonse, S.V. Kirner and J. Krüger, "Laser-Induced Periodic Surface Structures (LIPSS)," Handbook of Laser Micro- and Nano-Engineering, Nov. 2021, pp. 879-936. https://doi.org/10.1007/978-3-030-63647-0_17.

[37] G.G.E. Reaidy and L. Gallais, "Analysis of laser-induced contamination at 515 nm in the sub-ps/MHz regime," Opt. Eng., vol. 60, no. 3, Nov. 2020, pp. 031004. https://doi.org/10.1117/1.OE.60.3.031004.

[38] International Organization for Standardization, "Lasers and laser-related equipment -- Test methods for laser-induced damage threshold -- Part 1: Definitions and general principles (ISO 21254-1:2011),", vol. 2023, no. 01/20, Jul. 2011, pp. 16. https://www.iso.org/standard/43001.html.

[39] E. Assuncao and S. Williams, '"Comparison of continuous wave and pulsed wave laser welding effects," Opt Lasers Eng, vol. 51, no. 6, Jun. 2013, pp. 674-680. https://doi.org/10.1016/j.optlaseng.2013.01.007.

[40] M. Bachman, "RCA-1 Silicon Wafer Cleaning,", vol. 2021, no. 10/29, Sept. 1999, pp. 3. https://phas.ubc.ca/~ampel/nanofab/sop/rca-clean-1.pdf.

[41] J. Zhou, N. Mei, Z. Leonenko, N. Zhou and M. Mayer, "Direct glass-to-glass bonding obtained via simplified ammonia-based low-temperature procedure resists high shear stress and powerful CW fiber laser irradiation," RSC Adv., vol. 48, Oct. 2022, pp. 31016-31023. https://doi.org/10.1039/D2RA04234G.

[42] Thermo Fisher Scientific, "Thermo Scientific Microscope slides,", vol. 2021, no. 10/29, 2015, pp. 2. https://assets.thermofisher.com/TFSAssets/APD/brochures/objekttraeger_uk_0715_0209.pdf.

[43] VWR, "VWR® Plain and Frosted Micro Slides, Premium,", vol. 2021, no. 10/19, 2021, pp. 1. https://ca.vwr.com/store/product/en/4646174/vwrvistavisiontm-microscope-slides-plain-and-frosted-premium.

[44] D. Rugar and P. Hansma, "Atomic force microscopy," Phys. Today, vol. 43, no. 10, Oct. 1990, pp. 23-30. https://doi.org/10.1063/1.881238.

[45] M.G. Mostofa, C.I. Park and S.S. Park, "AFM probe based nano mechanical scribing of soda-lime glass," J. Manuf. Process., vol. 15, no. 4, Oct. 2013, pp. 625-634. https://doi.org/10.1016/j.jmapro.2013.05.003.

[46] M. Pantić, S. Mitrovic, M. Babic, D. Jevremović, T. Kanjevac, D. Dzunic and D. Adamovic, "AFM Surface Roughness and Topography Analysis of Lithium Disilicate Glass Ceramic," Tribol. Ind., vol. 37, no. 4, Dec. 2015, pp. 391-399. https://www.tribology.rs/journals/2015/2015-4.html.

[47] L. Henke, N. Nagy and U.J. Krull, "An AFM determination of the effects on surface roughness caused by cleaning of fused silica and glass substrates in the process of optical biosensor preparation," Biosens. Bioelectron., vol. 17, no. 6-7, Jun. 2002, pp. 547-555. https://doi.org/10.1016/S0956-5663(02)00012-X.

[48] P. Klapetek, D. Nečas and C. Anderson, "Gwyddion user guide,", vol. 2022, no. 10/5. http://gwyddion.net/documentation/user-guide-en/statistical-analysis.html.

[49] D. Fang, F. He, J. Xie and L. Xue, "Calibration of Binding Energy Positions with C1s for XPS Results," J. Wuhan Univ. Technol. Mater. Sci. Ed., vol. 35, Sept. 2020, pp. 711-718. https://doi.org/10.1007/s11595-020-2312-7.

[50] J. Zhou, Z. Liu, J. Sanderson, N. Zhou and M. Mayer, "A Method to Characterize the Quality of Interface Adhesion of Glass Substrates Using Damage Induced by Femtosecond Laser," Optical Interference Coatings Conference, Jun. 2022, pp. 1-3. https://doi.org/10.1364/OIC.2022.FA.2.

[51] Lidaris LTD, "5. Laser Peak Fluence, Intensity and Peak Power,", vol. 2023, no. 01/20, 2022. https://lidaris.com/glossary-2/fluence/.

[52] G. Thériault, "THE BEGINNER'S GUIDE ON SPOT SIZE OF LASER BEAM,", vol. 2023, no. 01/20, Aug. 2018. https://www.gentec-eo.com/blog/spot-size-of-laser-beam.

[53] M. Achintha, "5 - Sustainability of glass in construction," Sustainability of Construction Materials (Second Edition), no. 5, 2016, pp. 79-104. https://doi.org/10.1016/B978-0-08-100370-1.00005-6.

[54] K.W. Risgaard, P. Fojan, R.L. Jensen and L. Gurvich, "Surface Characterization of Coated and Uncoated Float Glass," International Summer School on Application of Scanning Probe Microscopy in Life Sciences, Soft Matter and Nanofabrication, Aug. 2013. https://same-nano.com/Abstracts2013/AFM-PhDschool_Extended%20abstract_Kasper.pdf.

[55] A.V. Naumkin, A. Kraut-Vass, S.W. Gaarenstroom and C.J. Powell, "NIST X-ray Photoelectron Spectroscopy Database," NIST Standard Reference Database 20, vol. 2023, no. 01/20, Sept. 2012. http://dx.doi.org/10.18434/T4T88K.

[56] L. Xiao, X. Zheng, T. Zhao, L. Sun, F. Liu, G. Gao and A. Dong, "Controllable immobilization of polyacrylamide onto glass slide: synthesis and characterization," Colloid Polym. Sci., vol. 291, no. 10, May 2013, pp. 2359-2364. https://doi.org/10.1007/s00396-013-2981-2.

[57] Thermo Fisher Scientific, "SEM working principle: the detection of backscattered electrons,", vol. 2023, no. 03/10, pp. 1. https://www.thermofisher.com/ca/en/home/global/forms/industrial/backscattered-electrons-sem.html.

[58] S.A. Venkatesan, "Simplifying Accelerated Electromigration Testing of Solder using Wire-based DUTs," UWspace, May 2021, pp. 1-86. http://hdl.handle.net/10012/16990.

Appendix A: Design schematics for bonding apparatus

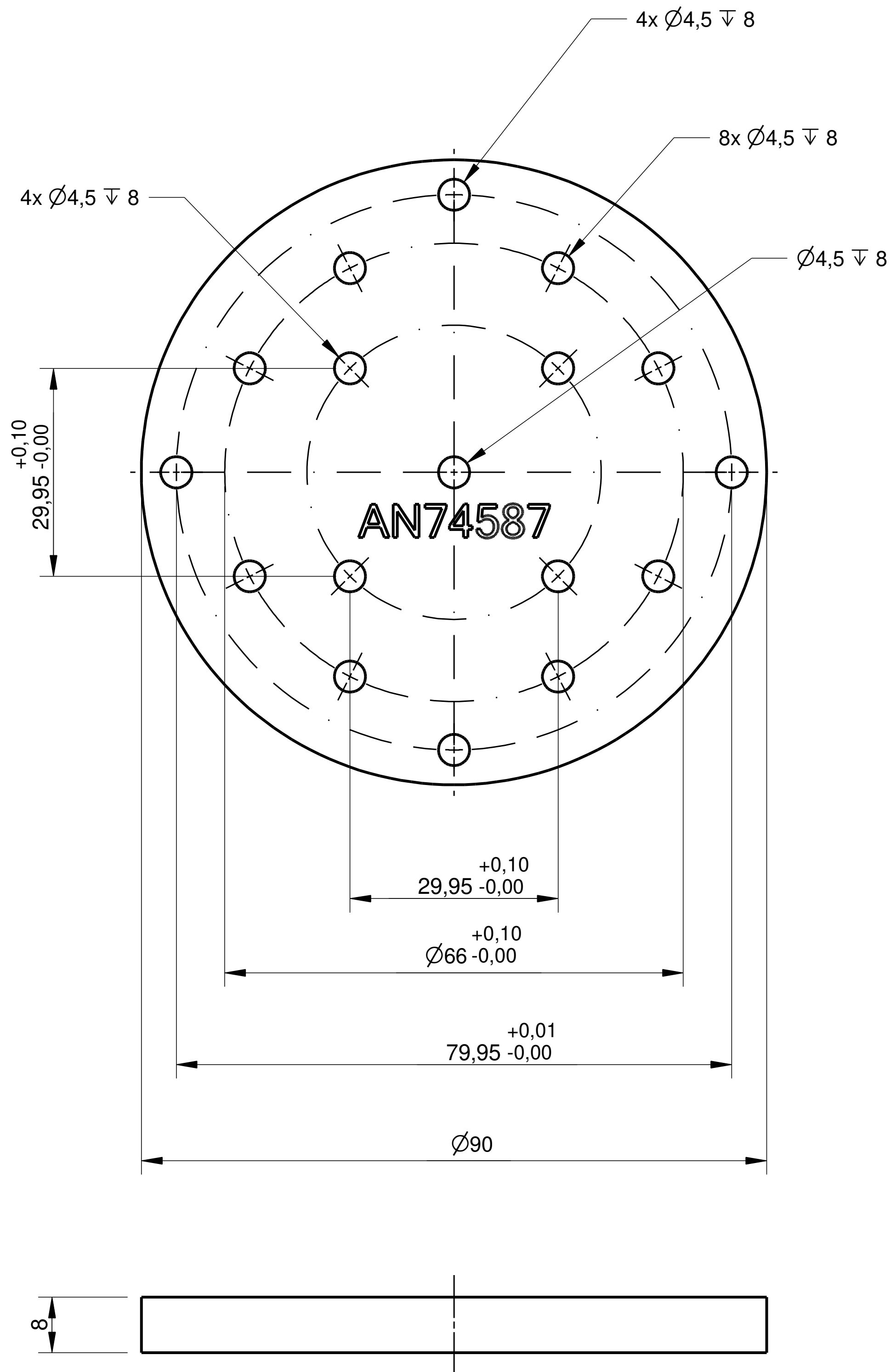


Figure A-1: CAD design for bottom piece of bonding apparatus with single plunger. Sizes are in mm. Design created by Montfort Laser and Prof. Michael Mayer.

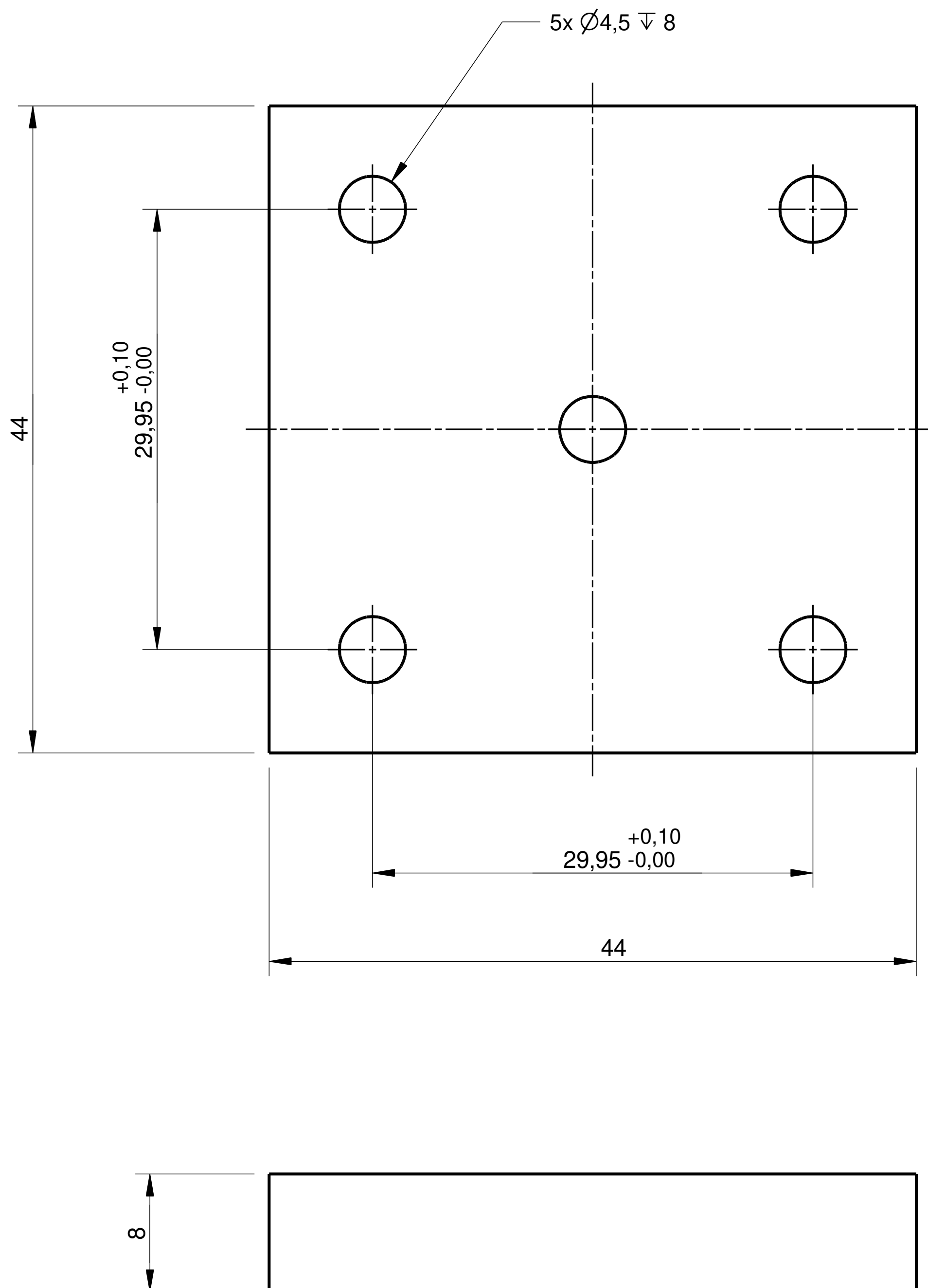


Figure A-2: CAD design for top piece of bonding apparatus with single plunger. Sizes are in mm. Design created by Montfort Laser and Prof. Michael Mayer.

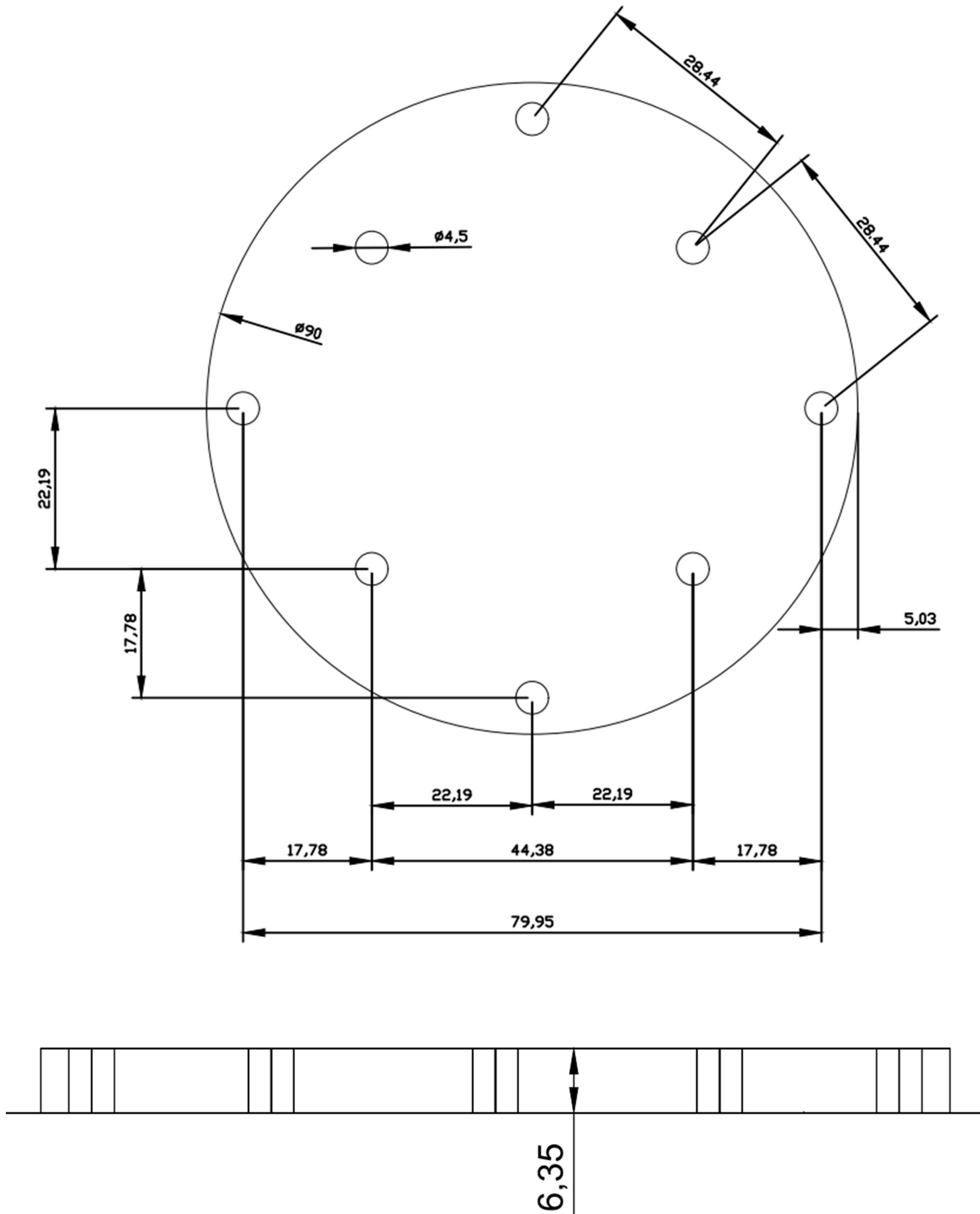


Figure A-3: Updated CAD design for bottom piece of bonding apparatus with 5 plungers. Sizes are in mm.

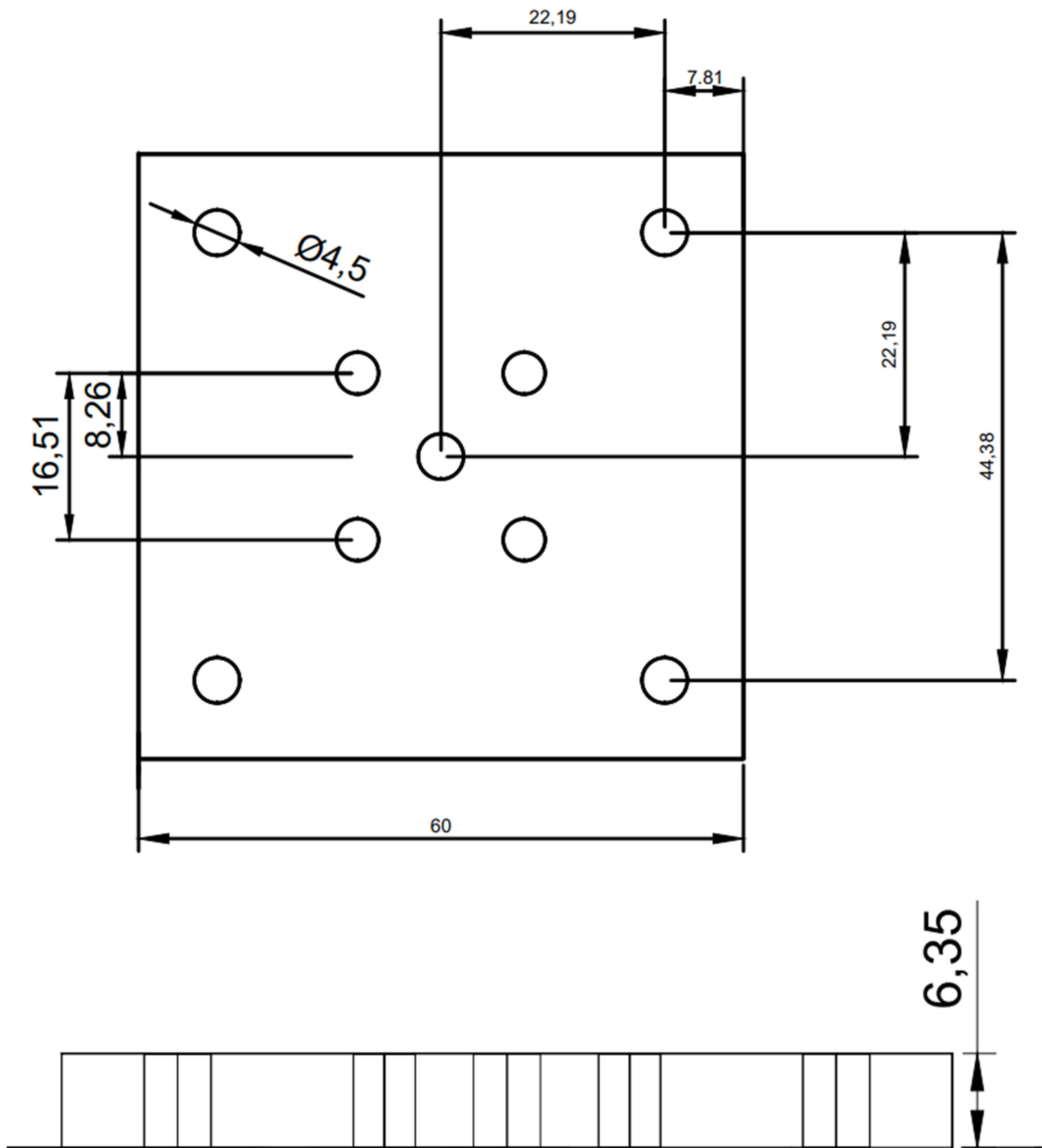


Figure A-4: Updated CAD design for top piece of bonding apparatus with 5 plungers. Sizes are in mm.

## Appendix B: Code used for data processing

```
clear all;close all
% read in the data
t=fileread('E:\OneDrive\OneDrive - University of Waterloo\School\Masters Term 2021-2023\Laser project\Trials\Surface Roughness\Surface Roughness Data for paper\Fused Si Sample 1 Flat 1\Fused Si Sample 1 Flat 1.txt');
% extract x, y, and z values
d=double(t);d13=find(d==13);sn=strfind(t,'Intensity');
if 0
  d13=d13(d13>sn); % intensity data
else
  d13=d13(d13<sn); % z-height data
end
d10=find(d(1:d13(1))==10);d13=[d10(end) d13];
tt_=t(d13(1):d13(end)+1);
tt=strrep(tt_,'Bad','NaN');
ttn=str2num(tt);
x=ttn(:,1);y=ttn(:,2);z=ttn(:,3);
% reshape z data in matrix and redefine x and y as single vectors
x=([1:736]-1)*1216/735;y=([1:480]-1)*925/479;
% setting was for field of view (FOV) 1.216 mm x 0.925 mm
zr=reshape(z,480,736);
```

Figure B-1: Code used to load surface roughness data collected using interferometry into Matlab for data processing. Code was originally written by Prof. Michael Mayer. filename: DataLoading.m

```
% visualize the data
zc=zr*80;
figure(1);contourf(x,y,zc,100,'Linestyle','none');
xlabel('X [?m]');ylabel('Y [?m]')
ax = gca;
ax.FontSize = 13;
colorbar
c=[539.341 351.461; 639.973 367.273]; % defines the line
np=10000;
xi=c(1,1)+(c(2,1)-c(1,1))/(np-1)*[0:np];
yi=c(1,2)+(c(2,2)-c(1,2))/(np-1)*[0:np];
hold on;plot(xi,yi,'r.');print -dpng fig1.png
```

```
% plot profile along the line
di=sqrt((xi-xi(1)).^2+(yi-yi(1)).^2);
zi=interp2(x,y,zc,xi,yi);
figure(2);plot(di,zi,di,zi,'.');xlabel('Distance along line [?m]')
ylabel('Z position [nm]');
ax = gca;
ax.FontSize = 13;
print -dpng fig2.png

% detrend the profile for determining the RMS roughness
zid=detrend(zi,3);figure(3);plot(di,zid,di,zid,'.');
xlabel('Distance along line [?m]')
ylabel('Z position (detrended) [nm]')
title(['RMS: ' num2str(sqrt(mean(zid.^2)),3) ' nm'])
ax = gca;
ax.FontSize = 13;
print -dpng fig3.png

% plot waviness along line
[xData, yData] = prepareCurveData( di, zi );
% Set up fittype and options.
ft = fittype( 'sin6' );
opts = fitoptions( 'Method', 'NonlinearLeastSquares' );
opts.Display = 'Off';
opts.Lower = [-Inf 0 -Inf -Inf 0 -Inf -Inf 0 -Inf -Inf 0 -Inf -Inf 0 -Inf -Inf
0 -Inf];
opts.Normalize = 'on';
opts.StartPoint = [0.021651151966128 3.62814286374389 -2.29844320018296
0.0116842369046206 30.839214341823 2.4860667149408 0.0114837865522144
36.2814286374389 -2.66825495455752 0.0112197777120702 34.4673572055669 -
1.08492776790495 0.00988961180832536 1.81407143187194 -2.7656736798373
0.00815221730247416 7.25628572748777 -2.87725752702387];
% Fit model to data.
[fitresult, gof] = fit( xData, yData, ft, opts );
% Plot fit with data.
figure(4);
h = plot(fitresult);
% Label axes
xlabel( 'Distance along line [?m]');
ylabel( 'Z position [nm]');
grid on
ax = gca;
```

```
ax.FontSize = 13;
print -dpng fig4.png

% calculate fitresult - actual data
figure(5)
zi2 = fitresult(di);
zi2 = zi2.';
plot(di,zi2-zi);xlabel('Distance along line [?m]')
ylabel('Z position [nm]');
ax = gca;
ax.FontSize = 13;
print -dpng fig5.png
```

Figure B-2: Code used to visualize surface roughness data collected using interferometry. Data is graphed initially as a contour plot of the surface of the substrate, with other graphs included such as a detrended surface profile along a specified line to determine RMS surface roughness and a graph for the determination of the waviness of the profile. Code was originally written by Prof. Michael Mayer. filename: DataVisualisation.m

```
# -*- coding: utf-8 -*-
"""
Created on Thu Sep 26 13:23:50 2019
1. This program measures the voltage using a 10A DMM
    at constant current
2. time is also recorded
Insturments:
    Circuit Specialist PS
    Hammatek PS
    KeySight NC6700
    2700 Multimeter
    10A DMM
@author: sazisurv
"""

#%% Reset All
from IPython import get_ipython
get_ipython().magic('reset -sf')


#%% Import packages required for this code
```

```
import visa
import time
import matplotlib.pyplot as plt
import subprocess
import scipy.io
from math import sqrt

#%% Close all plotting windows
plt.close('all')

#%% Saving File Name Initialization, Change before Run!
sampleName = ' Temp Trial Fused Si Coated 8,9,10,11,12'
fname=time.strftime("%y%m%d%H%M%S",time.localtime()) + sampleName

PRchange=0
#%% Define Functions
def roots(a,b,c):
    # Don't Make Changes
    """
    This function uses quadratic formula to get the real root 
(positive and less than 300)
    of an expression ax^2+bx+c=0 by entering (a,b,c).
    Note that this function will return an error if trying to 
obtain an imaginary root
    """
    disc = b**2 - 4*a*c #discriminant
    if disc >= 0:
        if ((-b + sqrt(disc))/(2*a))<300 and ((-b + sqrt(disc))/
(2*a))>00:
            return (-b + sqrt(disc))/(2*a)
       elif ((-b - sqrt(disc))/(2*a))<300 and ((-b - sqrt(disc))/
(2*a))>0:
            return (-b - sqrt(disc))/(2*a)
    else:
        return -10000000
#%% initialize variable
n = 1
#V = [[] for z in range(n)]
```

```
#V_check = [[] for z in range(n)]
#I = [[] for z in range(n)]
#I1 = []
#I2 = []
t = []
T = []
A = 3.9083E-3                #Constants for tp1000 temperature sen-
sor
B = -5.775E-7                #Constants for tp1000 temperature sen-
sor
RealTimeReadings = 100       #Real time plotting that only show a
window of this number of values

#%% List of Channel number and corresponding color while plotting
#channel=['@101']
#channel=['@101','@102','@103']
#color=['b']
#color=['b','g','r']

#%% Call PyVisa's Resource Manager
rm = visa.ResourceManager()

#%% Open GPIB Addresses, Change before Run!

#Ammeter =
rm.open_resource('USB0::0x2A8D::0x1301::MY59005695::0::INSTR')
#measure current across Circuit Specialist
#N6700C =
rm.open_resource('USB0::0x2A8D::0x0002::MY56008842::0::INSTR') #
DC Power Supply
#multiplexer = rm.open_resource('GPIB0::25::INSTR') # Multiplexer
for Voltage measurement
tempsensor =
rm.open_resource('USB0::0x2A8D::0x1301::MY59005979::0::INSTR')  #
measure voltage

#Ammeter.write("SYSTem:REMote")
#Ammeter.write("*RST")  # factory reset
```

```
#Ammeter.write("*CLS")  # clear memory
#Ammeter.write("CONFigure:CURRent:DC 10")  # sets the ammeter to
measure at the 10A range

#N6700C.write('*RST')
#N6700C.write('*CLS')
#N6700C.write('VOLT 8,(@1)')
#N6700C.write('CURR 0.1,(@1)')
#N6700C.write('OUTPUT ON,(@1)')

#multiplexer.write('*RST')
#multiplexer.write('*CLS')
#multiplexer.write('CONFigure:VOLTage')

tempsensor.write("SYSTem:REMote")
tempsensor.write("*RST")  # factory reset
tempsensor.write("*CLS")  # clear memory
tempsensor.write("CONFigure:SCALar:FRESistance")  # 4-wire con-
fig. to measure temperature

#%% Start the Timer
tic = time.perf_counter()
testDone = 0

while testDone == 0:

    #Find the temperature value from the resistance reading from
tp1000 according to the formula
    TRstr = tempsensor.query("READ?")  # The format of reading
from temp. sensor is '### OHM'
    index = TRstr.find("OHM")  # Find the index of 'OHM' to only
obtain the numbers before it
    TRvalue = float(TRstr[0:index])
    Tvalue = roots(B * 1000, A * 1000, 1000 - TRvalue)

#    Avalue1 = float(Ammeter.query("READ?"))
#    Avalue2 = float(N6700C.query('MEAS:CURR? (@1)'))
#
```

```
    for i in range(n):

        #Vvalue = -10000
#        while Vvalue == -10000:
#            try:
#                multiplexer.write(':ROUTe:OPEN (%s)' %
('@101:103')) # Open 3 channels
#                multiplexer.write(':ROUTe:CLOSe (%s)' % (chan-
nel[i])) #close channel for reading
#                rawstr = multiplexer.query('read?')
#                index = rawstr.find('VDC')
#                volstr = rawstr[0:index]
#            except:
#                    Vvalue = -10000;

        #multiplexer.write(':ROUTe:OPEN:all') # Open all channels
        #multiplexer.write(':ROUTe:CLOSe (%s)' % (channel[i]))
#close a channel for reading
        #rawstr = multiplexer.query('read?')
        #index=rawstr.find('VDC')
        #volStr = rawstr[0:index]
        #Vvalue = float(volStr)

        # Append voltage value of each channel to list
        #V[i].append(Vvalue)

        #Append current value of each channel to list
        #Avalue3 = 1.96



        #I.append(Avalue2)

    # End of For loop

    #saving found values
    #I[0].append(Avalue1)
#    I2.append(Avalue2)
```

```
#    I1.append(Avalue1)

        toc=time.perf_counter()
        T.append(Tvalue)
        t.append(toc-tic)

 #%% Plot Tvst, Rvst in real-time

#    plt.ion()
#    f = plt.figure(1)
##            plt.cla() #clear the plots for real time readings
#    #Real time plotting
#    plt.plot(t[max(0, len(t)-RealTimeReadings):],T[max(0,
len(t)-RealTimeReadings):],'b')
#    plt.xlabel('Time [s]', fontsize=30)
#    plt.ylabel('Temperature [?]', fontsize=30)
#    plt.rcParams['xtick.labelsize']=32
#    plt.rcParams['ytick.labelsize']=32
#    plt.show()
#    #Flush the data for the real time plotting window
#    f.canvas.draw()
#    f.canvas.flush_events()

    data = {}
#    data['T'] = T
    data['t'] = t
    #data['V'] = V
    data['T'] = T
#    data['V_check'] = V_check
#    data['I1'] = I1
#    data['I2'] = I2

    scipy.io.savemat('%s.mat' % fname, data)
#End of While loop

#%% close instruments
#A34411.close()
#tempsensor.close()
```

```
#N6700C.write('OUTPUT OFF,(@1)')
#N6700C.close()
```

Figure B-3: Code used to control multimeter that measures temperature of the oven during bonding thermal treatment. Temperature is measured using 4-wire resistance readings received from a temperature sensor connected to the multimeter. Code was modified, using existing code from a previous master's student who used the system [58]. filename: Laser Temp measure.py

```
clear all;close all
origImage = imread('bonded 2.png'); %cropped input image, with line for scale
greyImage = rgb2gray(origImage); %convert RGB image to greyscale
figure(1);imshow(origImage)

%calibrate pixel measurements to real dimensions
scaleline = drawline();
[cx, cy, rgbValues, xi,yi] = improfile(1000);
distanceInPixels = sqrt((xi(2)-xi(1)).^2 + (yi(2)-yi(1)).^2);
distanceInMM = 1;
MMperpixel = distanceInMM/distanceInPixels;

%create binary mask, using adaptive thresholding
BW =
imbinarize(greyImage,'adaptive','ForegroundPolarity','bright','Sensitivity',0.
50);
%overlayinitial = imoverlay(greyImage,BW);
%figure(2); imshow(overlayinitial) %view initial overlaid mask, if needed
BW2 = bwareafilt(BW, 30); %clean up mask by seleting only largest areas

%delete remaining artifacts manually
blocations = bwboundaries(BW2,'noholes');
figure(3); imshow(greyImage, []);
for ind = 1:numel(blocations)
    % Convert to x,y order.
    pos = blocations{ind};
    pos = fliplr(pos);
    % Create a freehand ROI.
    drawfreehand('Position', pos);
end

fig = uifigure('WindowButtonDownFcn',@(src,event)uiresume(src));
uiwait(fig);
```

```
% Convert edited ROI back to masks.
    hfhs = findobj(gca, 'Type', 'images.roi.Freehand');
    editedMask = false(size(greyImage));

for ind = 1:numel(hfhs)
    % Accumulate the mask from each ROI
    editedMask = editedMask | hfhs(ind).createMask();

    % Include the boundary of the ROI in the final mask.
    % Ref: https://blogs.mathworks.com/steve/2014/03/27/comparing-the-
geometries-of-bwboundaries-and-poly2mask/
    boundaryLocation = hfhs(ind).Position;
    bInds = sub2ind(size(greyImage), boundaryLocation(:,2),
boundaryLocation(:,1));
    editedMask(bInds) = true;
end

%display final mask
overlayfinal = imoverlay(greyImage,editedMask);
figure(4)
imshow(overlayfinal)

%define damage line within contour map of image
[y,x] = size(editedMask);
zr = reshape(editedMask,y,x);
xj = 1:x;
yj = 1:y;
figure(5);contourf(xj,yj,zr,100,'Linestyle','none');
xlabel('X [pixels]');ylabel('Y [pixels]')
ax = gca;
ax.FontSize = 13;

coorda1 = [7 21]; %first point of damage line a
coorda2 = [771 26]; %second point of damage line a
c1=[coorda1; coorda2]; % define damage line

coordb1 = [7 142]; %first point of damage line b
coordb2 = [771 148]; %second point of damage line b
c2=[coordb1; coordb2]; % define damage line
```

```
coordc1 = [7 273]; %first point of damage line c
coordc2 = [771 271]; %second point of damage line c
c3=[coordc1; coordc2]; % define damage line

coordd1 = [7 394]; %first point of damage line d
coordd2 = [771 393]; %second point of damage line d
c4=[coordd1; coordd2]; % define damage line

np=10000;

xi1=c1(1,1)+(c1(2,1)-c1(1,1))/(np-1)*[0:np];
yi1=c1(1,2)+(c1(2,2)-c1(1,2))/(np-1)*[0:np];

xi2=c2(1,1)+(c2(2,1)-c2(1,1))/(np-1)*[0:np];
yi2=c2(1,2)+(c2(2,2)-c2(1,2))/(np-1)*[0:np];

xi3=c3(1,1)+(c3(2,1)-c3(1,1))/(np-1)*[0:np];
yi3=c3(1,2)+(c3(2,2)-c3(1,2))/(np-1)*[0:np];

xi4=c4(1,1)+(c4(2,1)-c4(1,1))/(np-1)*[0:np];
yi4=c4(1,2)+(c4(2,2)-c4(1,2))/(np-1)*[0:np];

hold on; plot(xi1,yi1,'r.')
hold on; plot(xi2,yi2,'r.')
hold on; plot(xi3,yi3,'r.')
hold on; plot(xi4,yi4,'r.')

%rotate plot to be parallel to x-axis for evaluation of width
slope1 = (c1(2,2)-c1(1,2))/(c1(2,1)-c1(1,1));
slope2 = (c2(2,2)-c2(1,2))/(c2(2,1)-c2(1,1));
slope3 = (c3(2,2)-c3(1,2))/(c3(2,1)-c3(1,1));
slope4 = (c4(2,2)-c4(1,2))/(c4(2,1)-c4(1,1));

angle1 = atan(slope1)*(180/pi);
angle2 = atan(slope2)*(180/pi);
angle3 = atan(slope3)*(180/pi);
angle4 = atan(slope4)*(180/pi);

ha1 = imrotate(editedMask,angle1,'crop');
hb1 = imrotate(editedMask,angle2,'crop');
hc1 = imrotate(editedMask,angle3,'crop');
```

```
hd1 = imrotate(editedMask,angle4,'crop');

%figure(7); imshow(h) %rotated image
ha2 = ha1(((c1(1,2)+c1(2,2))/2-10):((c1(1,2)+c1(2,2))/2+10),c1(1,1):c1(2,1));
hb2 = hb1(((c2(1,2)+c2(2,2))/2-10):((c2(1,2)+c2(2,2))/2+10),c2(1,1):c2(2,1));
hc2 = hc1(((c3(1,2)+c3(2,2))/2-10):((c3(1,2)+c3(2,2))/2+10),c3(1,1):c3(2,1));
hd2 = hd1(((c4(1,2)+c4(2,2))/2-10):((c4(1,2)+c4(2,2))/2+10),c4(1,1):c4(2,1));
%figure(8); imshow(ha2) %cropped, rotated image

%plot graph of damage widths vs position along damage line
ha3 = sum(ha2);
hb3 = sum(hb2);
hc3 = sum(hc2);
hd3 = sum(hd2);

[xk,yk] = size(ha2);
distancelinefinal = 1:yk;

m1 = mean(ha3);
m2 = mean(hb3);
m3 = mean(hc3);
m4 = mean(hd3);

figure(9); plot(distancelinefinal*MMperpixel,hd3,'Color',[0.4940 0.1840
0.5560])
hold on; plot(distancelinefinal*MMperpixel,hc3,'Color',[0.9290 0.6940 0.1250])
hold on; plot(distancelinefinal*MMperpixel,hb3,'Color',[0.8500 0.3250 0.0980])
hold on; plot(distancelinefinal*MMperpixel,ha3,'Color',[0 0.4470 0.7410])
hold on;
plot(distancelinefinal*MMperpixel,ones(1,yk)*m4,'LineWidth',3,'Color',[0.4940
0.1840 0.5560])
hold on;
plot(distancelinefinal*MMperpixel,ones(1,yk)*m3,'LineWidth',3,'Color',[0.9290
0.6940 0.1250])
hold on;
plot(distancelinefinal*MMperpixel,ones(1,yk)*m2,'LineWidth',3,'Color',[0.8500
0.3250 0.0980])
hold on;
plot(distancelinefinal*MMperpixel,ones(1,yk)*m1,'LineWidth',3,'Color',[0
0.4470 0.7410])

xlabel('Position along damage line [mm]');ylabel('Arbitrary units')
```

```
ax = gca;
ax.FontSize = 13;
legend('1.0W', '0.8W', '0.6W', '0.4W','Location','northwest')
```

Figure B-4: Code used to process uncoated fused silica LID results. Image processing was used to generate a mask of the brightest pixels in the image, which were the damaged areas within the material. The damage width was then measured along a line to characterize damage severity. filename: laserdmgmask.m